FLORIDA STATE UNIVERSITY

FSU-FAMU COLLEGE OF ENGINEERING

HEAT AND MASS TRANSFER DURING A SUDDEN LOSS OF

VACUUM IN A LIQUID HELIUM COOLED TUBE

By

NATHANIEL GARCEAU

A Dissertation submitted to the
Department of Mechanical Engineering
in partial fulfillment of the
requirements for the degree of
Doctor of Philosophy

2022

Nathaniel Garceau defended this dissertation on April 5$^{\text{th}}$, 2022.
The members of the supervisory committee were:


Wei Guo

Professor Directing Dissertation


Sastry Pamidi

University Representative


Jingjiao Guan

Committee Member


Eric Hellstrom

Committee Member


Juan Ordonez

Committee Member


The Graduate School has verified and approved the above-named committee members, and certifies that the dissertation has been approved in accordance with university requirements.

To my family who supported and encouraged me
in adding this drop of rain to the sea of knowledge.

# ACKNOWLEDGMENTS

# TABLE OF CONTENTS

**Appendix**

# LIST OF TABLES

# LIST OF FIGURES

# LIST OF SYMBOLS

| Variable | Description | Units |
|:---:|:---|:---|
| $a$ | Decay time | s |
| $b$ | Decay length | m |
| $B_w$ | Breen-Westwater coefficient | W/(m$^2$·K$^{5/4}$) |
| $C$ | Specific heat | J/(kg·K) |
| $C_{eff}$ | Effective sticcking coefficient | |
| $d_b$ | Bath depth | m |
| $D_1$ | Inner diameter of the tube | m |
| $D_2$ | Outer diameter of the tube | m |
| $f^{-1}$ | Thermal conductivity function | W$^3$/m$^5$K |
| $g$ | Gravity | m/s$^2$ |
| $h_c$ | convection heat transfer coefficient | W/(m$^2$·K) |
| $h_{nb}$ | nucleate boiling heat transfer coefficient | W/(m$^2$·K) |
| $h_{fg}$ | latent heat | J/kg |
| $k$ | Thermal conductivity | W/(m·K) |
| $\dot{m}_c$ | Mass deposition rate | kg/(m$^2$·s) |
| $M$ | Gas molar mass | kg/mol |
| $Nu$ | Nusselt number | |
| $P$ | Pressure | Pa |
| $P_e$ | Equilibrium vapor pressure | Pa |
| $P_s$ | Saturation vapor pressure | Pa |
| $P_t$ | Tank pressure | Pa |
| $Pr$ | Prandtl number | |
| $q^*$ | Maximum nucleate boiling heat flux | W/m$^2$ |
| $q_a$ | Applied heat flux | W/m$^2$ |
| $q_{dep}$ | Deposition heat flux | W/m$^2$ |
| $q_{He}$ | Heat flux to the liquid helium bath | W/m$^2$ |
| $q_i$ | Heat flux to the inner tube surface | W/m$^2$ |
| $q_R$ | Minimum film boiling heat flux | W/m$^2$ |
| $R$ | Ideal gas constant | J/(mol·K) |
| $Re$ | Reynolds Number | |
| $\hat{s}$ | Specific entropy | |
| $t$ | Time | s |
| $\Delta t^*$ | Characteristic time to transition to film boiling | s |
| $T$ | Temperature | K |
| $v$ | Velocity | m/s |
| $V$ | Volume | m$^3$ |
| $x$ | Axial coordinate | m |

*Greeks*

| | | |
|---|---|---|
| $\alpha$ | Gas sticking probability | |
| $\delta$ | Thickness of the $SN_2$ layer | m |
| $\varepsilon$ | Specific internal energy | J/kg |
| $\rho$ | Density | $kg/m^3$ |
| $\mu$ | Viscosity | Pa·s |
| $\sigma$ | Evaporation/condensation coefficients | |
| $\gamma$ | Specific heats ratio | |
| $\psi$ | Peak heat flux tuning parameter | |
| $\omega$ | Kapitza regime empirical parameter | $kW/m^2K^n$ |

*Subscripts*

| | |
|---|---|
| $b$ | Helium bath conditions |
| $g$ | Bulk gas condition |
| $s$ | Condition at the surface of $SN_2$ layer |
| $w$ | Copper tube wall |
| $SN$ | Solid nitrogen |
| $o$ | entrance or initial conditions |

# ABSTRACT

There are many safety concerns with cryogenic systems around the world such as particle accelerators. One large concern is the sudden loss of vacuum within the particle accelerator systems. Loss of vacuum can lead to catastrophic equipment and facility damage as well as possible personnel injury. To mitigate risk and improve safety during operation of particle accelerator systems, a clear understanding of the dynamic and complex heat and mass transfer processes after a vacuum break is needed. Research in our lab focuses on the simulation of a sudden loss of vacuum in liquid helium cooled superconducting particle accelerator beam-line tubes. Loss of vacuum is simulated using an evacuated copper tube cooled in liquid helium and suddenly venting nitrogen gas from a buffer tank into the tube. Abrupt temperature rise by thermometers mounted to the tube's wall marked the location of the gas propagating front. Previous experiments and analysis in our lab using normal helium (He I) and preliminary studies in superfluid helium (He II) observed an exponential slowing of the gas propagating front (Dhuley and Vansciver, 2016). Condensation of the nitrogen gas onto the tube walls was shown to be the reason for the exponential slowing, but the underlying analysis and explanation of the gas dynamics and condensation was limited. This dissertation describes the continuation and evolution of our lab's experiments, and improvements in the quantitative analysis to better explain the underlying physical mechanisms of the slowing down process in both He I and He II. Further systematic experimental and simulation work using different mass flow rates into the evacuated tube were conducted to determine the applicability and robustness of the model in both He I and He II. The improved understanding of the physics of a vacuum break in a liquid helium cooled tube could have practical uses by improving particle accelerator safety.

# CHAPTER 1

# INTRODUCTION

This chapter provides an introduction to particle accelerators and illustrates some of the challenges they face with respect to safety for their beam tube cavities. It also discusses the scope and layout of the research conducted in this dissertations.

## 1.1  Superconducting Radio Frequency Particle Accelerators

Particle accelerators are complex machines, which affect lives all over the world. Worldwide, over 30,000 particle accelerators are in operation for a variety of applications [1]. In medical, they can be used to produce radioisotopes, which are used in diagnosis, therapy, and radiobiology [1, 2]. In national security, they have been used in cargo inspection and directed energy research [1, 3]. In high energy physics, they have been used in numerous ground breaking research studies, e.g., at CERN's Large Hadron Collider, the Higgs boson was discovered, which is informally named in the current media as the "God Particle" [4, 5].

In general, particle accelerators are sophisticated devices, which accelerate particles (i.e., protons, neutrons, or electrons) to extreme speeds to increase their kinetic energy. Lower energy accelerators, such as those in defense, medical or industrial radiography, are smaller systems, that can fit in a small room or house. These small accelerators can accelerate particles to have kinetic energy on the order of a few million electron volts [2, 3]. High energy accelerators, such as those in high energy physics, are giant system spanning many kilometers. They can accelerate charged particles close to the speed of light, so these particles have energy on order of a few giga to several tera electron volts. Examples of these large systems include: CERN's Large Hadron Collider, the linear accelerator at SLAC National Accelerator Laboratory, European Spallation Source (ESS) facility, and currently the world's most powerful neutrino beam at Fermilab's accelerator complex [6–9].

Modern particle accelerators are segmented into numerous modules, called cryomodules. These modules are linked together to create a linear or circular chain several kilometers long [10]. Figure 1.1 (a) shows an example of numerous cryomodules linked in a long tunnel to illustrate the

extreme length of these facilities. Within each cryomodule, there are a number of ultra-high-vacuum ($< 10^{-9}$ Torr) super conducting radio frequency (SRF) cavities, which create electromagnetic fields to confine and accelerate the particles into a beam [11]. These linked SRF cavities creating the beam tube path have complex shapes. One style is a series of elliptical cavities. To illustrate, which is illustrated in Figure 1.1 (b) [12, 13]. This figure shows a 3D CAD drawing illustrating the internals of an ESS cryomodule with an SRF elliptical style beam tube.
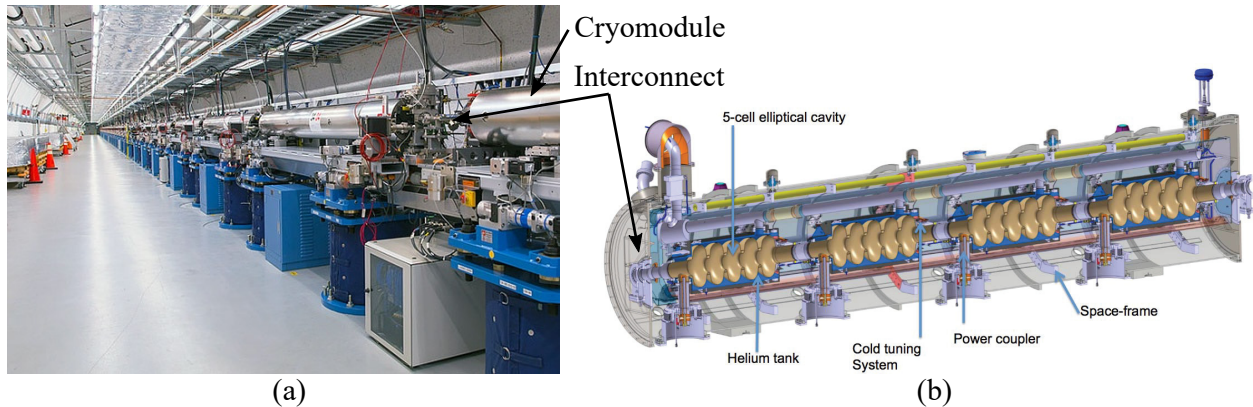


Figure 1.1: (a) Linear accelerator cryomodule chain at SLAC National Accelerator Laboratory. [Image source: https://lcls.slac.stanford.edu/overview], (b) CAD drawing of ESS's elipical type cavity cryomodule [13].

These SRF cavities are superconducting, which means they are made of a material that is characterized by no resistance to electrical flow [14, 15]. There are various superconductors some are high temperature (e.g., REBCO) and others are low temperature (e.g., niobium alloys) superconductors, which have their advantages and disadvantages [16]. Typically, the SRF cavities of particle accelerators are made of a niobium alloy, which must be maintained below 9 K to remain in its superconducting state [15]. Maintaining these cold temperatures is effectively accomplished using 2 K liquid helium (LHe) bath to immerse the cavity. Note the helium bath is also pointed out in Figure 1.1 (b).

## 1.2 Helium

Unlike all other fluids, helium does not have a triple point. The phase diagram of helium is shown in Figure 1.2 [17]. It remains as a liquid under the saturation vapor pressure even close to absolute zero, and will only solidify at high pressures. Helium does undergo a second phase transition under

2.17 K (the lambda point), where it converts from a normal fluid (He I) to a superfluid (He II). He I is composed of completely normal fluid, which is viscous and carries entropy. He II as a mixture of both a normal fluid component and a superfluid component. Superfluid component is invicid and does not carry entropy. The fraction of these two components is temperature dependent and is illustrated through the normalized densities in Figure 1.3. As seen in Figure 1.3, close to the lambda transition LHe is almost all normal fluid and close to 1 K the mix is almost completely superfluid.
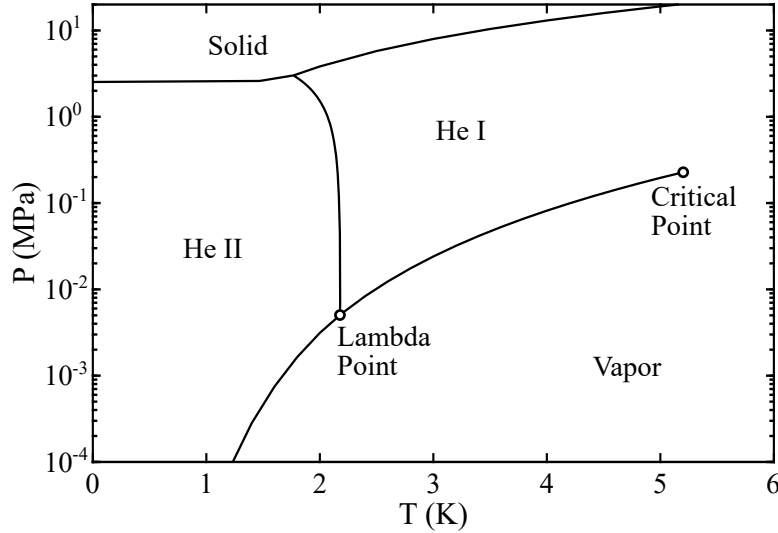


Figure 1.2: Phase diagram of helium-4 (generated from standard reference table and equation data in [17]).

He I heat transfer can be modeled similar to classical fluids with convection, nucleate boiling and film boiling. In relation to particle accelerators, He II phase is typically used because it has a more efficient heat transfer mechanism known as thermal counterflow. Thermal counterflow is a unique heat transfer mechanism in which the superfluid component moves toward a heat source at velocity $\vec{v}_s$, while the normal fluid, carrying the heat and entropy, moves away at equal and opposite speed of $\vec{v}_n$. During this process, in a static bath at temperature $T_b$, there is no bulk movement of the fluid so mass is conserved, so [18]: $\rho_s \vec{v}_s = -\rho_n \vec{v}_n$, where $\rho_n$ and $\rho_s$ are the normal and superfluid densities respectively. The magnitude of the normal component's velocity during this exchange can be calculated by $\vec{v}_n = q_a/\rho_n \hat{s} T_b$ where $q_a$ is the applied heat flux, and $\hat{s}$ is its specific entropy. As the superfluid component moves, it takes the form of a tangle of quantitized

3
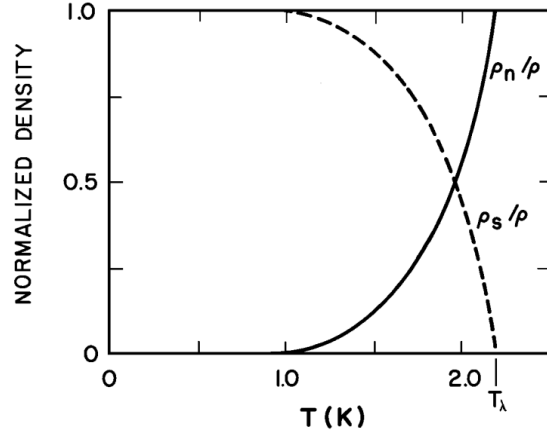
Figure 1.3: Temperature dependence of the normal fluid and superfluid densities in LHe below the lambda point. [18]

vorticies. These vorticies can break apart and reconnect as they interact and scatters the normal fluid component. This interaction of components with each other creates what is called 'mutual friction,' and limits the thermal conductivity of the bulk fluid [18].

## 1.3   Major Issue: Beam-line Vacuum Failure

A potential major safety issue in any cryogenic system is vacuum failure. When the vacuum fails, presumably air rushes into the system destroying the insulating vacuum, and it freezes or condenses on the walls. This causes a large heat load in the cryogenic fluid, which results in rapid boiling of the cryogen. Rapid boiling can result in explosive pressure buildup within the system and can result in equipment failure, facility damage, and personnel injury [19–21]. Liquid helium (LHe) based systems are especially vulnerable to pressure buildup due to its low latent heat of vaporization, which allows the LHe to boil more quickly [18, 22].

Particle accelerators have two vacuum spaces to maintain. First vacuum layer, like other cryogenic systems, is the insulating vacuum. This insulating vacuum is often, but not always, isolated per cryomodule, which can limit the scope of the damage. Second vacuum space is within the particle beam tube. This vacuum space is interconnected through all cryomodules. In many systems the interconnect between cryomodules is exposed to atmosphere, so it provides a possible leak point of air into the beam tube. This interconnect is pointed out in Figure 1.1 (a) and (b). If there is

4

a vacuum break in the beam tube, it is possible a significant portion or the whole system will be affected. Even if the cryomodules are not physically damaged, there is an extremely high cleanliness requirement within the cavity to maintain a high quality particle beam. The in-rushing gas may carry dust and particles into the cavity, which could require cleaning of all affected cavities. For example, CERN's Large Hadron Collider in 2008 had a beam tube vacuum break, and it caused damage to 53 cryomodules, 6 tons of helium to be lost, and it took many months to repair [23].

## 1.4   Past Vacuum Failure Research

Vacuum break scenario into a liquid helium cooled beam tube is a highly complex dynamic process involving many different physical and heat transfer mechanisms. An simple illustration of this process is provided in Figure 1.4. In the beginning, some event occurs which allows air to rush into the beam tube. The gas propagates within the tube, and then reaches the cold LHe cooled wall, where the gas freezes onto the surface. This is illustrated in the zoom in portion of Figure 1.4. The significant energy the gas contains is deposited into the tube walls causing the wall temperature to rise. This heat is conducted through the walls where it is taken away by the liquid helium through various physical mechanisms, i.e., natural convection, thermal counterflow and boiling. The rate of gas adsorbing on the wall depends on the wall temperature and local gas saturation conditions. A frost layer will build over time as the gas deposits on the surface, which can retard the heat flow.

### 1.4.1   Shock Tube Research

To understand this complex process a little better, one needs to understand how gas propagates within a tube at room temperature. This process is classically known as the 'shock-tube problem,'and has been studied extensively [24, 25]. Shock tubes simple devices which are composed of a long pipe broken into two sections: a higher pressure driver section and a low pressure driven section. These sections are separated by a thin membrane, such as aluminium foil, which is broken at the start of an experiment. Shock tube experiments can be used to study various phenomenon in areas such as aerodynamics, strength of materials, or chemical kinetics [26–28]. For particle accelerators, shock tubes are used to simulate the gas propagation dynamics into an evacuated beam tube to help improve system safety [25, 29, 30]. For example, one method for mitigating damage is
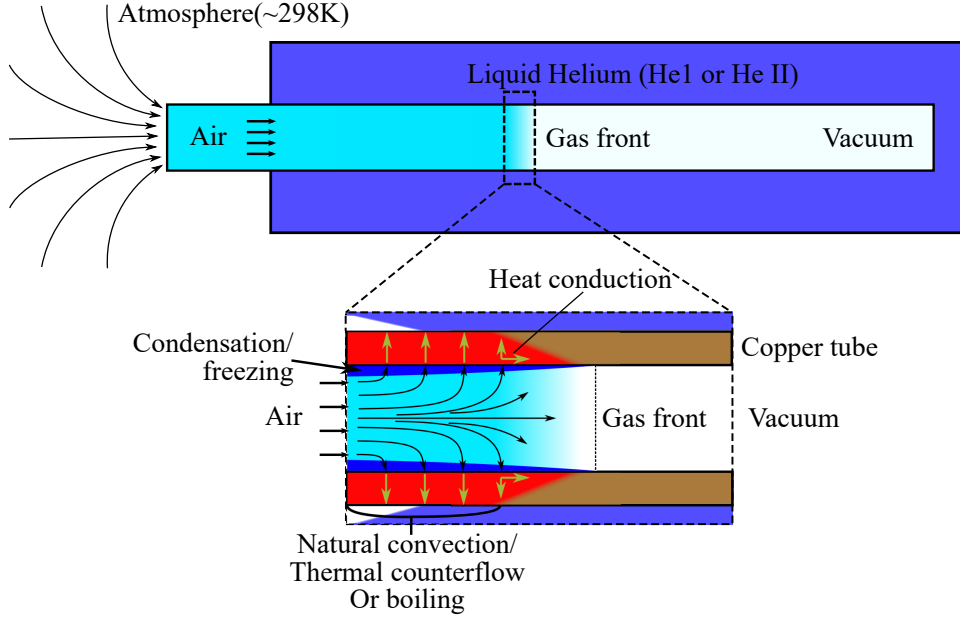
Figure 1.4: Schematic illustrating dynamic physical process which occurs after a vacuum break in a liquid helium cooled tube.

an interlock system which is used to isolate cryomodules and prevent adjacent cryomodules from being contaminated. To determine the effectiveness of such an interlock system and how fast contaminated in-rushing gas travels, Ady, et.al. at CERN conducted various room temperature shock tube experiments and simulations to evaluate leak propagation velocity [29, 30].

The exact solution to the shock tube problem is well known and can be described through the Rankine-Hugoniot relations [26, 31]. Although, when considering a low pressure and evacuated driven section, it has been shown by Takiya, et.al., smaller shocks form as the pressure drops [25]. In pure vacuum, when the diaphragm ruptures, the gas propagation is characterized by only an expansion fan. The tail tip of the fan moves at a speed, the escape speed $v_{es}$, which is calculated by $v_{es} = 2a_o/(\gamma - 1)$, where $\gamma$ is the ratio of the specific heats and $a_o$ is the speed of sound in the gas. For air, the escape speed is approximately 1700 m/s. Experimental data recorded speeds of 350-900 m/s, which is in modest agreement when considering sensor sensitivity limits and orientation [25, 29, 30].

### 1.4.2 Cryopumping Research

To understand vacuum break, one has to know how the gas is adsorbing onto the walls of the beam tube and the resulting heat transferred into the wall. This freezing or deposition phenomena, also called 'cryopumping,' has been studied by many, e.g., [32–35]. Cryopumping is commonly used in vacuum technology to generate an ultra low pressure environment by capturing the gas within the system on a cold cryogenic surface. To illustrate the cryopumping process, Figure 1.5 zooms in to the molecular scale to show gas molecules entering a volume and depositing or sticking to the inner surface when they collide. Gas condensation rate onto the freezing surface is controlled by the local pressure of the gas, the temperature of the gas, and interface temperature of the cold wall.
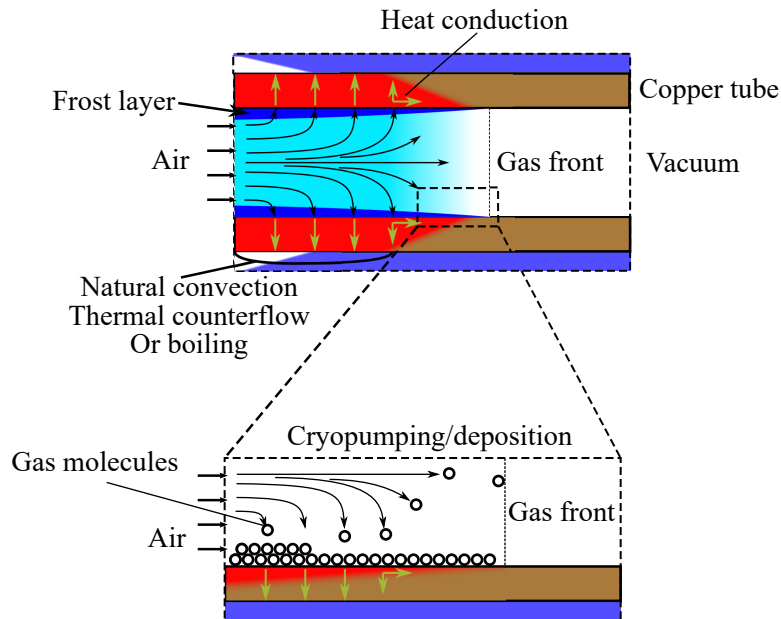


Figure 1.5: Molecular view of cryopumping on a cold surface.

During a vacuum break event, a large quantity of air rushes into the system and undergoes deposition at the cold surface. This occurs because the in-rushing bulk gas pressure is larger than the saturation vapor pressure of air at 4.2 K, which is less than $10^{-11}$ Torr [33]. In a vacuum break scenario where more than a monolayer of gas molecules can adsorb on the surface, the condensation or deposition rate will be determined by the interface temperature of the solidified gas. As more

air is adsorbed to the surface, the frost layer will retard the heat flow into the wall and cause the interface temperature to rise up eventually to the point where nitrogen will no longer condense on the surface, i.e., the local saturation point. More details on modeling how gas sticks to the surface in the free molecular region will be provided in the modeling section of Chapter 3. Additional details of gas condensation in the continuum region will be in covered in modeling section of Chapter 4.

Linked with the cryopumping is the heat load resulting from the gas molecules adsorbing to the LHe cooled surface. Ultimately the heat, which is deposited into the wall from the gas, will transfer into LHe bath. The near the surface, LHe will warm and can vaporize, perhaps explosively, if the heat absorbed is great enough. For this reason, Wiseman, et.al, at the Continuous Electron Beam Accelerator Facility (CEBAF), conducted a loss of cavity vacuum experiment using two SRF cavities immersed LHe [36]. They observed a maximum sustained heat flux of 20 kW/m$^2$ and peak heat fluxes of 35.0 Kw/m$^2$ for He II and 28.4 Kw/m$^2$ for He I. Experiments at European X-ray free-electron laser (XFEL) by Boekmann, et.al, in 2 K LHe for several different testing conditions, showed average heat transfer ranging from 3.3 to 23 kW/m$^2$ [37]. These obtained values are good to know for reference, but do not allow one to see the full picture of a vacuum break scenario. Further details of heat transfer mechanisms and heat load modeling into a He I bath will also be covered in depth in Chapter 3 and into a He II bath will be covered in Chapter 4.

### 1.4.3   Vacuum Break Into Liquid Helium Cooled Tube Research

To get the whole picture of a vacuum failure event within particle accelerator, both the gas propagation, heat transfer, and condensation or freezing effects need to be coupled together. Experimental observations in past vacuum break failure research showed that the supersonic gas rushing into a cold evacuated tube, like a particle accelerator's beam tube, will radically slow. Experiments at XFEL and Fermi National Accelerator Laboratory observed propagation speeds on the order of 10 m/s, which are much slower than speeds of a room temperature shock tube [37, 38].

Foundational work conducted at the National High Magnetics Field Laboratory (NHMFL) by Dhuley and Van Sciver set out to better explain the interlinked heat and mass transfer processes occurring during a beam line vacuum break [39–41]. Their experiments used a straight evacuated copper tube cooled by He I to create a simplified setup mimicking a particle accelerator's beam tube. Vacuum break was simulated by venting nitrogen ($N_2$) from a reservoir tank into the evacuated tube. To observe the propagating gas front, copper tube's surface temperature and internal pressure

were measured. From these experiments, they observed an exponential slowing of the propagating gas front. Additional preliminary experiments conducted in superfluid helium (He II) showed that He II showed a stronger slowing effect. Through further analysis, they were able to qualitatively attribute the gas deceleration to the gas condensation and freezing to tube's inner walls using a conservation of mass analysis. Although, there were some issues with their experimental setup and weaknesses in their analysis, which needed to be addressed. Experimental system problems and upgrades are discussed in Chapter 2. Weaknesses of Dhyley's conservation of mass analysis model and its missing physical links are discussed further in Chapter 3.

## 1.5   Scope of Research and Organization of this Dissertation

This dissertation describes next stage research conducted at NHMFL to significantly advance the experiments and analysis conducted by Dhuley and Van Sciver. Objective of this work was to expand the understanding and quantitatively explain a vacuum break event in a LHe cooled beam tube. Experiments conducted in this dissertation follow Dhuley and Van Sciver's procedures, but fabricate a new experimental setup based on a helical copper tube design. This allowed systematic experiments in both He I and He II to be conducted. Additionally, this dissertation covers the development of a new vacuum break model and simulation, which quantitatively describes the physical processes occurring during a vacuum break.

Chapter 2 begins by describing issues with Dhuley's experimental setup and discusses issues with its continued use. This chapter discusses design choices for a simplified setup as well as the initial system upgrades needed for systematic study. It also covers other details of the procedure, instrumentation, and data processing. Additionally, this chapter covers some preliminary results illustrating how condensation point effects results. Finally, this chapter shows the final setup which was used for systematic studies in both He I and He II. Contents in this chapter have been peer reviewed and published in [42–44].

Chapter 3 begins by discussing Dhuley's conservation of mass model and its weaknesses. The chapter then discusses a new systematic model which quantitatively links experimental observations to physics of what is occurring during a sudden loss of vacuum in a liquid helium cooled tube. Within this modeling section a more detailed discussion He I heat transfer, mass deposition and gas dynamics is covered. Next part of the chapter discusses the systematic results of the He I

experiments and shows comparisons to the He I theoretical model. Additional discussion on extracted information about propagation dynamics and nitrogen frost layer growth is also reported. Contents in this chapter have been peer reviewed and published in [42, 44, 45].

Chapter 4 covers a more detailed description of He II heat transfer and how it differs from He I. This section covers how the model was updated to account for the different heat transfer mechanisms of He II. It also describes an update to the mass deposition model, which better describes condensation in the continuum region. A comparison of the numerical model with the systematic experimental studies was conducted for model verification and is reported within the chapter. Additional information on different aspects of heat flux through the tubular system was also extracted from the model. Results within this chapter were peer-reviewed and have been published in [46].

Chapter 5 discusses design of a new experimental system which will better simulate an elliptical style SRF cavity. For this new facility, the helical tube is replaced with a short tube with a single voluminous cylindrical cavity. This cavity has the same aspect ratio as a single elliptical style SRF cavity cell. This chapter reports preliminary experimental observations from the vacuum break experiment in He I.

Final chapter, Chapter 6, summarizes the body of this work. It also illustrates and suggests areas for future research and experimental development.

# CHAPTER 2

# EXPERIMENTAL SETUP

This chapter covers the upgrades and development of a new experimental test facility to systematically measure gas propagation within a LHe cooled tube. It also covers a discussion of condensation point and the effect on the measured gas propagation. Finally, it shows the end experimental system developed to systematically study the exponential slowing of the gas within the tube. Contents of this chapter are also peer reviewed and published in [42–44].

## 2.1   Design Simplifications

Ideally this research would be conducted in an actual SRF beam tube but, due to various challenges associated with procurement, fabrication and modeling, this research continues using Dhuley's design simplifications [41]:

1. Typical particle accelerators beam tubes are designed as series of interconnected complex shaped cavities made of niobium alloys as illustrated in Chapter 1. Modeling the highly dynamic gas slowing process in the complicated geometry would be immensely challenging. Like Dhuley, this study uses a simple tube immersed in LHe instead of an actual SRF niobium cavity.

2. Niobium is a challenging and expensive metal to procure and it is difficult to work with. For example, welding a niobium channel to a standard stainless tube is a complex process involving nickle plating, which is not practical for these experiments at this time. Instead, this study continues using copper as a substitute. Unlike niobium, copper is readily available in many standard tube and pipe sizes. Copper plumbing can be easily attached to stainless steel through silver brazing or use of standardized fittings.

3. SRF beam tubes are positioned horizontal within a liquid bath of the particle accelerators. Dhuley used a straight vertical tube immersed in LHe to conserve laboratory space and for use in existing cryostats. Experiments in this study are conducted in a helical coil where the central axis to the coil is vertical making the coiled tube is almost horizontal. This new design allows for a longer tube to be tested within a more compact space, which allowed for characterization of the slowing effect in both He I and He II.

4. In a typical vacuum failure air will rush into the vacuum space and propagate within the tube. Air is a complex mixture of gases with a possibly daily varying humidity level, all of which can make analysis challenging. Dry air is a mixture of two major components: 21% oxygen and 79% nitrogen. To simplify this process and control the mass flow rate into the evacuated beam tube, an reservoir tank filled with 99.999% pure nitrogen was again used in these studies.

5. Dhuley showed temperature sensors were more sensitive to gas front arrival compared to pressure sensors. Experiments conducted in this paper will continue using temperature sensors to measure gas front propagation. Numerical modeling in the next chapter will illustrate the interlinked physics of why this method can be used.

## 2.2   Preliminary Experimental Setup

Some of the first experiments in vacuum break were conducted in a copper straight tube by Dhuley. These experiments used both pressure and temperature sensors monitor a spike in their measured values [39, 47]. This spike was attributed to the location of the propagating gas front within the tube. Though these experiments, several key observations were made. First, the gas propagating within the beam tube does indeed slow. Second, the experiments showed that temperature sensors were much more sensitive to the gas front arrival than pressure sensors. Finally, He II, most commonly used in superconducting particle accelerators, might have a stronger slowing effect than He I due to the different heat transfer mechanism, i.e., thermal counterflow [41].

Valuable insight was gained from Dhuley's vacuum break experiments, but there were issues with the setup. To better characterize the slowing effect within the simplified beam tube, the tube needed to be significantly longer, specifically for the He II experiments. Reaching the He II phase within the cryostat requires evaporation cooling using a vacuum pump. This cooling causes the liquid level to drop to about half of the original height, which causes many of the sensors on the straight copper tube to be above the liquid level. To solve this, Dhuley and Van Sciver proposed a helical tube based system for future work. Work conducted in this dissertation picks up from that initial suggestion, builds a new the system, tests it, and helps improve the understanding of a vacuum break scenario.

### 2.2.1 New Helical System

The new vacuum break experimental system was designed with a 25.4 mm inner diameter, 1.25 mm thick, 5.75 m long helical copper tube. Additionally, to allow the longer test time, the buffer reservoir size was increased from 86 L to 230 L. This size increase allowed for pressure drop within the reservoir for the duration of the experiment to be minimized, thereby reducing the change in mass flow rate over time. Summery of the geometries changes from the straight tube system to the new helical tube system are shown in Table 2.1.

Table 2.1: Summery of changes between Dhuley's original straight tube system and the new helical tube system.

|                           | Straight tube system | Helical tube system |
| ------------------------- | -------------------- | ------------------- |
| Pipe length (m)           | 1.5                  | 5.75                |
| Inner pipe diameter (mm)  | 32.1                 | 25.4                |
| Wall thickness (mm)       | 3                    | 1.25                |
| Coil diameter (mm)        | -                    | 229                 |
| $N_2$ tank (L)            | 86                   | 230                 |

The system's larger nitrogen tank was connected to the tube system uses the same fast acting solenoid valve (opening time less than 25 ms), which was the method also used in the straight tube system. After the solenoid valve a miniature venturi tube for flow regulation was also reused. The venturi chokes the flow at the throat at the local speed sound thereby allowing mass flow regulation as a function of the backing tank pressure. The exit of the venturi is attached to a 32 mm 304 stainless steel extension tube. This extension is silver brazed to a copper elbow, which was then soldered to the helical coil. The extension supports the helical coil such that the coil is suspended in the center of the cryostat not touching the walls. Figure 2.1 (a) shows a schematic of Dhuley's and Van Sciver's setup, and Figure 2.1 (b), shows a schematic of the new experimental setup. Figure 2.2, shows a picture of the helical pipe assembly after fabrication.
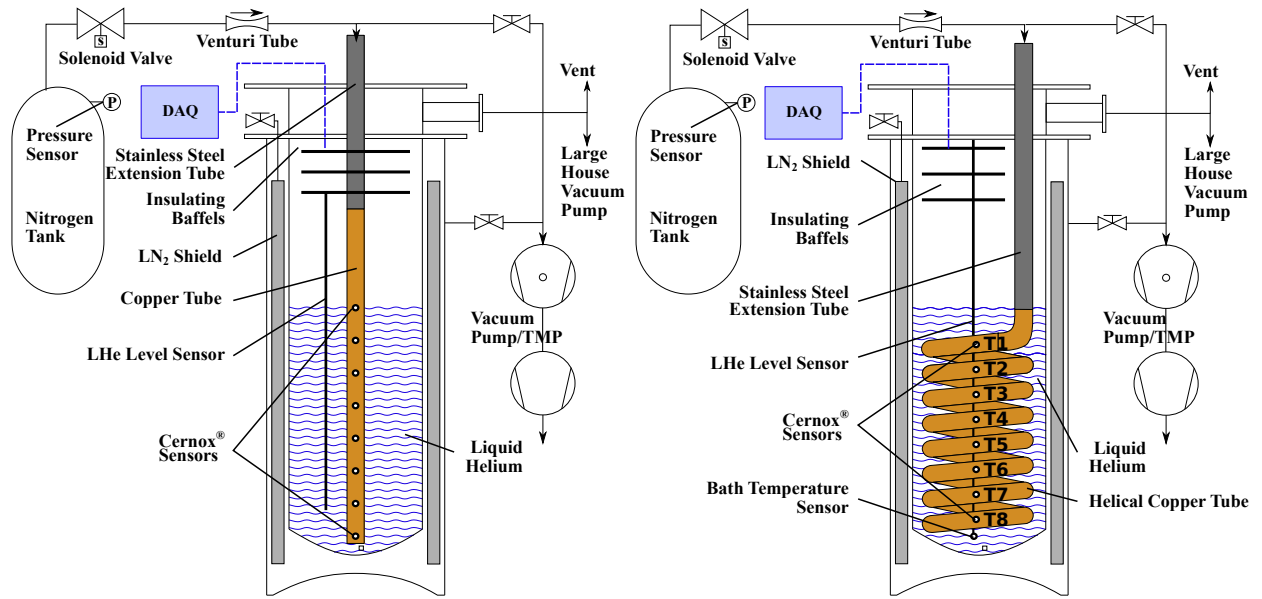
Figure 2.1: Schematic diagram of Dhuley's straight tube system (a) and schematic of the initial helical tube setup (b).



Figure 2.2: Initial helical tube setup after fabrication.

### 2.2.2 Instrumentation & Safety

Many of the instrumentation, sensors and data acquisition methods in currently presented research were also reused or adapted from Dhuley and Van Sciver's straight tube system. Like the straight tube system, to measure gas front propagation, the surface temperature of the helical beam tube was measured using seven Lake Shore Cernox™ SD-package thermometers, which have a thermal response of 15 ms at 4.2 K. These sensors were encapsulated in 2850 FT Stycast™ epoxy to insulate them from the bulk LHe as detailed by Dhuley [47]. To mount the sensors on the new helical system, the thin walled soft copper tube was deformed slightly and then polished to create a smooth flat surface. To ensure good thermal contact, a thin piece of indium foil (less than 0.3 mm thickness) and Apiezon™ thermal grease was sandwiched between the sensor and the copper tube wall. Sensors were secured to the wall using stainless steel wire or a stainless hose clamp. Each sensor was mounted at regular 72 cm intervals along the tube. Figure 2.3 shows an example of the sensors (a), their casting (b), and their mounting on the surface of the copper tube (c).
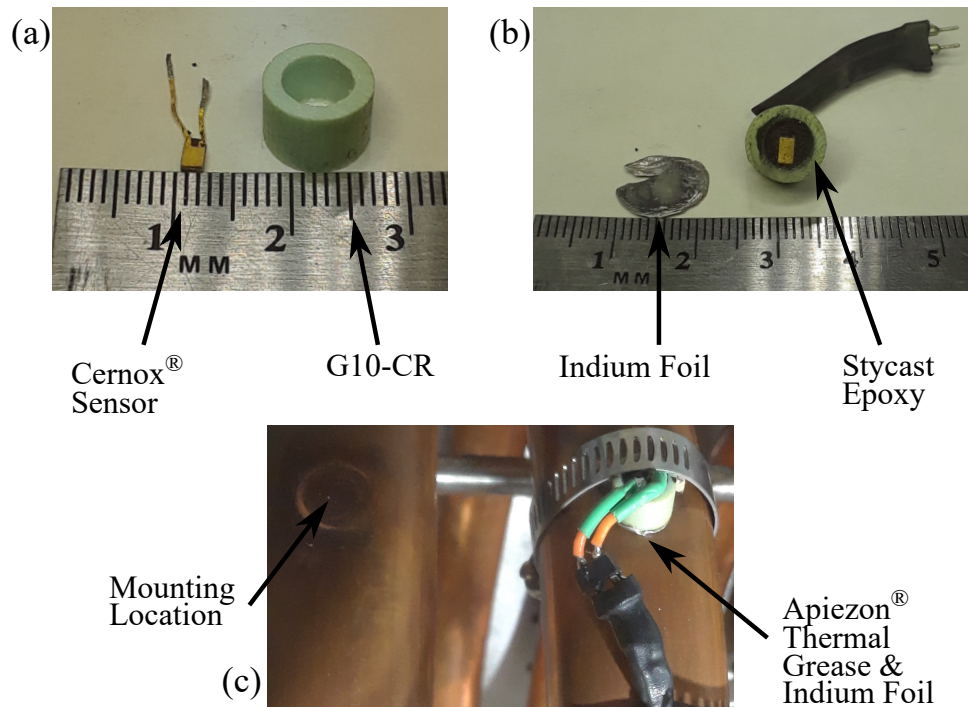


Figure 2.3: Cernox™ sensor and support G10-CR sheath (a). Thin indium foil and sensor after casting in Stycast™ epoxy (b). Typical sensor mounting on the surface of the copper tube (c).

Cernox™ sensors are a resistance temperature detector, which means their electrical resistance depends on the temperature. These sensors were powered by reusing Dhuley's in-house designed 3 μA constant current supply. It consists of a 2 MΩ in series with a 6 VDC battery and has a 4.09 kΩ reference resistor for validating the current. Temperature sensors and the reference resister were chained in series and used a DC four-wire method to determine the resistance on each sensor.

To measure the vacuum pressure within the tube a cold cathode guage ($10^{-3}$ to $10^{-7}$ range) was mounted just after the venturi. Pressure within the nitrogen buffer tank was measured with a factory calibrated TD1000 pressure transducer from Transducers Direct, which was powered at the recommended 24 V using a TENMA 72-7245. This sensor allowed the pressure drop within the buffer tank to be recorded so mass flow could be calculated. Details of mass flow calculation are presented in Section 2.3.1.

Data from the temperature sensors, the tank pressure sensor, and the solenoid valve triggering signal were routed into four Data Translation, Inc. DT9824 USB data acquisition modules, and the data was recorded with National Instruments LabView™ at a frequency of 4800 Hz.

To monitor the LHe level within the bath, an American Magnetics Inc. superconducting LHe level sensor was suspended from the baffles in the center of the helical coil. Calibration holes on the sensor itself were used to accurately determine where the liquid level was in relation to the internal structure. The 46 cm calibration hole was positioned such that it aligned with the top of the helical coil at the elbow joint.

Heavy rapid boil off results from the large heat load introduced into the system after breaking the vacuum in the beam tube. During the experiment boil off was vented into a helium recovery line when possible. To prevent pressure buildup within the system, two large diameter 1/3 psi (2.3 kPa) relief valves were also placed on the system. A third 1 psi (6.9 kPa) safety valve was mounted in the top flange of the cryostat should one of the relief valves fail to open. To remove the frozen gases within the tube before subsequent tests, the system must be brought to room temperature. During warmup, tube is vacuum pumped, but should power fail, a fourth 1 psi (6.9 kPa) safety valve is mounted to the evacuated beam tube to relieve pressure from the melting and evaporating gas.

Standard safety precautions were taken for dealing with and transferring cryogenic liquids: long clothing, safety goggles, and insulated gloves.

### 2.2.3   Experimental Procedure

Experimental procedure was based on Dhuley and Van Sciver's method. First, the system, including both the beam tube and the vacuum shields, was fully evacuated below $10^{-5}$ Torr. Next, liquid nitrogen ($LN_2$) was filled into the $LN_2$ shield in the cryostat and the inner LHe bath for precooling. System was allowed to precool for at least ten hours overnight to ensure it was cold and to minimize LHe loss during cooldown. After precooling, the $LN_2$ was removed from the bath, and the system was allowed to warm to at least 90 K ensuring there was no liquid left in the bath. While the system was warming, the pressurized gas lines before the solenoid valve tank and the tank itself were evacuated and purged three times with ultra high purity nitrogen gas. After, they were pressurized to the desired run pressure, i.e, 50 kPa, 100 kPa, 150 kPa or 200 kpa. Following the slight warm-up, LHe was slowly transferred into the LHe bath over several hours at a temperature drop rate of about 1 K/min to maximize cooling potential of the LHe and minimize LHe loss. For the He I runs, the liquid was filled up to the top of the copper elbow connected to the stainless steel extension tube or a reading of 46 cm on the liquid level sensor. For a He II run, the bath was filled to a maximum point corresponding to roughly the 84 cm reading on the liquid level sensor. After, the helium recovery line was closed and the bath was evaporatively cooled using a large house vacuum pump. The bath was cooled down to around 1.95 K, which is well below the lambda transition point of 2.17 K. Once the temperature was reached, the liquid level was noted. Final bath level varied slightly, but was always around 46 cm, which allows full immersion of the tube coil, but below the exit of the vacuum jacket. Gas pressure in the buffer tank was verified and data acquisition began. After data recording was running for at least one second, a opening signal current was supplied to the solenoid valve between the evacuated beam tube and the nitrogen buffer tank allowing the nitrogen gas to rapidly flow into the tube. Valve was left opened for at least eight seconds. From this point, valve was closed and system was allowed to warm to room temperature. Data acquired was then processed in Matlab.

## 2.3   Preliminary Results

### 2.3.1   Mass Flow Measurement

Important parameter in determining the severity of a vacuum break in a particle accelerator is the mass flow rushing into the system. The mass flow was choked at the speed of sound at the

venturi's throat, which allowed regulation of the mass flow by changing the initial starting pressure of the nitrogen buffer tank. This method follows Dhuley and Van Sciver's technique for simulating different rupture sizes into a beam tube without having to change the size of the venturi throat. The mass flow rate into the tube can be calculated using the well known formula for the isentropic discharge of a pressurized tank under choked flow conditions [26]:

$$\dot{m} = -\left(\frac{P_{to}^{(\gamma-1)/\gamma}V_t}{\gamma R_{N_2}T_o}\right)\left(P_t^{(1-\gamma)/\gamma}\frac{dP_t}{dt}\right) \tag{2.1}$$

where $V_t$ is the volume of the nitrogen buffer tank and the attached lines (approximately 230 L), $T_o$ is the starting temperature (room temperature or around 298 K), $\gamma$ is the ratio of the specific heats (1.4 for nitrogen), $P_{to}$ is the starting pressure (50, 100, 150 or 200 kPa), $P_t$ is the instantaneous pressure in the tank at time $t$, and $R_{N_2}$ is the nitrogen gas constant. Pressure drop in a tank under isentropic discharge choked conditions can be modeled in the form [26]:

$$P_t = (P_o^B + A*t)^{1/B} \tag{2.2}$$

where $B = (1-\gamma)/2\gamma$, and $A$ is a fit coefficient, which can be obtained by least squares regression. After knowing $A$, the $dP_t/dt_t$ term of can be evaluated, and then the mass flow can be calculated. Figure 2.4 (a) upper graph contains the experimental buffer tank drop and the fit $P_t$ curve. The lower graph is the conversion of that data to mass flow. Figure 2.4 (b) shows the time dependent mass flow rates for the various backing tank pressures used in the experiments. The lines cut off a little after at the rise time of the last sensor. Note, this last sensors rise time will differ depending on if experiment is conducted in He I or He II. It should also be noted that the regression fit for the mass flow is also used in the modeling of the subsequent chapters to account for the drop in mass flow over the course of an experiment.
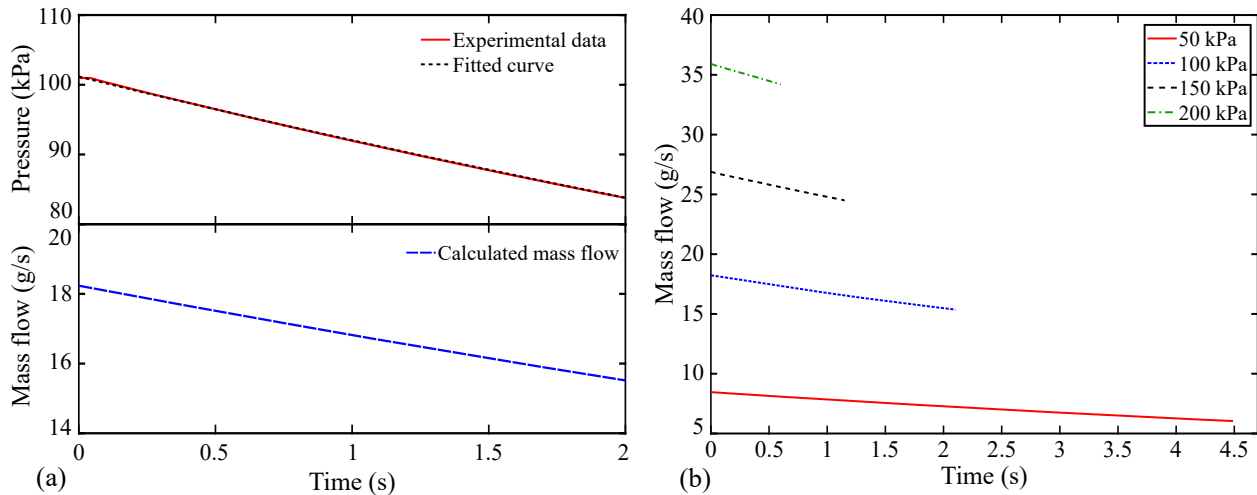
Figure 2.4: (a) Calculated mass flow based off of tank pressure drop over the course of an experiment with 100 kPa backing pressure. (b) Comparison of the different mass flow rates for 50-200 kPa runs.

### 2.3.2 Initial Processing

There was some data processing needed to acquire useful data from the experiment. Using four data acquisition boxes causes a slight deviation in the recording time from box to box. The data was able to be synchronized in post processing using the voltage reference signal from the solenoid valve switch which was routed to each box.

After synchronization, resistance of each sensor was calculated, and then converted to temperature. This temperature data had significant and varying harmonic noise in addition to random noise. This noise causes up to a $\pm$ 0.2 K temperature swing in some temperature readings for both He I and He II experiments. To researcher's best efforts at the time of these experiments were conducted, this noise was unable to be eliminated with physical modification such as grounding or shielding. To remove the harmonic and random noise, the data was smoothed with an 80-point moving average. Figure 2.5 shows an example of the effect of smoothing the data for one sensor in a He I run. Same smoothing method was conducted on all sensor data for both He I and He II. It should be noted that smoothing the data can decrease the accuracy of the temperature readings, but it was necessary.
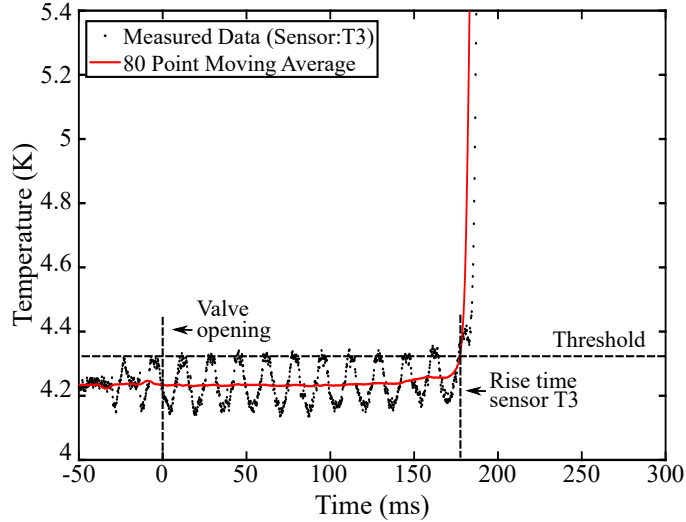
Figure 2.5: Effect of an 80-point moving average on the harmonic and random noise seen in the data.

Next step in data processing was to determine when the gas front arrived at the sensor location. The time when a near vertical rise in the temperature marks the gas front arrival, and is termed the 'rise time.' To determine this rise time an arbitrary threshold level was set for the data, and when the smoothed temperature profile exceeded this value, that time is recorded as the rise time. Dhuley and Van Sciver set a threshold of three standard deviations above the average bath temperature before the start of the experiment. This method was not appropriate for He II case which a bath temperature rise was recorded over the course of the experiment. For He I an arbitrary threshold level of 0.1 K above the bath temperature was set for these experiments. This temperature is above the 1 atm saturation temperature of 4.23 K, and it is in the near vertical region of the temperature data. For He II, the arbitrary threshold level was set at 2.17, the lambda transition point. Threshold was set higher because the bath temperature starts rising immediately when a heat load is induced. The temperature profile is again nearly vertical in this region so it will not effect results significantly. Figure 2.6 shows experimental temperature data after smoothing for both He I (a) and He II (b). Threshold level in Figure 2.6 (a) and (b) are marked with a horizontal black line, and the rise times are marked with vertical dashed lines.

20
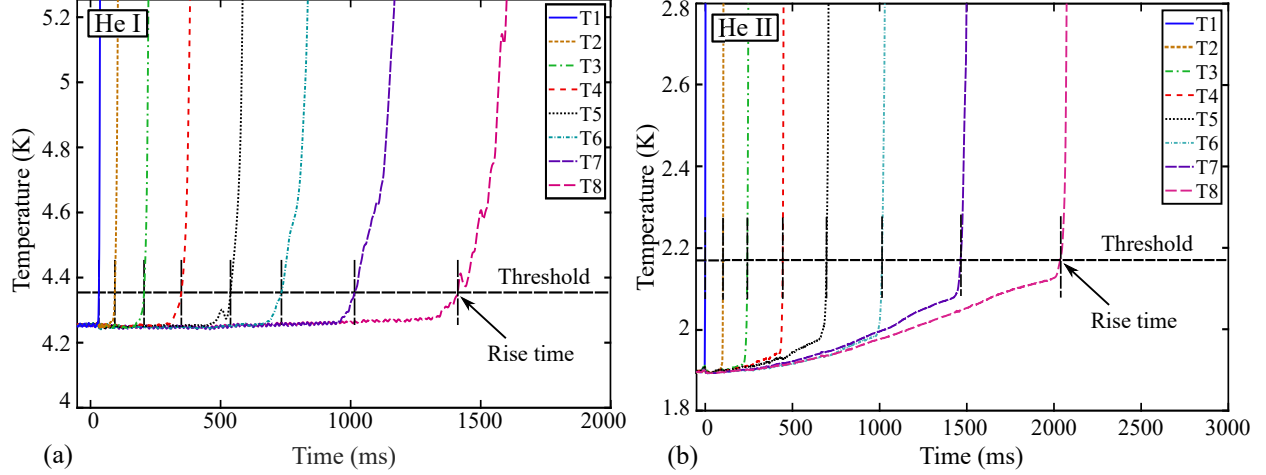
Figure 2.6: Illustration of the threshold level and corresponding rise times in the helical system after smoothing for He I(a) and He II(b) [44].

### 2.3.3 Gas Front Propagation Modeling

At a quick glance of figure 2.6, one can easily observe there is a difference in rise times with He I T8 sensor rising at 1400 ms while He II rising slower at 2000 ms. It can also be observed that the equally spaced sensors rise closer together in the beginning and spread out later in both experiments, which indicates a deceleration. To characterize this exponential slowing, Dhuley and Van Sciver developed an empirical model where an exponential curve was fit to the experimental rise time data in the form $t(x) = a(e^{x/b} - 1)$ where $t(x)$ is the arrival time at location $x$. $x = 0$ is at the first sensor and is also at the liquid level. The $a$ coefficient represents the decay time and the $b$ coefficient represents the decay length. The $a$ and $b$ coefficients were obtained by non-linear least squares regression [39, 41]. Arrival time equation can be converted to a velocity deceleration curve in the form $v = v_o e^{-x/b}$ where $v_o$ is the tube entrance velocity or the velocity at the first sensor. Entrance velocity can be calculated by $v_o = b/a$. Figure 2.7 shows the tube position, $x$, and the corresponding rise time at that location, $t(x)$. Exponential fit of the data is also illustrated in the figure. Coefficients from the regression fit, $a$, $b$, and the calculated inlet velocity, $v_o$, are presented in Table 2.2.
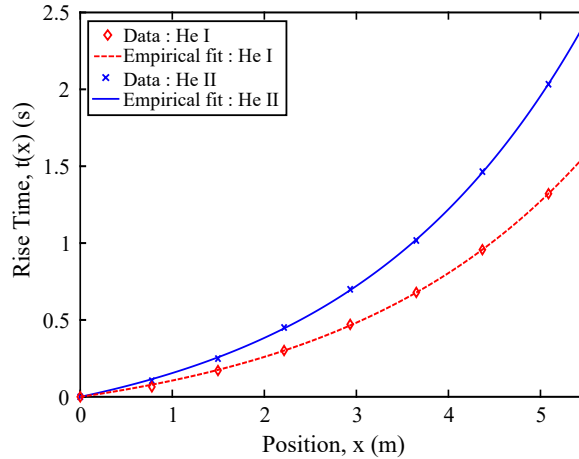
Figure 2.7: Rise time versus position with exponential fitted curves for He I and He II [44].

Table 2.2: Regression fit and inlet velocities based on actual liquid level at 100 kPa [44].

|  | a (s) | b (m) | $v_o = b/a$ (m/s) |
| --- | --- | --- | --- |
| Helical tube He I | 0.236 | 2.70 | 11.42 |
| Helical tube He II | 0.323 | 2.56 | 7.91 |
| Straight tube He I [39] | 0.031 | 0.63 | 20.32 |

These observations confirm Dhuley and Van Sciver's preliminary observations and indicate that He II does seem to have a stronger slowing effect than He I. Although, it should be noted that the values calculated from the fitting are considerably different Dhuley's published values. This difference could be due to couple reasons such as different geometry between the two systems, or a different mass flow rate change rate due to a bigger nitrogen reservoir. A larger reservoir in the helical tube case means there was less pressure drop thereby less mass flow change over the same time interval.

### 2.3.4 Effect of Condensation Point

The possible explanation for the observed differences in the He I and He II experiments can be assumed to be from the differences in heat transfer in He II. Although, there is a slight issue with this assumption. Looking at the calculated entrance velocities for both He I and He II, one can note that they are different: 11.42 m/s for He I and 7.91 m/s for He II. Both these experiments

were conducted under almost the same conditions. Therefore, the entrance velocities should be approximately the same, but they differ.

It can be surmised that this was an effect of the cold tube above the liquid surface. It is possible that the wall was cold enough to condense the nitrogen so the properties of the gas (density, pressure, mass flow, etc.) would be different at the start of the liquid level. Temperature above the liquid level was not monitored so it was plausible that the nitrogen started condensing above the liquid level, which is the assumed condensation point. For example, to reach the He II phase, the LHe bath was filled to the highest possible level making the a good portion of the tube above the liquid level cold. Also during the evaporative cooling phase, there was additional convective cooling from the outgoing gas, which could cool the upper parts of the tube above the fill point further. This could cause considerable temperature variation between runs.

The above data for He II can be shifted such that the assumed condensation point is no longer at the liquid level but higher in the tube. If the condensation point in He II is shifted to 38 cm above the liquid level, then the entrance velocities will approximately match, as shown in table 2.3. Looking at figure 2.8 it can be seen that He II still shows a slightly stronger slowing which is likely due to the higher apparent thermal conductivity, but it is no where near as strong as what was seen previously in figure 2.7.
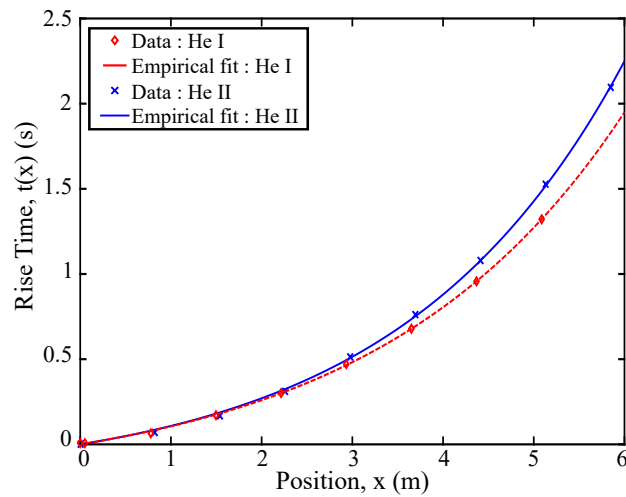


Figure 2.8: Graph showing the rise time versus position after shifting the condensation point of He II by 38 cm [44].

Table 2.3: Regression fit coefficients and inlet velocities based on a 38 cm shift in the assumed condensation point for He II at 100 kPa [44].

|  | a (s) | b (m) | $v_o = b/a$ (m/s) |
|---|---|---|---|
| Helical tube He I | 0.236 | 2.70 | 11.42 |
| Helical tube He II | 0.216 | 2.47 | 11.4 |

This uncertainty of temperature profile above the liquid level needed to be addressed before further steps were taken. To determine the temperature profile three sensors were moved to the upper portion of the tube. The top sensor (T1) was placed 12 cm from the top flange. The next two were placed in 15 cm increments below. Sensors left on the copper coil pipe started again at the beginning of the tube (Sensor T4) and spaced linearly down the tube 144 cm apart (sensors T5-T8). Figure 2.9 illustrates the location of the new sensors.
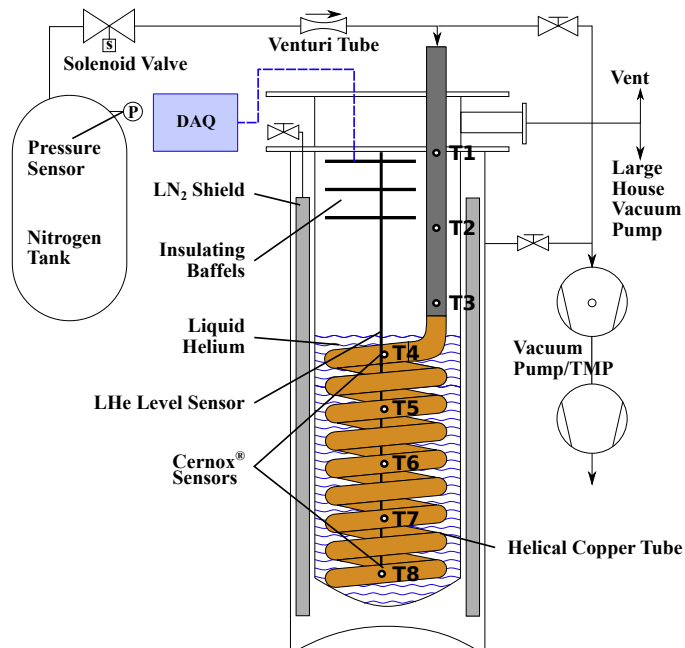


Figure 2.9: Schematic of the helical tube system with the sensors moved to new locations.

After moving the sensors, the experiments were repeated. From the data, some of the sensors were cold enough to condense nitrogen. Sensors T2 was about 17 K for both He I and He II, and sensor T3, the lowest sensor, read 4.8 K for the He II and 3.0 K for He II. Most significant difference occurs in the first sensor, T1, which was approximately room temperature for He I, but less than

60 K for He II indicating a shift in condensation point was occurring. Figure 2.10 shows the temperature profiles during an experiment He II after shifting the temperature sensors to monitor the upper temperature profile. This data does not support shifting He II's in condensation point by 38 cm is valid, but it does indicate precise temperature control above the liquid level is critical for systematic measurements comparing He I and He II.
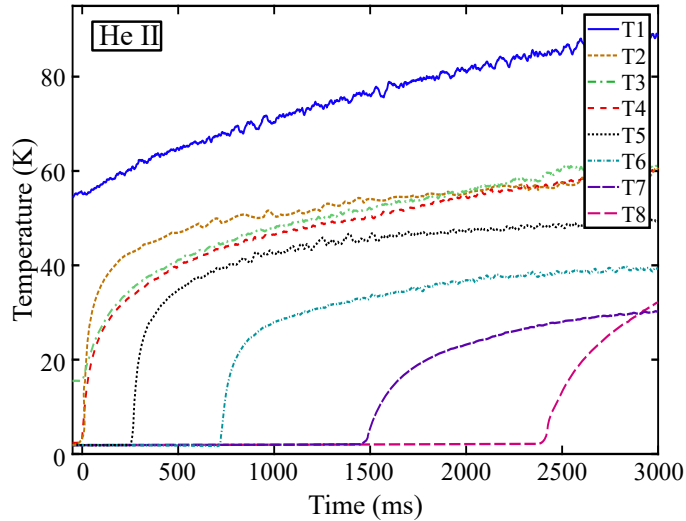


Figure 2.10: Temperature profiles of He II above the liquid level during a run.

## 2.4  Secondary Upgrades

The above results showed there is a need to control the temperature profile in the upper section of the tube. To solve this issue, a vacuum shield with multi-layer insulation (MLI) was added around the upper section of the tube. Additionally within the tube, a simple kapton film heater with a Cernox™ sensor were installed such that the wall temperature at the exit of the vacuum jacket was controlled. Temperature was controlled using a Lakeshore 340 Temperature Controller and the control sensor was positioned 3.5 cm above the copper elbow stainless transition. To verify there was no condensation in the upper section of the tube, three additional E-type thermocouples were spot-welded to the inner tube's surface at 6.5 cm 26.5 cm and 46.5 cm above the copper elbow stainless transition. Additionally, another Cernox™ bath temperature sensor was added for the He II runs such that the bath temperature could be monitored better as it warmed. Figure 2.11 (a)

shows the overall system schematic after the upgrade and Figure 2.11 (b) shows a picture of the vacuum jacket and helical assembly after assembly.
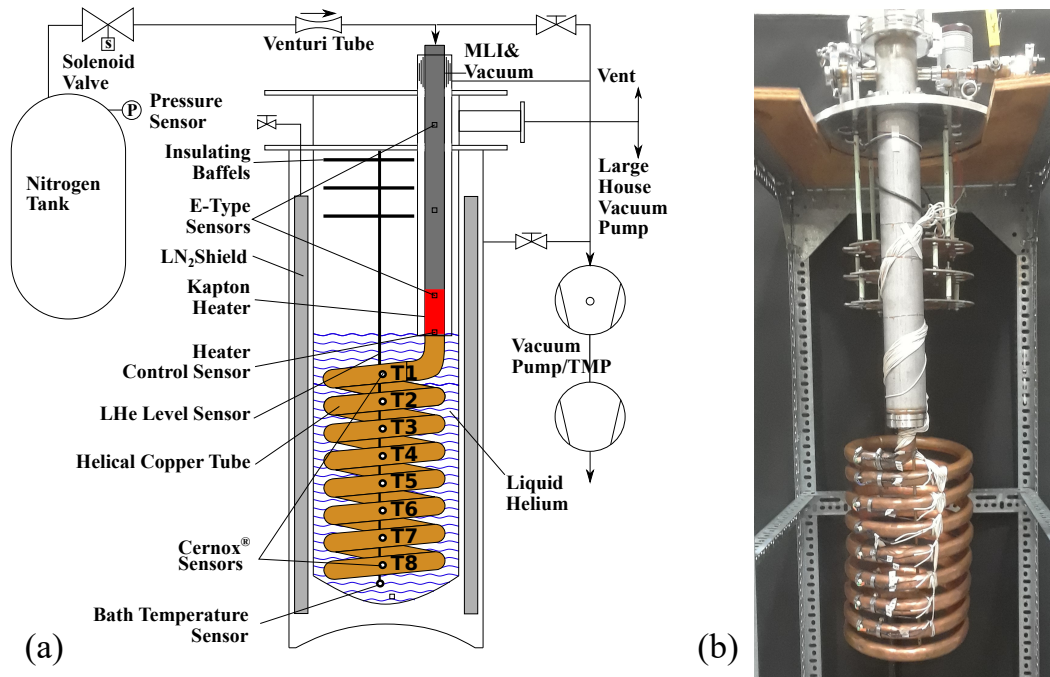


Figure 2.11: Overall system schematic after adding a vacuum jacket (a) and (b) picture of helical tube with the new insulation after assembly.

After fabrication, the 100 kPa nitrogen reservoir tank pressure experiments were repeated using the same procedure as previous experimental runs. During the experiment, the temperature controller was set to 77 K, which corresponds to condensation temperature of nitrogen at 1 atm. For the insulated pipe runs, temperatures were approximately the same for both He I and He II runs and from upper to lowest read 250 K, 210 K and 150 K, which are all above the condensation point of nitrogen. This is significantly different than the non-insulated temperature profiles of 60 K, 15 K and 3 K. These results also indicate that the condensation point is now at the exit of the vacuum tube for both He I and He II. Figure 2.12 illustrates this cold temperature profile for a He II experimental run.
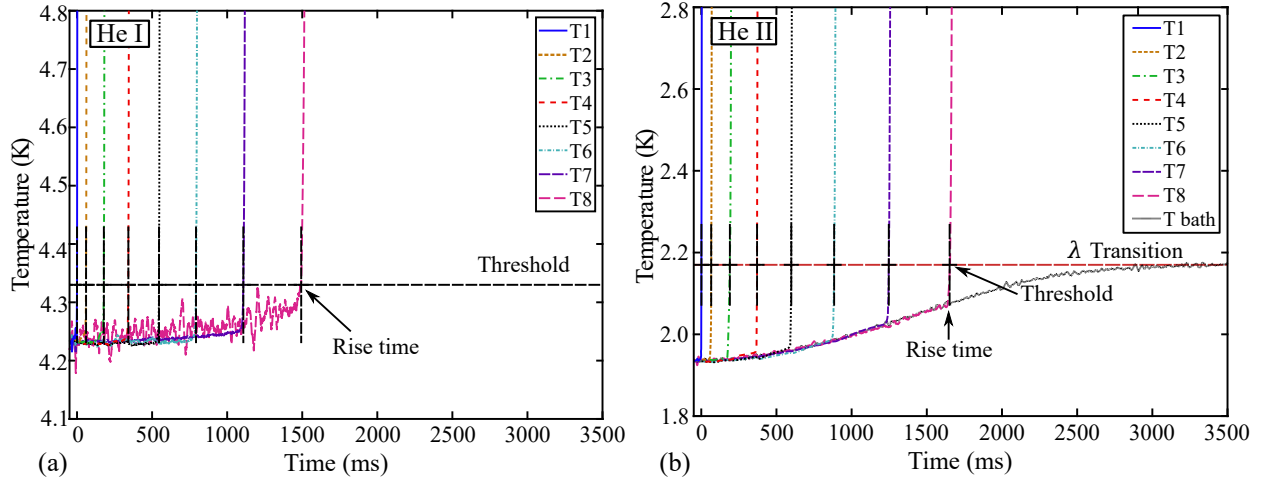
Figure 2.12: Temperature profiles for insulated He I (a) and He II (b) experiments with 100 kPa tank pressure with new insulation jacket [43].

From this data, rise time for sensor T8 for He I was about 1500 ms, and for He II, it was about 1600 ms. For non-insulated tube, seen in Figure 2.6, He I was about 1400 ms and He II was about 2000 ms. This data indicates that there is still a stronger deceleration effect in He II, but it is not as strong as it initially appeared. Continuing using Dhuley and Van Sciver's procedure to characterize the propagation slowing effect, exponential curves were again fit for insulated He I and He II as well as non-insulated He I and He II. Condensation point for the non-insulated case was set to be the at the exit of the vacuum jacket which is also the liquid level and the stainless-copper elbow transition for the non-insulated cases. The threshold level for He I was again at 0.1 K over the bath temperature which was just above the sensor noise. The threshold for He II was set at 2.17 K, which was again the same as the non-insulated case. Figure 2.13 shows the empirical curves fit from the experimental data and show that the slowing curves are indeed much closer together. Continuing the analysis, the decay time, decay length, and entrance velocities were again calculated in Table 2.4. From this calculation it can be seen that the entrance velocities are much closer together for the insulated case as compared to the non-insulated cases. Cumulatively, this shows that data is consistent and is no longer affected by variations in upper tube temperature. This consistency will allow confidence in the systematic studies and modeling comparison in the following chapters.
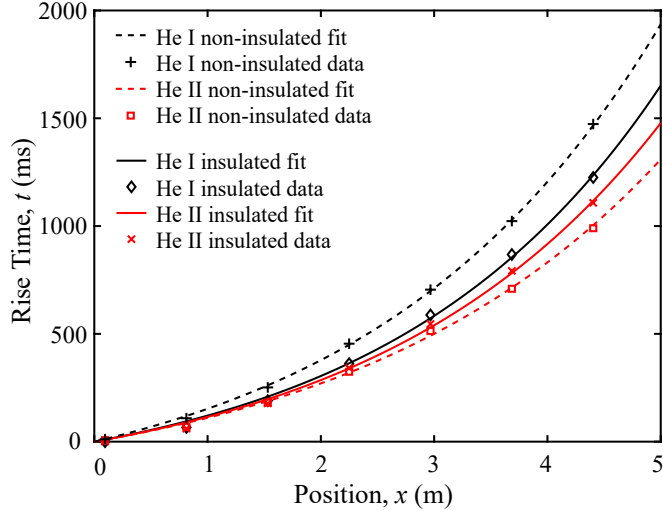
Figure 2.13: Comparison of He I and He II rise time curves with and without insulation for 100 kPa backing tank pressure [43].

Table 2.4: Regression fit coefficients and inlet velocities based on a 38 cm shift in the assumed condensation point for He II at 100 kPa [43].

|  | a (s) | b (m) | $v_o = b/a$ (m/s) |
|---|---|---|---|
| Non-insulated He I | 0.247 | 2.71 | 11.95 |
| Non-insulated He II | 0.318 | 2.55 | 8.03 |
| Insulated He I | 0.237 | 2.53 | 10.66 |
| Insulated He II | 0.286 | 2.67 | 9.30 |

## 2.5   Systematic Study Results

For the upgraded system with the vacuum jacket, systematic studies were conducted in both He I and He II for 50 kPa, 100 kPa, 150 kPa and 200 kPa nitrogen reservoir tank pressure specifically to look at the effect of mass flow on the gas propagation. Surface temperature results for all He I experiments are shown in Figure 2.14. From this figure, one can see the temperature profiles behave similarly for all pressures. As the gas front within the tube arrives at the location, a sharp, almost vertical, temperature spike is seen on the surface. It can also be seen that the gas will propagate rapidly for the higher mass flow rates, Figure 2.14 (d), compared to the lower mass flow rates, Figure 2.14 (a).
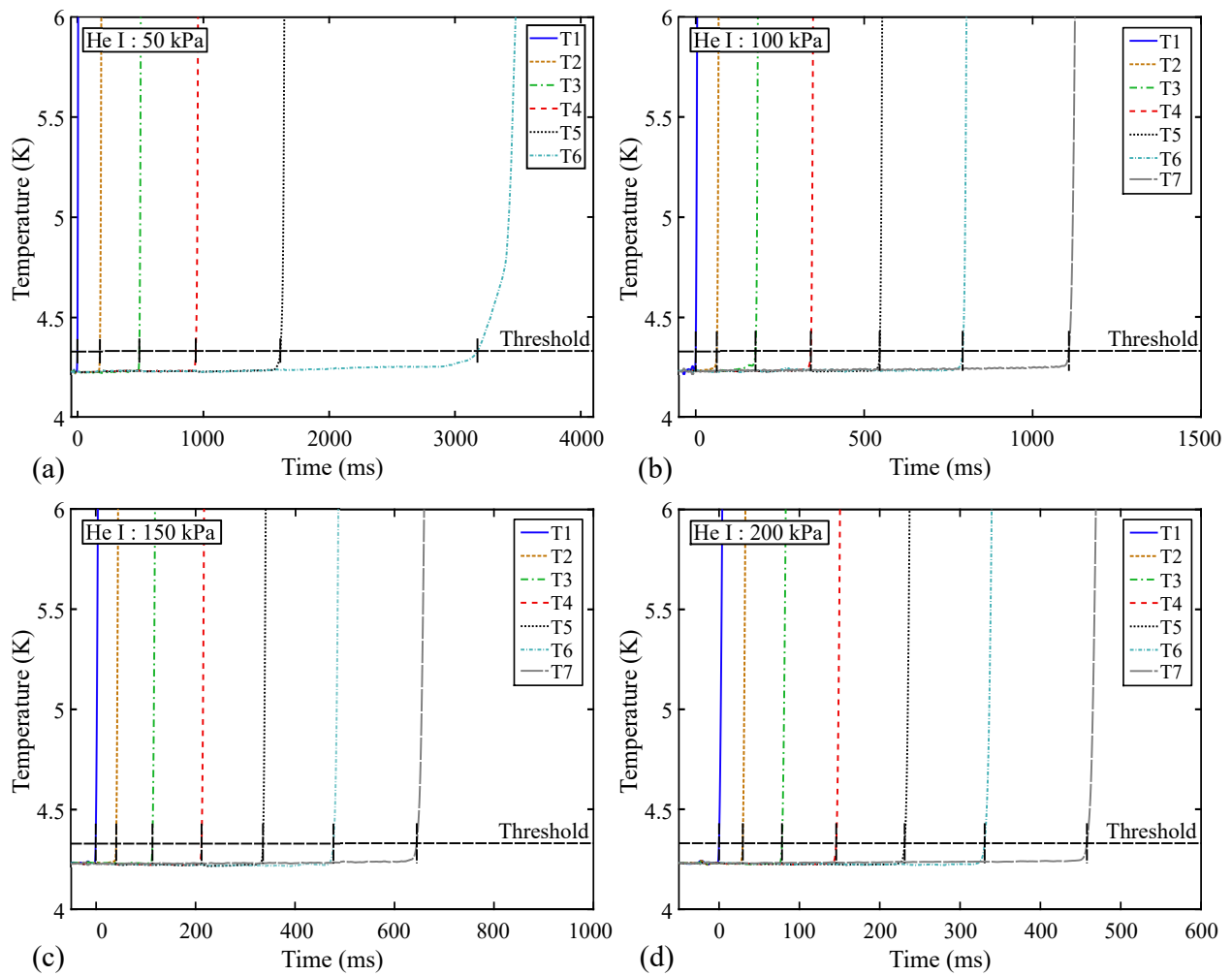
Figure 2.14: Surface temperature profiles for systematic studies in He I for (a) 50 kPa, (b) 100 kPa, (c) 150 kPa, and 200 kPa.

This different slowing can more clearly be observed by again taking a threshold value above the bath temperature and looking at the rise times of each of these curves. Figure 2.15 clearly shows the faster propagation of the high mass flow rates compared to the lower mass flow rates. Condensation plays a much more significant role in the low mass flow rate cases compared to the high mass flow cases. Again note, the empirical fits presented in this figure are for visualization of the exponential slowing effect at different mass flow rates and do not have a physical basis.
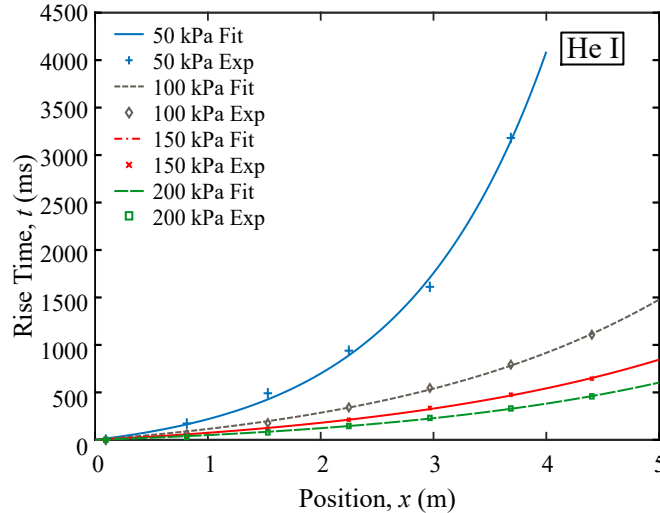


Figure 2.15: Rise time versus position for systematic studies in He I.

Studies in He II are most relevant for particle acceleration operation. Therefore, similar systematic studies were also conducted for He II. Surface temperature results for all He II results and the bath temperature are shown in Figure 2.16. For all cases a slight increase in bath temperature can be seen, but the bath temperature rises more for the 50 kPa case compared to 200 kPa case due to longer experimental time. These figures also show similar surface temperature curve behavior as the He I profiles. As the gas reaches the location within the pipe a sharp, almost vertical, temperature rise is observed. Rise times are again extracted at the threshold value of 2.17 K for the various mass flow rates and are presented in Figure 2.17. Again, it shows that the low mass flow rates are highly effected by the condensation upstream, and the higher mass flow rates do not slow as significantly.
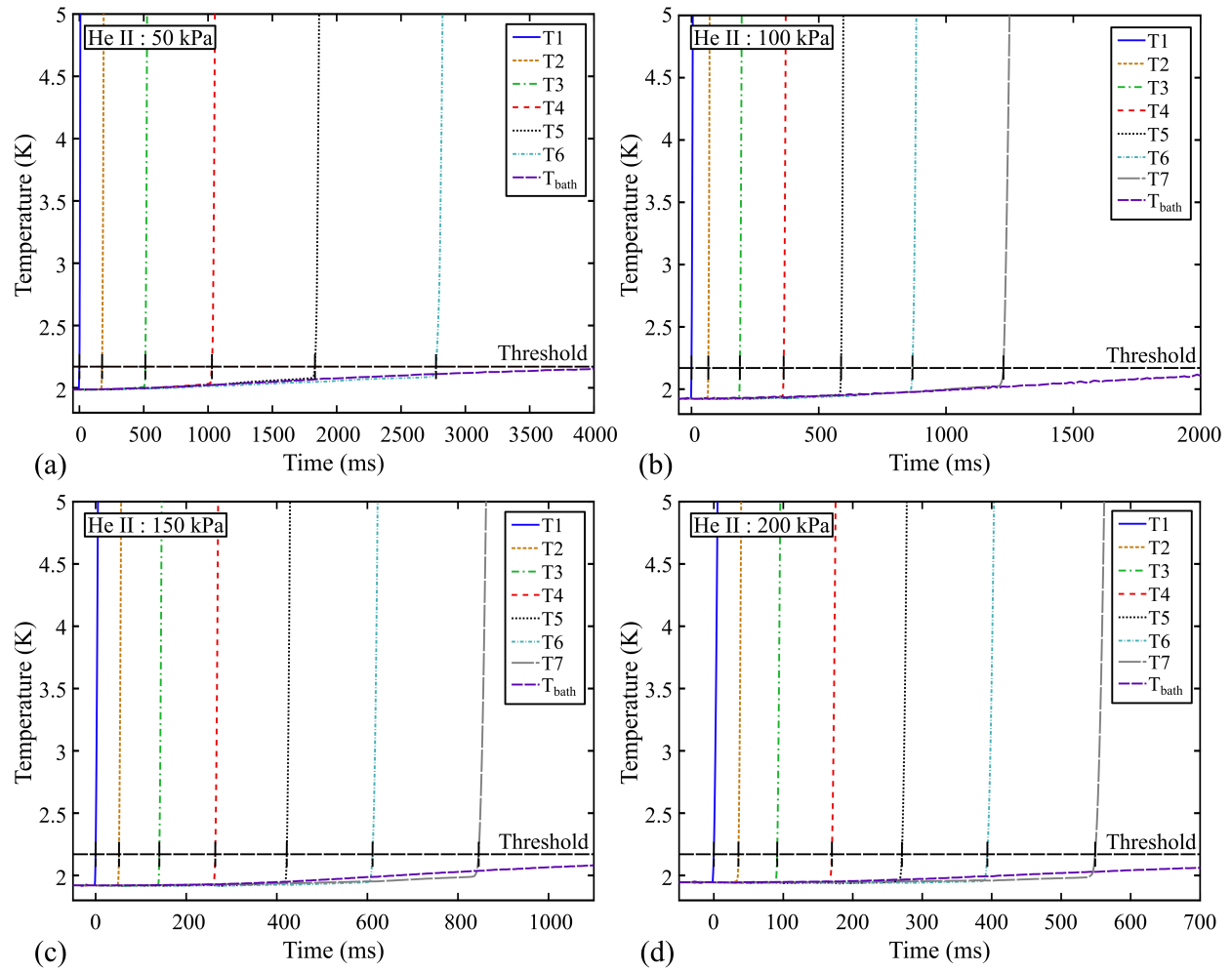
Figure 2.16: Surface temperature profiles for systematic studies in He II for (a) 50 kPa, (b) 100 kPa, (c) 150 kPa, and 200 kPa.
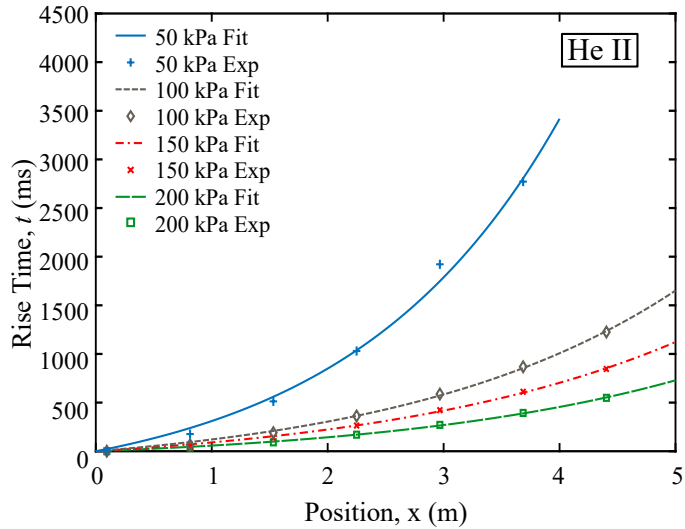
Figure 2.17: Rise time versus position for systematic studies in He II.

## 2.6   Summary

This chapter discussed the development of new experimental facilities in the NHMFL Cryogenics lab which allow for the systematic and consistent study of vacuum break in a liquid helium cooled tube. Chapter begins by discussing Dhuley and Van Sciver's straight tube setup and issues it faced with regard to limited sensor coverage along the pipe wall. To solve this, a new helical based tube design was proposed then built. Initial results indicated there was a flaw in the design due to condensation occurring above the LHe level. To solve the initial design oversight, an insulating vacuum jacket was added to the tube above the liquid level. A heater and temperature controller ensured that this jacketed portion of the pipe would not condense nitrogen. Data obtained from the insulated system indicated that condensation above the liquid level was indeed a problem, and it was resolved with the insulation upgrade. Additionally, it showed that He II still shows a stronger slowing effect than He I. Finally, results illustrated that the data is reliable and can be used in studies and model development for both He I and He II, which occurs in the following chapters.

# CHAPTER 3

# VACUUM BREAK IN HELIUM I

This chapter begins by discussing Dhuley's analysis and its weaknesses. After, it describes a new theoretical model which fully couples heat, momentum and mass transfer to simulate the physics of a vacuum break in a helium I cooled tube. This model is then compared to actual experimental data to validate and tune the model. Other useful information on gas propagation behavior and frost layer growth are also extracted from the model, which could be useful to particle accelerator facilities. Contents of this chapter have been peer reviewed and published in [44, 45].

## 3.1    Prior Conservation of Mass Analysis

Dhuley and Van Sciver analyzed one dimensional tube flow based on the conservation of mass to qualitatively describe the observed deceleration of the nitrogen gas ($GN_2$) front in a LHe cooled tube. Additional details and expanded derivations can be found in [39–41]. To summarize, similar to their experimental setup, the analysis assumed copper tube, with a diameter $D$, was fully evacuated and cooled with He I at 4.2 K. At time, $t = 0$, vacuum is broken at the beginning of the tube located at $X = 0$. $X = 0$ corresponds to the condensation point of the gas, which for the experiments, was the liquid level and the position of the first sensor. After the valve opens, $GN_2$ was assumed to rush into the tube at constant rate equal to the averaged mass flow of the experiment, $\dot{m}_{in}$. The gas inside of the cold tube starts to condense on the walls at a local rate of $\dot{m}"_{dep}(X,t)$, and forms a propagating wave at location $X = x$. Due to continuous condensation after the front and expansion into vacuum, a density gradient will form, $\rho(X,t)$. The density at the gas front is $\rho_x$. The speed of $GN_2$ front, $v|_x$, can be estimated by rearranging the mass conservation equation in the form of Eq. 3.1. Relevant parameters and the gas deposition process is illustrated in Figure 3.1.

$$v|_x = \frac{\dot{m}_{in} - \pi D \int_0^x \dot{m}''_{dep}(X,t)dX}{\frac{\pi D^2}{4}\rho|_x} \tag{3.1}$$
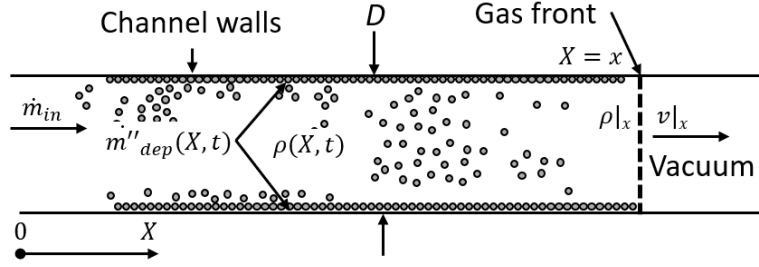
Figure 3.1: Illustration of the tube geometry and initial conditions used in Dhuley's analysis of vacuum break in 4.2 K He I cooled tube [44].

Using Eq. 3.1 the observed deceleration of the $GN_2$ front can be qualitatively explained. Total deposition rate along the tube (represented by $\pi D \int_0^x \dot{m}''_{dep}(X,t)dX$ term in Eq. 3.1) increases with time because there is more area to condense upon as the $GN_2$ propagates down the tube. If the mass deposition increases, then the wave front velocity, $v|_x$, will drop. If mass coming changes, e.g., due to buffer tank pressure drop, velocity will also proportionally change.

This analysis qualitatively explains the slowing down of the gas front, but there are a number of weaknesses which need to be addressed:

First, there is an issue with the density term, $\rho_x$, within Eq. 3.1. At the true gas front, the density is almost zero, $\rho_x \approx 0$, which causes $v|_x$ to diverge. In order for this velocity not to diverge, one has to set an arbitrary finite density. Therefore, the calculated velocity will depend on the density choice of that boundary.

Another issue, Dhuley and Van Sciver proposed an exponential decay model of $v = v_o e^{-x/b}$ to describe the slowing of the velocity seen in their experiments. However, there is no direct or quantitative link between that experimental exponential model and the theoretical conservation of mass analysis proposed in Eq. 3.1.

Next issue is another missing link between experimental and model. Experimentally, Dhuley and Van Sciver measured both temperature and pressure, and they found that measuring surface temperature provided a faster response due to better sensor sensitivity. Measured pressure can be directly linked to density of the gas molecules inside the tube, but surface temperature can not. Furthermore, any type of sensor will be limited by their sensitivity. The sensors require gas

density within the tube to increase to a threshold in order to be measured. The true front of the propagating gas front will be beyond the sensor when a response is measured.

Another issue, after the initial GN$_2$ front passes, a mono-layer of nitrogen molecules will coat the entire inner surface, but condensation will not stop until an equilibrium point is reached. The building nitrogen frost layer could induce significant temperature difference between the condensation interface of the solid nitrogen (SN$_2$) and the actual copper wall temperature. This in turn would affect the gas propagation. Dhuley's propagation velocity analysis does not incorporate the effect of a growing of the frost layer.

Finally issue, the mass enters the system through a venturi and undergoes an isentropic expansion into vacuum until it reaches the condensation point downstream. Eq. 3.1 nor Dhuley and Van Sciver's other analysys address if there is a significant effect of this warm section on the gas mass flow and other physical properties before the condensation point.

Dhuley and Van Sciver's analysis was simplified for qualitative analysis, but in order to accurate capture the physics of a vacuum break in a LHe cooled tube and relate them to the experimental observations, a new more complex theoretical model was needed. This model had to couple heat transfer, gas dynamics, and condensation effects together in order to build a more complete picture of a vacuum break event.

## 3.2    New Theoretical Model

### 3.2.1    Gas Gynamics

Modeling the gas dynamics during a sudden vacuum break is critical to understanding the full process. To describe the dynamics of the GN$_2$ as it propagates down the tube, the velocity and two thermodynamic properties are needed. With three unknowns, three equations are needed to describe the process. Three equations are derived from the conservation laws of mass, momentum, and energy as well as the equation of state, i.e., ideal gas law.

**Gas Conditions.**    The mean free path of a gas molecule, $l$, will determine if the gas rushing in the pipe is in the free molecular regime or the continuum regime. It is calculated by: $l = (n_p A_{cs})^{-1}$ where $n_p$ is the number of particles per unit volume, and $A_{cs}$ is the effective cross-sectional area for collision [48]. Free molecular regime is characterized by a mean free path larger than the container they are in, which is on the order the diameter of the copper pipe (approximately 2 cm). In the free

molecular regime, gas molecules collide with the pipe walls much more frequently than each other. The continuum regime is the opposite, with smaller mean free paths, gas molecules will collide with each other much more frequently than the walls. To distinguish between these two regimes, one needs to look at the Knudsen number, $K_n$, which is calculated by: $K_n = l/D$ where is the diameter of the pipe or a characteristic length scale. A $K_n < 0.1$ indicates the flow is in the continuum regime, and a $K_n > 10$ indicates the free-molecular regime [48]. The free molecular regime generally occurs at pressures less than $10^{-3}$ Torr at room temperature. For a typical experiment, pressures are on the order of 10-100 Torr within the pipe. Therefore, the molecules have a mean free path on the order of 1 $\mu$m and a $K_n \gg 10$, so the flow is in the continuum regime.

Next, thermal equilibrium of the gas as it propagates is important characterize. Thermalization time, $t_{th}$, of the gas can be calculated by [48]: $t_{th} = l/\bar{v}_{th}$, where $\bar{v}_{th}$ is the mean thermal velocity of the molecules. It is calculated by: $\bar{v}_{th} = \sqrt{8k_B T_g/(\pi M_g)}$, where $k_B$ is the Boltzmann constant, $T_g$ is the absolute temperature of the nitrogen gas, and $M_g$ is the molecular mass of the gas molecule. For nitrogen around room temperature and 50 torr, $\bar{v}_{th} \approx 470$ m/s and $l \approx 1\mu$m, so $t_{th} \ll 1\mu$s. From experimental observations, temperature variation scale is on the order of 10 ms or greater. Therefore, local thermal equilibrium across the gas segment can be assumed because the thermalization is much smaller than typical temperature variation scale.

The appropriate equation of state to use for GN$_2$ needs to be determined. In the vacuum break situation, inside the tube is always below atmospheric pressure. Looking at the comprehensibility factor of GN$_2$, one can see it approaches unity as the pressure drops below atmospheric [49]. If comprehensibility is unity, the gas can be treated as an ideal gas following the ideal gas equation of state: $PM_g = \rho_g RT_g$ where $P$ is the gas pressure, and $\rho_g$ is the gas density.

**Conservation of Mass.**    First equation needed to solve for the thermodynamic gas properties and its velocity comes from the conservation of mass. The simplified mass conservation equation for 1D pipe flow [26]:

$$\frac{\partial \rho_g}{\partial t} + \frac{\partial}{\partial x}(\rho_g v) = -\frac{4}{D_1}\dot{m}_c \tag{3.2}$$

where $v$ is the downstream velocity of the gas, and $D_1$ is the inner diameter of the tube. $x$ is the position along the tube length and $t$ is the time. The additional $-\frac{4}{D_1}\dot{m}_c$ term accounts for the loss of gas as it condenses onto the walls of the tube. The mass deposition rate of GN$_2$ per area, $\dot{m}_c$, which will vary down the tube based on local conditions.

Quantifying $\dot{m}_c$ is a small challenge to evaluate in shock tube conditions at cryogenic temperatures. Existing cryopumping research offers one solution, which is a free molecular regime deposition model based on an effective sticking coefficient, $C_{eff}$ [32, 33, 35, 50, 51]. $C_{eff}$ quantifies how effectively a gas molecule will stick to a cold freezing surface and not evaporate or bounce off. Mass condensation can be written as a function of this sticking coefficient in the form:

$$\dot{m}_c = \dot{m}_0 \cdot C_{eff} \tag{3.3}$$

where $\dot{m}_0$ is a normalization factor accounting for the $GN_2$'s collisions against the wall per unit area. It is calculated by:

$$\dot{m}_o = \frac{1}{4}\sqrt{\frac{8RT_g}{\pi M_g}}\rho_g \tag{3.4}$$

Dawson and Haygood showed that $C_{eff}$ can be modeled as [32]:

$$C_{eff} = \left(1 - \frac{P_e}{P}\right)\alpha \tag{3.5}$$

where $P_e = P_s\sqrt{T_g/T_s}$ is the equilibrium pressure, $P_s$ is the local saturation pressure at the frost-gas interface temperature, $T_s$, and $\alpha$ is the condensation coefficient which describes the probability that the gas molecule condense onto a cold interface. $\alpha$ has been measured for nitrogen and it depends on frost-gas interface temperature ($T_s$), $T_g$, and the over saturation ratio, $P/P_e$ [50]. Figure 3.2 shows an interpolation of experimental data from [50] for 300 K $GN_2$. It illustrates the dependence of $\alpha$ on $P/P_e$ and $T_s$.
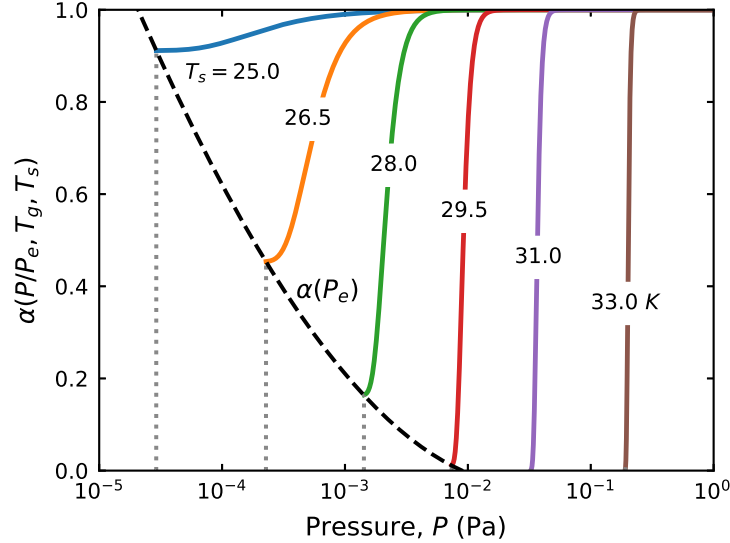
Figure 3.2: Probability of $GN_2$ at $T_g$=300 K sticking to various temperature cold surfaces as a function of gas pressure [45] (extracted from [50]).

As illustrated in the figure, there is no condensation when $P/P_e$ <1 so $\alpha = 0$. $\alpha$ will have some finite value between 0 and 1 as $P/P_e$ approaches 1. When $P/P_e \ll 1$, gas almost always sticks to the wall so $\alpha$ generally approaches unity. Extracting $\alpha$ at different gas temperatures can be accomplished by scaling the values of Figure 3.2 through the relation [32]:

$$Log(1 - \alpha) = -\frac{E}{k_B T_g} \tag{3.6}$$

where $E$ is the critical energy, which is a constant that is determined only by the gas-solid interface temperature. Though these equations the mass dynamics can be described, but $T_s$ is still unknown so it needs to be evolved through other equations.

It is important to note, this sticking coefficient model is intended for use in the free molecular flow regime, but these experiments were conducted in the continuum regime. Therefore, the sticking coefficient behavior may change due to collisions between gas molecules adjacent to the wall. There is sparse research in this niche deposition problem: Some studies exist for evacuated shock tubes with condensation at room temperature (e.g., methanol evacuated shock tube studies by Maerefat et.al. [52]), but these studies are not at cryogenic freezing temperatures. Within cryogenic temperatures there are some relevant studies, e.g., [53, 54], but they do not study nitrogen condensation.

Bosque studied continuum regime vacuum break with $GN_2$ for a liquid helium cooled surface, but did not develop a deposition model or evaluate a sticking coefficient for their observations [35]. Regardless of its limitations, results below show effective sticking coefficient model allowed for key features of the experimental observations to be reproduced. Note, this model was only used for He I analysis conducted in this chapter. Mass deposition model is updated in the next chapter to correct for this free molecular regime limitation.

**Momentum Conservation.** Second equation needed to solve for the thermodynamic gas properties and its velocity comes from the conservation of momentum. The Navier-Stokes equation for compressible fluids can be used to describe the momentum of the gas within the pipe [26]. This simulation only considers 1D flow. Also, the flow is dominated by mass deposition and inertial effects, so viscous effects can be ignored. This simplifies the momentum conservation equation for propagating $GN_2$ to:

$$\frac{\partial}{\partial t}(\rho_g v) + \frac{\partial}{\partial x}(\rho_g v^2) = -\frac{\partial P}{\partial x} - \frac{4}{D_1}\dot{m}_c v \tag{3.7}$$

where the momentum loss caused by mass deposition on the tube wall is accounted for by the addition of last term on the right hand side. Note, $\dot{m}_c$ is unknown within this equation, but as previously discussed above, it can be evaluated through its dependence on $T_s$ and local gas conditions.

**Energy Conservation.** Third equation needed to solve for the thermodynamic gas properties and the gas velocity comes from the conservation of energy. Using thermodynamics first law analysis, the energy conservation equation for the 1D propagating $GN_2$ within in the tube can be simplified to [55]:

$$\frac{\partial}{\partial t}\left[\rho_g\left(\varepsilon_g + \frac{1}{2}v^2\right)\right] + \frac{\partial}{\partial x}\left[\rho_g v\left(\varepsilon + \frac{1}{2}v^2 + \frac{P_g}{\rho_g}\right)\right] = -\frac{4}{D_1}\dot{m}_c\left(\varepsilon + \frac{1}{2}v^2 + \frac{P_g}{\rho_g}\right) - \frac{4}{D_1^2}Nu \cdot k(T_g - T_s) \tag{3.8}$$

where $\varepsilon_g$ is the specific internal energy and $k_g$ is the thermal conductivity of the gas. Within this equation, first term on the right hand side accounts for the energy lost by the gas as it condenses onto the wall. Second term is the convective heat transfer from the gas to the gas-solid frost interface. Sieder-Tate correlation is used to evaluate the Nusslet number, $Nu$, in the convective heat transfer term is evaluated by [55]:

$$Nu = 0.027 Re^{4/5} Pr^{1/3}(\mu_g/\mu_s)^{0.14} \tag{3.9}$$

39

where $Re$ is the local Reynolds number, $Pr$ is the local Prandlt number, $\mu_g$ and $\mu_s$ are the viscosity for the bulk gas and at the solid-gas interface respectively. Note, the solid frost layer interface temperature, $T_s$, is still unknown so it needs to be simultaneously evaluated with additional equations found through radial heat transfer analysis.

### 3.2.2 Radial Heat Transfer

Radial heat transfer through the wall needs to be coupled with gas dynamics in order to evolve a complete picture of what is occurring at every step: Within one slice of the tube, energy is living the gas. This energy deposits onto the wall at a rate of $q_{dep}$, passes through the frost layer into the copper wall at a rate of $q_i$, and then flows from the tube wall into the LHe bath at a rate of $q_{He}$. This process with relevant parameters is illustrated in Figure 3.3. In order to estimate $T_s$, one can
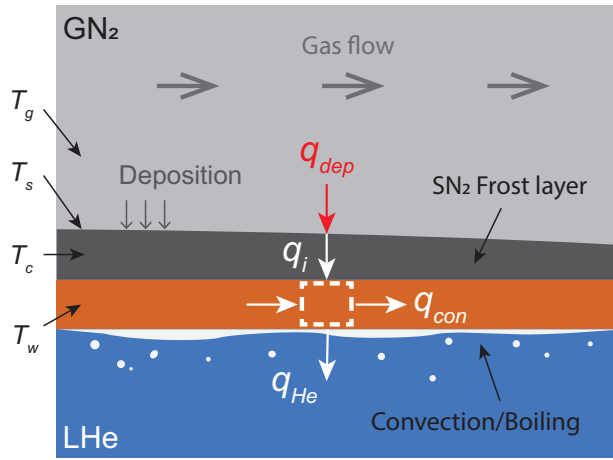


Figure 3.3: Radial heat transfer process through the He I cooled tube [45].

begin the analysis by determining $q_{dep}$. $q_{dep}$ is equal to the sum of the energy leaving the gas from convective heat transfer and from the gas as it condenses and freezes to the wall, which includes sensible heat, latent heat, and kinetic energy. Deposition heat is modeled by:

$$q_{dep} = \dot{m}_c \left[ \frac{1}{2} v^2 + \hat{h}_g - \hat{h}_s \right] + \frac{Nu \cdot k_g}{D_1} (T_g - T_s) \tag{3.10}$$

where $\hat{h}_g$ is the specific enthalpy of the $GN_2$ and $\hat{h}_s$ is the specific enthalpy of the $SN_2$. An equilibrium temperature profile is assumed for the frost layer because the thickness of this layer, $\delta$, should be small. If the profile is at equilibrium, it is linear, and the midpoint temperature is simply

40

an average of the frost-gas interface temperature and the copper wall temperature: $T_c = (T_w + T_s)/2$. An energy balance of the frost layer yields:

$$\rho_{SN} C_{SN} \delta \frac{\partial T_c}{\partial t} = q_{dep} - q_i \qquad (3.11)$$

where $C_{SN}$ is the heat capacity of the $SN_2$ layer. Heat flux into the copper wall is estimated by the conduction across the layer, which is: $q_i = k_{SN}(T_s - T_w)/\delta$, where $k_{SN}$ is the thermal conductivity of the $SN_2$ layer. Also, growth of this frost layer over time is modeled by:

$$\frac{\partial \delta}{\partial t} = \dot{m}_c / \rho_{SN} \qquad (3.12)$$

where $\rho_{SN}$ is the density of the growing solid nitrogen layer. To solve the above equations, the copper wall temperature, $T_w$, dynamics also need to be modeled. Copper tube is relatively thin and highly conductive, so it is treated as a lumped-heat-capacity system with nearly uniform wall temperature. $T_w$ can be obtained through an energy balance on the wall:

$$\rho_w C_w \frac{D_2^2 - D_1^2}{4D_1} \frac{\partial T_w}{\partial t} = q_i - q_{He} \frac{D_2}{D_1} + \frac{D_2^2 - D_1^2}{4D_1} k_w \frac{\partial^2 T_w}{\partial x^2} \qquad (3.13)$$

where $D_2$ is the outer diameter of the tube. $k_w$, $C_w$, and $\rho_w$ are the thermal conductivity, heat capacity and density of the copper tube respectively. Within the equation, energy coming in to the wall is $q_i$, energy is leaving the wall to liquid helium bath is $q_{He}$, and energy is also leaving due to conduction, which is accounted for in the last term on the right hand side of the equation. All the variables can be solved for except for estimation of liquid helium heat flux, $q_{He}$, for He I, which is discussed in further detail in the next section.

### 3.2.3   Normal Helium Heat Transfer

Particle accelerators typically use He II in their baths, but for initial simulations and experiments, He I was used to simplify the process and validate the model. He I is a normal fluid so it behaves like other classical fluid and follows the various known correlations. Boiling point of normal LHe is 4.2 K at 100 kPa. LHe has a very low latent heat (i.e., 21 kJ/kg) compared to other cryogens (e.g., nitrogen at 199 kJ/kg), which means it can rapidly boil with a small amount of heat. Rapid boiling can cause an explosive build up of pressure, which is a safety hazard [18, 56].

Like other classical fluids, there are four heat transfer regimes within He I: convective cooling (a), nucleate boiling (b), transition regime (c), and film boiling (d) illustrated in Figure 3.4.

41

Figure 3.4 (e) is an example graph of the heat flux and temperature relation for the different regimes. It should be noted that values presented and mentioned below can change depending on local saturation temperature at depth, the surface conditions, geometry, and orientation [18].
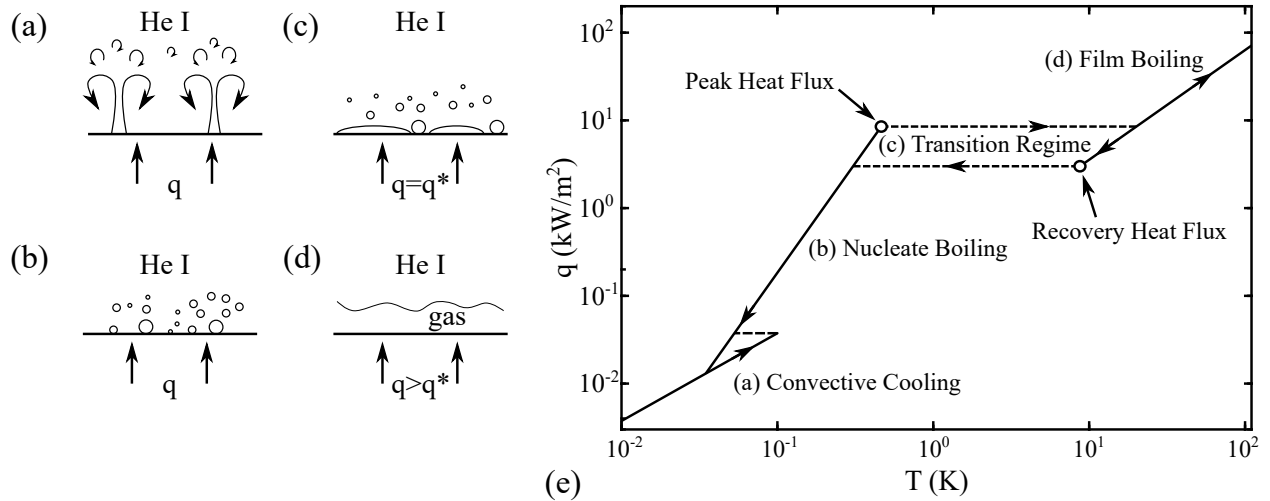


Figure 3.4: Heat transfer regimes in a He I pool: a) natural convection, b) nucleate boiling, c) transition to film boiling, d) film boiling. e) He I heat transfer diagram of correlations adopted for this model.

**Natural Convection Regime.** Natural or free convective cooling, illustrated in Figure 3.4 (a), is characterized by the flow of a fluid induced by thermal expansion and buoyancy forces. This is typically the heat transfer mechanism in stagnant low heat flux He I baths. Convective cooling does not generate any bubbles and the helium near the surface stays as a liquid. Convection occurs at a heated surface which has heat flux less than 10 W/m$^2$ and a temperature difference, $\Delta T$, between the surface, $T_w$, and bulk fluid, $T_b$, of less than 0.1 K [18]. Typical correlation to describe the convection regime for classical fluids is in the form of Newton's law of cooling:

$$q_{He} = h_c(T_w - T_b). \tag{3.14}$$

where $h_c$ is the convection coefficient. For He I, $h_c$ has been measured in the range of 0.25-0.5 kW/m$^2$K [57]. For purposes of modeling in the simulation, a convection coefficient of 0.375 kW/m$^2$K is used based on those experimental measurements. Model also assumes all $\Delta T$ less than 0.1 K were treated as natural convection.

**Nucleate Boiling Regime.** Nucleate boiling regime, illustrated in Figure 3.4 (b), is characterized by the formation of gas bubbles on the heated surface. These bubbles may detach and raise allowing new fluid to take the gas's place, which causes periodic wetting of the surface. This efficient mode of heat transfer occurs when $\Delta T$ is greater than 0.1 K and roughly less than 0.5 K [18]. A simplified Kutateladze correlation can be used to model nucleate boiling:

$$q_{He} = h_{nb}(T_w - T_b)^{2.5} \tag{3.15}$$

For simulating the nucleate boiling, empirical heat transfer coefficient, $h_{nb} = 5.8$ kW/m$^2$K$^{2.5}$, and included $\Delta T > 0.1$ $K$, but below the peak heat flux, $q^*$ [18].

**Transition to Film Boiling Regime.** The transition regime, illustrated in Figure 3.4 (c), is characterized by a large amount of gas bubble formation reducing the ability of the surface to periodically wet itself. This is observed at the point where there is a large sudden jump in surface temperature, but has no additional heat flux. This point is known the 'peak critical heat flux,' $q^*$. At one atmosphere, the transition regime occurs approximately at temperature differences between 0.5 K and 20 K. Steady state peak heat flux has been measured experimentally at 8 kW/m$^2$ for helium at 4.2 K, but it can range from 5-15 kW/m$^2$ depending on surface orientation and local saturation conditions [18, 58]. In the case of the experimental setup, there is a variation in depth along the helical coil as well as possible effects of bubble rise on other coils. For simplicity within the model, $q^*$ was set to 7.5 kW/m$^2$.

In this transition region, it should also be noted there is a minimum film boiling heat flux which is also termed the recovery heat flux, $q_r$. This can be significantly less than the peak critical heat flux and it occurs when a stable film boiling cools down and transitions back to the nucleate boiling regime. Recovery heat flux is not relevant to current modeling and simulation because vacuum break only deals with the sudden high heat loads as the propagation front arrives at a location. Further information on recovery heat flux can be found in [18].

**Film Boiling Regime.** Finally, if the heat flux continues to increase, all the bubbles merge and form a gas layer or film, i.e., film boiling illustrated in Figure 3.4 (d). In film boiling, the heat is conducted and radiated across the vapor film into the bulk fluid [18]. For modeling the steady film boiling regime, the Breen-Westwater correlation is commonly used [59]:

$$q_{He} = B_w(T_w - T_b)^{5/4} \tag{3.16}$$

where $B_w$ is a constant that depends on the surface conditions. The model uses uses an optimal $B_w$ value such that the variation between experimental and simulated the rise times are minimized. Combing all heat transfer modes, a heat transfer map for He I used in the following simulations is shown in Figure 3.4 (e).

**Transient Heat Transfer.** This section has so far described the heat transfer processes under steady state conditions. Although, a vacuum break scenario is a highly transient process. Transient pool boiling model ideally would be implemented within the simulation. This is done through the use of the 1D radial heat diffusion equation into the bulk fluid [18]:

$$\frac{\partial^2 T_b}{\partial r^2} + \frac{1}{r}\frac{\partial T_b}{\partial r} = \frac{\rho_b C_b}{k_b}\frac{\partial T_b}{\partial t} \tag{3.17}$$

where $r$ is the distance from the tube surface. Also, $k_n$, $\rho_n$, and $C_n$ are the thermal conductivity, density and heat capacity of He I respectively. However, the simulation is complex and needs to solve several differential equations simultaneously. Additionally, there will be effects from adjacent tubes in the helical structure. To avoid another layer of complexity and simplifying the model, this dissertation uses the above simple correlations for steady state conditions.

To validate this steady state or psuedo-steady state assumption is not unreasonable, it is important to know how long it takes to transition from unsteady transient to steady state boiling. To determine this characteristic time scale, $\Delta t^*$, one needs to look at the energy it takes to vaporize a fluid layer, $\Delta E^*$ with thickness, $\delta_{tr}$ or [18]:

$$\Delta E^* = q_a \Delta t^* = \delta_{tr} h_{fg} \tag{3.18}$$

where $h_{fg}$ is the latent heat of LHe and $q_a$ is the applied heat flux. From this, $\Delta t^*$ can be roughly approximated by [18]:

$$\Delta t^* \approx \rho_n h_{fg} \delta_{tr}/q_a \tag{3.19}$$

Using saturated liquid properties for LHe at 100 kPa and 4.2 K ($\rho_n = 125 kg/m^3$, $h_{fg} = 21$ kJ/kg), an assumed film thickness of $\delta_{tr} \approx 10\mu m$, and an applied heat flux of 8 kW/m$^2$ (slightly above the assumed peak heat flux of 7.5 kW/m$^2$ in the model), the transition time will be approximately 3 ms. More accurate estimations were conducted by Schmidt indicated [60]:

$$\Delta t^* = 0.01 q_a^{-2.8} \tag{3.20}$$

where $q_a$ is in W/cm$^2$ and $\Delta t^*$ is in seconds. Again assuming an applied heat flux of 8 kW/m$^2$ (0.8 W/cm$^2$), it would take approximately 10 ms to transition to film boiling. The experimental time scales are larger and range from roughly 0.5 to 4.5 seconds for rise times the last sensor, which means psuedo-steady state assumption is reasonable. Additional details of transient boiling in He I can be found in [18].

### 3.2.4 Geometry, Boundary, and Initial Conditions

To be able to compare the numerical results to the experimental data, the geometry of experimental system is used within the simulation. A one dimensional simulation is conducted for an evacuated tube with length of 6.45 m, a diameter of 25.4 mm, and a thickness of 1.25 mm. The full length of the tube was assumed to be evacuated to $10^{-6}$ Pa. First 0.57 m of the tube represented the vacuum jacketed 304 stainless steel tube. Temperature profile of the upper section was set to match the upper E-type thermocouple positions and readings for the experiments (i.e., 250 K, 210 K and 150 K). The stainless tube entrance was set at room temperature, 298 K, and the exit was 77 K due to the heater and temperature controller. Therefore, there was no condensation in the first 0.57 m of the tube. The stainless steel segment was attached to the last 5.88 m copper tube, which represents the helical copper coil immersed in LHe. He I experiments were conducted at atmospheric pressure, so the initial copper wall was set to the corresponding saturation temperature of LHe, 4.2 K. Physical properties of copper and stainless steel were extracted from literature [19, 61].

At $t = 0$, vacuum was broken simulating the opening of the fast-acting solenoid valve between the venturi and the nitrogen buffer tank. Inlet GN$_2$ mass flow into the evacuated tube was set to match to the experimental run's time-varying mass flow (See Section 2.3.1). Flow into the tube is choked due to the venturi, so inlet flow velocity, $v(0,t)$, was assumed to be at the local speed of sound. The inlet gas density, $\rho_g(0,t)$ can be calculated using the known mass flow rate and the relation: $\dot{m}(0,t) = \rho_g(0,t)v(0,t)\pi D_1^2/4$. Inlet pressure, $P_g(0,t)$, can be calculated using ideal gas law and incoming gas temperature, $T_g(0,t)$=298 K. The end of the copper tube is capped. However, an open-ended boundry condition was used to avoid complications caused by reflected shocks or reflected wave propagation. Figure 3.5 shows an illustration of the relevant boundary conditions within the 1D tube model.

The density, $\rho_{SN}$ and thermal conductivity, $k_{SN}$, of the growing solid nitrogen on the tube surface highly depends on the surface temperature and mass deposition rate. In free molecular
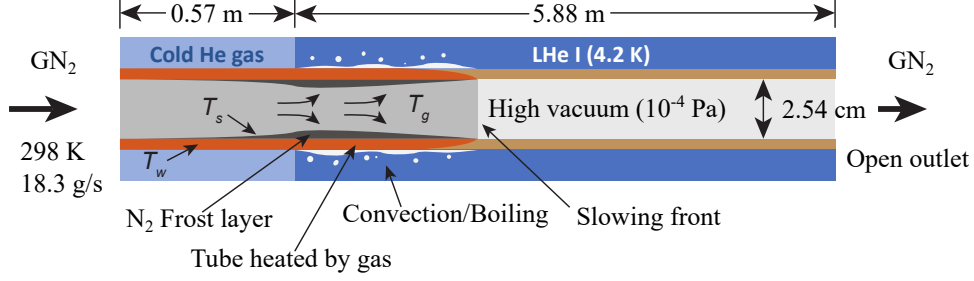
Figure 3.5: Illustration of the tube geometry and initial conditions used in simulating vacuum break in 4.2 K He I cooled tube [45].

regime and low temperatures, the solid nitrogen layer will be less dense and snow like due to many voids in the disordered polycrystalline structure. At higher temperatures and large deposition rate, a more solid ice like closely-packed crystalline structure can form because of higher molecule mobility [62, 63]. These vacuum break experiments are conducted in the continuum regime where large rapid mass deposition occurs, and the wall temperatures raise from 4.2 K to around 50 K within several milliseconds. Related research in a similar situation showed that the density and thermal conductivity of the frozen nitrogen will be higher and are similar those of $SN_2$ formed from liquid phase [54, 62]. With this in mind, $SN_2$ property values observed in [62] were chosen for the simulation.

## 3.3    Results and Discussion

The above 1D gas dynamics equations, radial heat transfer equations, physical correlations and initial conditions were coupled together in a numerical simulation using a two-step first-order Godunov-type finite-difference method [31]. Godunov-type scheme is an implicit type numerical method which solves all the gas properties (i.e., $\rho_g, \varepsilon_g, T_g$, etc.), frost layer properties, heat fluxes, and wall conditions at a half spacial step $(x + \frac{1}{2}\Delta x)$, and then uses them to predict the full steps results $(x+\Delta x)$. Basic illustration of this type of numerical scheme is illustrated in Figure 3.6. This method was chosen because it has shown to be reliable in solving nonlinear hyperbolic equations [64].
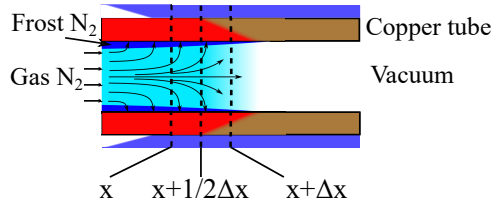
Figure 3.6: Basic numerical scheme for Godunov type finite-difference method.

### 3.3.1 Model Validation

Wall surface temperature was used to chart the propagating GN$_2$ for the experiments. For 100 kPa starting nitrogen buffer tank pressure, Figure 3.7 shows the temperature profile curves at various locations along the tube. The simulated curves contain similar features as the experimental
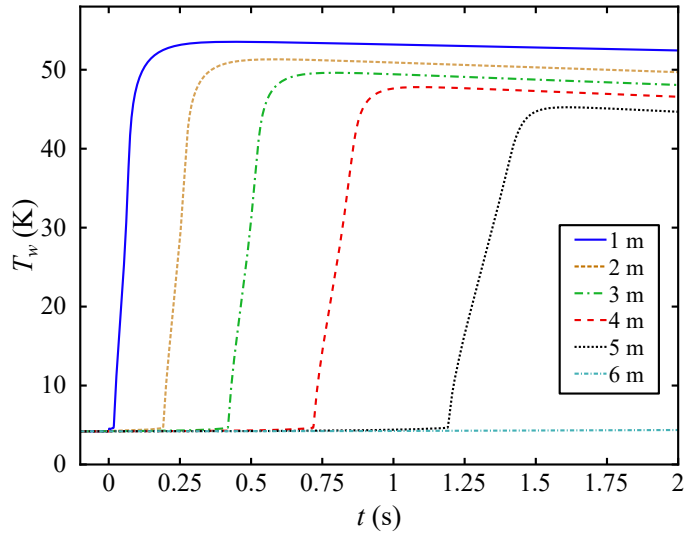


Figure 3.7: Temperature profiles for He I 100 kpa tank pressure simulation at different spacial slices [45].

observations. Temperatures start off at the bath temperature. As the gas propagates down the tube, there is a sudden rise to a maximum between 40 K and 60 K at the approximate location of the gas front. There is also a slight downward trend in the maximum temperature as the frost layer builds and the mass flow rate drops. The figure also shows that the gas front is propagating rapidly at the beginning with the adjacent temperature profiles rising quickly, but later downstream, the profiles become more spaced.

47

Most important feature is the timing of the temperature spike because this marks the location of the GN$_2$ propagation wave front. An overlap zoomed comparison of simulated temperature responses with experimental results at locations where the sensors are installed is presented in Figure 3.8. This figure shows reasonable agreement between the temperature profiles except for the last sensor location. Similar to the experiments, an arbitrary threshold value in the near vertical region can be set (i.e., 4.7 K), and the apparent gas front arrival can be plotted, as shown in Figure 3.9. Again, one can see there is reasonable agreement between experimental temperature profiles and simulated results (except for the last sensor). This last sensor difference could be the result of gas front reflection at the end of the experimental setup, or differences due to physical issues such as bubbles from coils deeper in the LHe bath affecting the boiling of those above them.
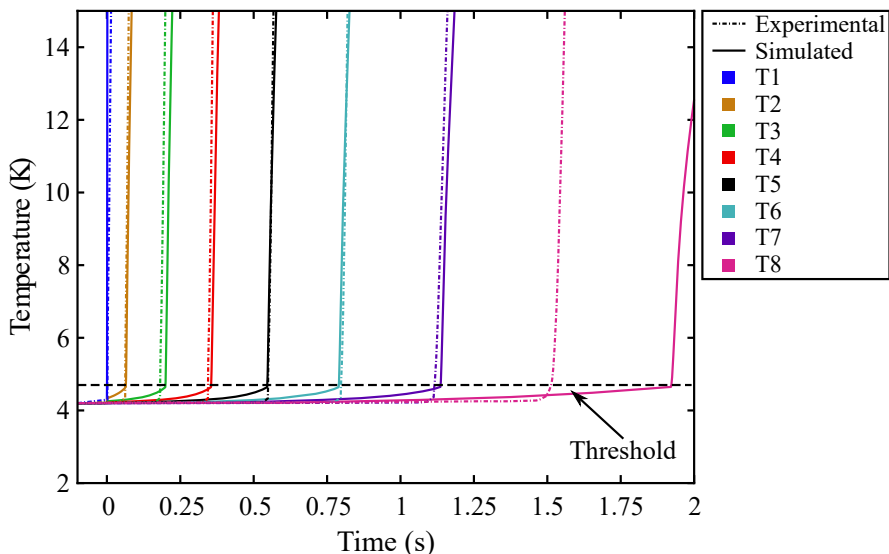


Figure 3.8: Simulated wall temperature profiles (solid lines) and experimentally observed wall temperature profiles (dashed lines) for 100 kPa tank pressure [45].

For this simulation, it should again be noted that the Breen-Westwater coefficient, $B_w$, was adjusted to achieve the best match between simulation and experimental data rise times. Literature suggests a $B_w$ value of 0.013 W/cm$^2$K$^{5/4}$ for cylindrical heaters with over 1 cm diameter [65]. Optimum $B_w$ for this simulation was close at 0.017 W/cm$^2$K$^{5/4}$. This slight difference could be the result of increased heat transfer due to the adjacent coils in the helical structure compared to just a straight horizontal pipe. It also could indicate a different type of mass deposition model might be better to
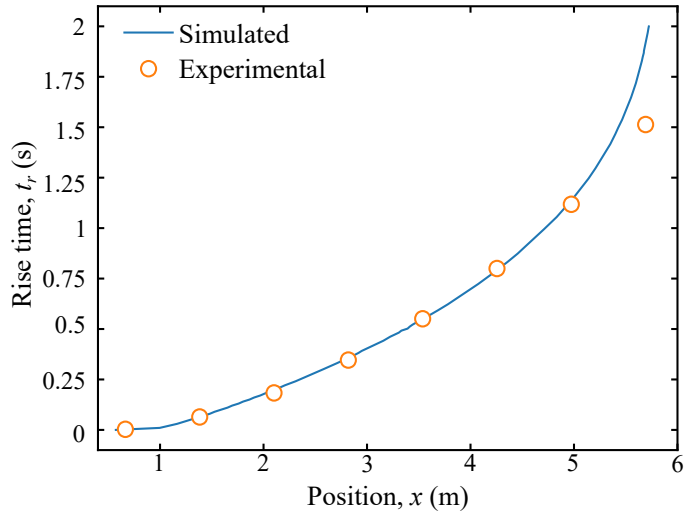
Figure 3.9: Comparison between simulated rise times and experimental rise times as a function of location for 100 kPa tank pressure [45].

reach simulating gas dynamics in the tube (i.e., the continuum based condensation model detailed in the next chapter). Depth effects could also cause changes in the local peak heat flux (depth effects are included in next chapter's He II model). In all, the simulation and experimental observations are in fair agreement with the simulations thereby supporting the validity of the model. Therefore, it can provide other useful information on behavior of nitrogen gas as it propagates and how frost layer grows in the tube.

### 3.3.2   Behavior of Nitrogen Gas

From the simulation, one can take a glimpse into the complex and interlinked physics of the $GN_2$ propagation in the LHe cooled tube. Simulation was able to address the prior raised concerns of Dhuley's analysis, i.e., the effect of the warm section of tube before the condensation point on gas propagation and why surface temperature can be used to measure gas propagation. Figure 3.10 shows various spatial properties at a number of time slices illustrating these dynamics. Figure 3.11 shows the density profiles around the entrance at several different time slices, which illustrates the effect of condensation. From these graphs, are three unique regions which can be identified: the inlet region, mass deposition region, and a leading expansion fan region.
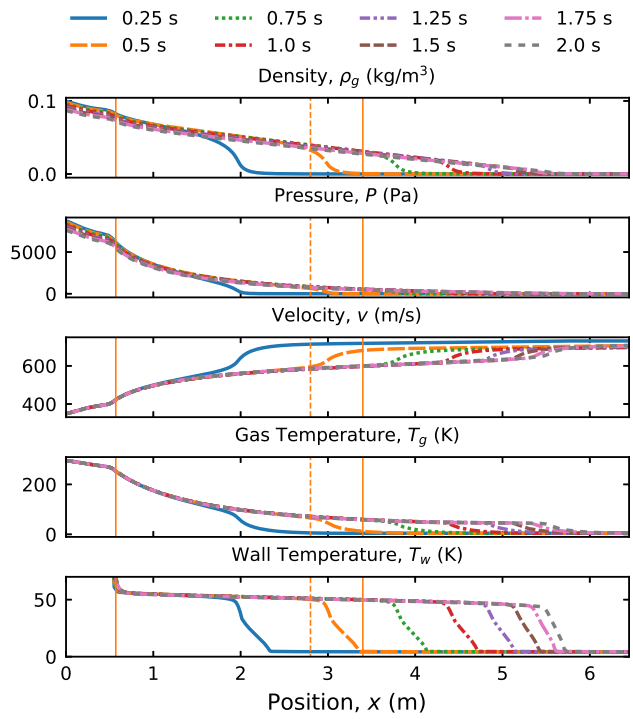
Figure 3.10: Simulation results comparing the the various spacial properties at several time slices [45].
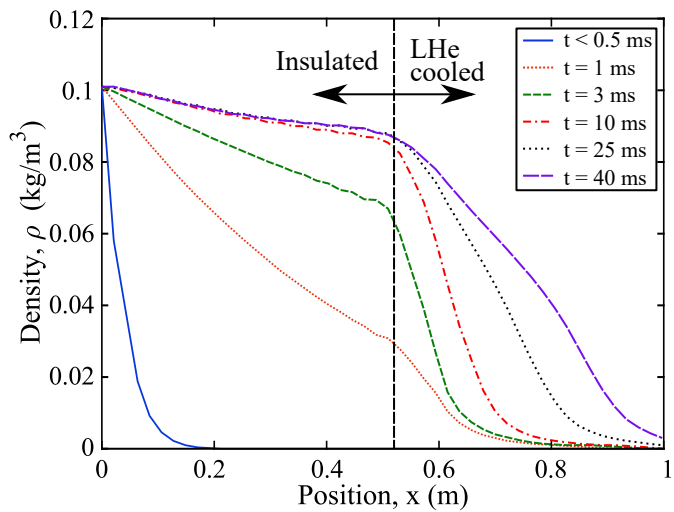


Figure 3.11: Simulation results showing condensation effect due to sharp the gas density change versus position for several different time slices.

**Inlet Region.** Inlet region is the insulated 0.57 m stainless steel section. Figure 3.10 and Figure 3.11 both show that the inlet gas properties in the 0.57 m warm section are roughly constant with only a slowly decreasing mass flow rate from the drop in buffer tank pressure. From Figure 3.11, it can be more clearly seen that in less than 25 ms, the conditions have saturated in this non-condensing entrance section. Therefore, it shows that the warm section's effect on gas properties is minimal.

**Mass Deposition Region.** The mass deposition region can be broken up into two parts: a transient sub-region and a steady deposition sub-region. Mass deposition region for a given propagation time, $t$, is located between the condensation point (i.e, the copper stainless tube transition at 0.57 m) and the location where a wall temperature spike is recorded. In Figure 3.10, for $t = 0.5$ s, this region is marked by solid vertical lines. Temporarily, this region starts forming just as the nitrogen gas passes through the warm entrance. Mass starts condensing on the surface down stream of the condensation point, gas density drops, wall temperature spikes, and a gas wave starts to form, as seen in Figure 3.11. This transient sub-region is characterized by rapid change in spacial properties (i.e., mass deposition, heat flux, wall temperature, gas density, etc.). In Figure 3.10, for $t = 0.5$ s, an approximate transient-to-steady boundary is marked by a dashed vertical line. Heat transfer in this region transitions from convective cooling to steady film boiling. This transient region also has highest mass deposition rate due to a cold tube wall. In terms of particle accelerator safety, the arrival time of this transient region is important because it marks the position behind which most of the heat and energy are deposited into the LHe bath.

Once the wall temperature rises and the main wave front passes, a dynamical equilibrium state is reached. This steady deposition sub-region is characterized by roughly constant spacial parameters (e.g., wall temperature, $GN_2$ mass deposition rate, and heat flux) over time at any location $x$. Simulated steady film boiling heat flux of 23 kW/m$^2$ were observed, which is similar to prior research [36]. Steady heat flux is an important parameter to note for beam line safety because the typically 2 K He II cavity baths will warm and can transition back to He I during high heat loads, (e.g., rising bath temperature observed earlier in Figure 2.12 (b)).

**Expansion Fan.** Figure 3.11 illustrated the development of the propagating wave as it condenses after the condensation point just after breaking the vacuum. Even though the propagating wave develops, not all the gas molecules condense onto the surface creating a very low pressure

fast moving expansion fan ahead of the main propagating wave. This is more clearly observed in the gas velocity plot in Figure 3.10. The tail tip of this expansion propagates at the escape speed, which is theoretically predicted by $2c_o/(\gamma - 1)$. Following the this tip, the gas velocity in this tail region is roughly constant at 860 m/s. At this speed, the tip reaches the end of the tube in a couple milliseconds, but this can not be observed in the scales of Figure 3.10 and Figure 3.11. As seen in the figures, gas density and pressure are very low in this region, so there is very little mass deposition. This causes the surface temperature to remain below the 4.7 K threshold. For particle accelerator safety, this region is of less importance because it does not carry the bulk of the heat and possible dust with it, but it does indicate that a larger swath of beam line cavities could have some minor, perhaps negligible, air contamination. Amount of contamination can be approximated by looking at the frost layer growth.

### 3.3.3 Frost Layer Growth

The simulation also allows one to extract information about the growth behavior of the frost layer. Figure 3.12 shows the calculated frost layer thickness growth at several locations over two seconds. Two seconds time frame was chosen because the transient-to-steady propagating $GN_2$ wave had past the last sensor in most experiments.
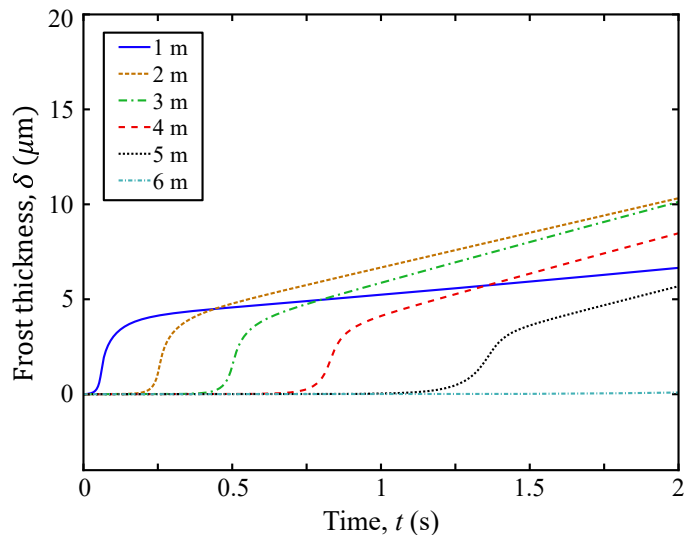


Figure 3.12: $SN_2$ frost layer growth over two seconds at several locations for 100 kPa buffer tank pressure [45].

As noted in the prior section, majority of the deposition starts as the wave front reaches the specific location. A thin layer of nitrogen frost will rapidly form, and in under 100 ms, it can be roughly 0.03 mm thick. After the transient wave passes, surface temperature stabilizes and the mass deposition rate levels off and becomes nearly constant. Constant growth is shown by the near linear slope of the frost layer profiles in Figure 3.12. Positions near the entrance see a quicker transition to steady deposition because of very high density gas, but they have a lower steady rate of growth after. This slower growth is due to the higher temperature of both the wall and gas, which makes the gas less likely to stick and condense to the surface. Convective heat transfer plays a larger role in the heat deposition in this region. Situation is opposite for locations further downstream, the lower tube see a more gradual transition to steady growth, but it has a higher rate of steady growth. This is due to a lower density gas wave arriving at the location, but the gas is cooler so it can more readily condense onto the colder surface.

Initially in Section 3.2.2, it was assumed that the frost layer would be thin and the temperature across the layer would be small. The simulation supports this assumption. Figure 3.13 shows frost layer thickness profile and the induced temperature difference across it at again 2 s, well after the rise time of the last sensor.
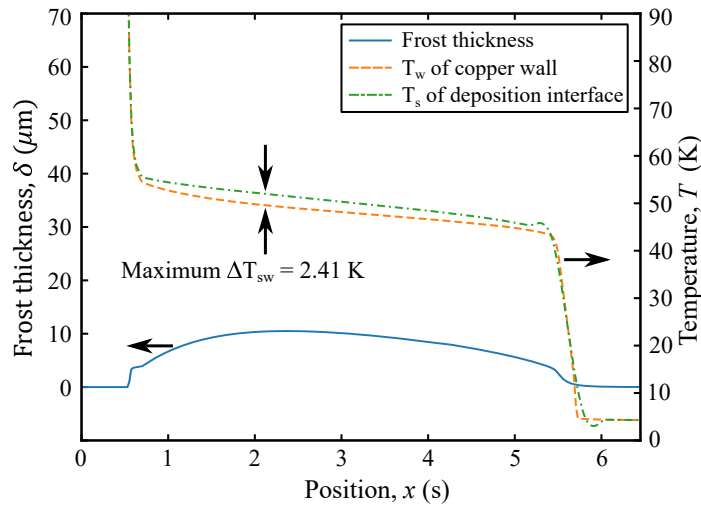


Figure 3.13: At a time slice of 2 seconds, figure shows the frost layer thickness, deposition surface temperature and wall temperature profiles along the pipe for 100 kPa buffer tank pressure [45].

Propagation wave front is located just before the 6 m location. From this figure, it can be seen that the frost layer starts building just after the condensation point, but it remains thinner due to the slower growth rate. For the 2 s time slice, a maximum thickness of the frost layer of 0.11 mm was observed at approximately $x = 2.13$ m. At that location, the thermal resistance of the layer caused only a temperature difference of a maximum of 2.41 K. Further downstream, the frost layer thins due to lower gas density and less time since the transient wave passed. At 2 seconds, frost buildup at the end of the tube due to leading expansion fan will be less than 10 $\mu$m, illustrating how very little gas actually reached that location by that time.

## 3.4   Summary

In this chapter begins by summarizing Dhuley and Van Sciver's initial analysis and discussing its weaknesses. To address these concerns, a new theoretical model was devised, which qualitatively accounts for the dynamics of a vacuum break in a He I cooled tube system. Key aspects of the model were discussed including gas dynamics, liquid helium heat transfer, and radial heat transfer through the frost layer and copper tube. Numerical simulation using the model captured some key physics of gas propagation, frost layer growth on the wall, and surface temperature variations. Temperature profiles showed reasonable agreement with wall temperatures rise times. Although, there are some differences in the transient profiles, which could be the result of experimental geometry, model simplifications, or choice of empirical values for the various models.

A range of information about gas front dynamics, mass deposition and heat transfer were able to be extracted from the simulation illustrating the usefulness of the model. Some important information to note, first the experimentally observed surface temperature rise times correspond with an internal gas density wave which forms due to condensation. It also showed that there is an expansion fan which leads the main propagating wave, but the pressure and density of this region are very low so it does not cause a significant heat load and corresponding temperature rise on the surface. The majority of gas deposition occurs after this propagating wave passes in a steady deposition region. Simulation also showed that gas density will continue to drop along the tube until it reaches a point where it very little gas remains, i.e., a freeze out point. This freezing out is the topic of an upcoming paper. Modeling also revealed that a 23 kW/m$^2$ max boiling heat flux was observed, which is an important safety parameter for particle accelerator facilities. While the

model and simulation are not perfect, they do provide foundation to build a more complex finer tuned simulation later, and they also provided a stepping stone to develop a He II model in the next chapter.

# CHAPTER 4

# VACUUM BREAK IN HELIUM II

Particle accelerators typically use He II for the SRF cavity baths because of its excellent heat transfer properties due to thermal counterflow. This chapter begins by reviewing He II heat transfer and discussing associated heat transfer model updates such that heat transfer into the He II bath can be simulated. Additionally, mass deposition model update is discussed. After, the results from the numerical simulation are validated and tuned for four different buffer tank starting pressures (i.e., 50 kpa, 100 kPa, 150 kPa, and 200 kPa). Finally, additional details of LHe heat transfer and heat deposition are extracted from the simulation, which are useful for improving particle accelerator beam line safety. Contents of this chapter have been peer reviewed and published in [46].

## 4.1   Theoretical Model Updates

He I numerical simulation provided the physics foundation for the next step of modeling He II. Radial heat transfer through the copper and growing nitrogen frost layer properties were unchanged from the He I modeling in the previous chapter. However, helium heat transfer model was updated to incorporate He II heat transfer mechanisms. He I model did not have perfect agreement so additional physics of liquid helium depth effects were added to the model. Core gas dynamics conservation equations are unchanged except for the estimation of the mass deposition term $\dot{m}_c$. Mass deposition modeled through an effective sticking coefficient allowed for reasonable agreement of the arrival times of the propagating gas front, but it is a free molecular based model. Therefore, to address this limitation, a continuum based mass condensation model was adopted for the simulation update.

### 4.1.1   He II Heat Transfer Summary and Model

As noted in Chapter 1, as liquid helium cools down, it will under go a phase transition from He I to He II at 2.17 K. He II is a temperature dependent mixture of two miscible fluid components:

normal component and the superfluid component. It is characterized by high bulk heat conductivity and low viscosity, which cause complicated changes to how LHe behaves when heat loads are applied. Main heat transfer mechanism for He II is thermal counterflow, which is highly effective for diffusing heat away from the heat source. Due to the major departure away from classical fluid behavior, there are only two stable heat transfer regimes for He II: the Kapitza regime at low heat fluxes and film boiling at high heat fluxes. Steady state heat transfer diagram is presented in Figure 4.1 and it marks both steady regimes with the transient regime between them.
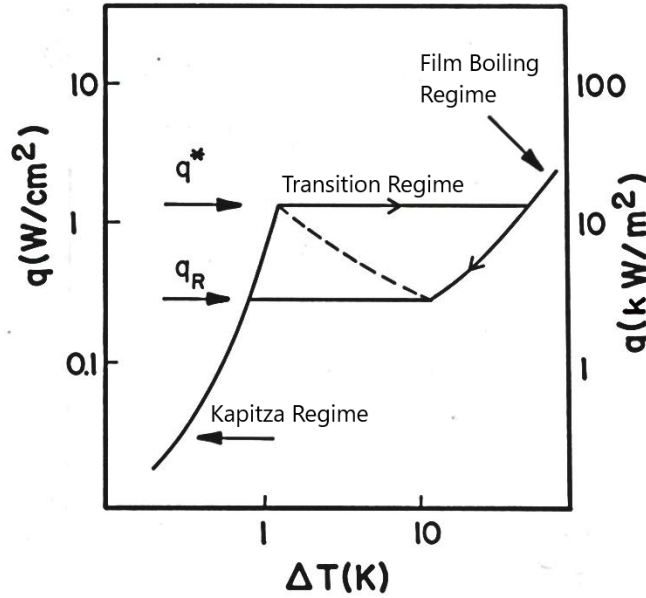


Figure 4.1: Generic heat transfer map versus temperature difference showing different regimes in a He II [18].

**Steady Heat Diffusion.** For completeness of a He II heat transfer summery, it is important to note the bulk heat transfer within the bath. To describe steady heat transfer into a large He II bath for cylindrical geometries (i.e., heaters or tubes), one can use of the radial heat diffusion equation:

$$\frac{dT_b}{dr} = -f(T_b, P)q_{He}^m \left(\frac{r_0}{r}\right)^m \tag{4.1}$$

where $m$ is an exponent that is theoretically 3, but can vary up to 4 [18]. $q_{He}$ is an applied LHe heat flux. $f(t)^{-1}$ is called thermal conductivity function for He II. $f(T) = A_{GM}\rho_n/(\rho_s \hat{s}^4 T^3)$ where

$A_{GM}$ is the Gorter-Mellink parameter, which quantifies mutual friction between the normal and super fluid [18]. Estimating $A_{GM}$, the associated $f(t)^{-1}$, and modeling thermal counterflow have been extensively studied both theoretically and experimentally by many, e.g., [66–71]. This heat diffusion equation indeed can describe the temperature gradient as radial distance from the wall increases. However, it was desired to simplify the simulation by only using empirical correlations for the different heat transfer regimes described below.

**Kapitza Regime.** Within the Kapitza regime, heat is transferred from the heat source to the bulk fluid by a process known as Kapitza conductance, and then it is quickly taken away from the wall by thermal counterflow before vapor can form. At the heat-source-liquid interface the thermal impedance resulting from two dissimilar materials is what limits the heat transfer in this regime. This is illustrated by a sudden drop in temperature at the solid-liquid interface, as illustrated in Figure 4.2 [18]. This regime generally occurs at low temperature differences (i.e.,
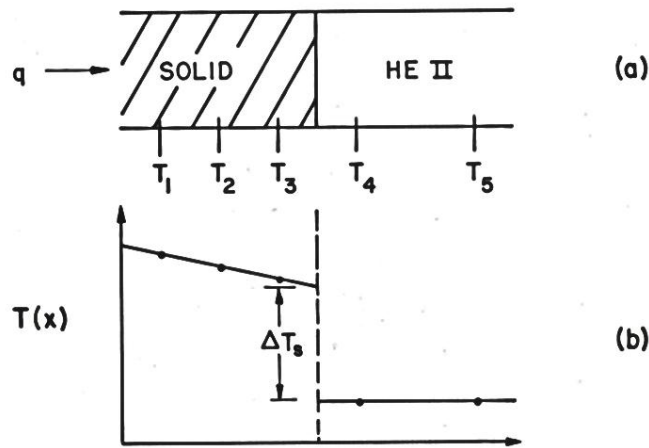


Figure 4.2: Simple illustration sensor position (a) and the drop in temperature across a solid-LHe interface (b) [18].

less than 1 K) between the bath and surface (i.e., copper tube outer wall). In this regime, LHe heat flux, $q_{He}$, depends on both the bath temperature, $T_b$ and the copper wall temperature, $T_w$. There are various studies to try to quantify the Kapitza conductance, e.g., [72–74]. Empirical and theoretically derived forms of this heat transfer regime can vary depending on applied heat flux or difference between $T_b$ and $T_w$ [18]. For a vacuum break scenario, high heat flux with a large

surface-bath temperature difference is expected. For this case, Kapitza regime heat flux can be empirically modeled through:

$$q_{He} = \omega(T_w^n - T_b^n) \tag{4.2}$$

where $\omega$ and $n$ are experimentally determined parameters which strongly depend on the surface conditions of the material [75–77]. It is important to note that there are large uncertainties in Kapitza conductance measurements. For seemingly identical surfaces, these empirical parameters can differ by a factor of two. Regardless, for the model, experimentally measured values for oxidized copper were adopted: $\omega = 0.5$ kW/m$^2$K$^n$ and $n = 3.5$ [77].

**Transition Regime.** As the heat flux increases, LHe enters into the transition to film boiling regime. This transition regime is characterized by an unstable vapor film formation. Similar to He I, this transition region occurs at a critical peak heat flux, $q_0^*$. Formation of vapor causes the surface temperature to rise without allowing an increase in the dissipating heat flux. $q_0^*$ is strongly dependent on heat source geometry, orientation, and local saturation conditions at the surface. It can be estimated by [18]:

$$q_0^*(T_b, x) = \left( \frac{2\psi}{D_2/2} \int_{T_b}^{T'(x)} \frac{dT}{f(T)} \right)^{1/3} \tag{4.3}$$

where $D_2$ is the diameter of the heat source (i.e., copper pipe or heater). For modeling in this simulation, the estimation of $f(T)^{-1}$ available within the commercial LHe property database HEPAK™ by Cryodata Inc. was used. Upper limit on the integral, $T'(x)$, is lowest temperature of either the lambda transition temperature, $T_\lambda$, or the saturation temperature, $T_{sat}$, at the local LHe saturation pressure, $P_{ls}$. $P_{ls}$ is estimated by:

$$P_{ls}(x) = P_v(T_b) + \rho_{He}gd_b(x) \tag{4.4}$$

where $P_v$ is the vapor pressure at $T_b$, and $d_b(x)$ is the depth the copper tube within the LHe bath at location $x$. Van Sciver introduced the radially-dependent empirical parameter $\psi$ to account for the differences between ideal theory (i.e., $\psi$=1) and experimental measurements of the peak steady heat flux [18, 78, 79]. However, $\psi$ was proposed for steady state modeling of experimental observations of cylinders, but transient nature of the vacuum break could reveal dependence on heat flux. Helical tube geometry, surface conditions, bath temperature, and hydrostatic head also possibly could affect the parameter. For these reasons, $\psi$ is treated as a tuning parameter within the model to best fit the experimental observations.

Within the transient regime, there is also a recovery heat flux, $q_r$, also noted in Figure 4.1. This noteworthy heat flux occurs during the cooling transition from film boiling to Kapitza regime. However, like He I modeling, $q_r$ is not relevant for the current situation because vacuum break scenario causes sudden high heat fluxes without cooling. Additional information on calculation of recovery heat flux can be found in [18].

**Film Boiling.** Film boiling regime is characterized by a vapor layer which completely coats the heated surface. At higher pressures above the lambda point transition pressure, a film of He I can also form between the bulk He II bath as illustrated in Figure 4.3 (a) and (b). Figure 4.3 (c) shows approximate location where these two scenarios would occur on a phase diagram. For experiments in this dissertation, the helium bath was evaporatively cooled by vacuum pumping, so due to low pressure, mode (a) would be type of film that can be assumed to develop. However, this will not effect the chosen film boiling model.
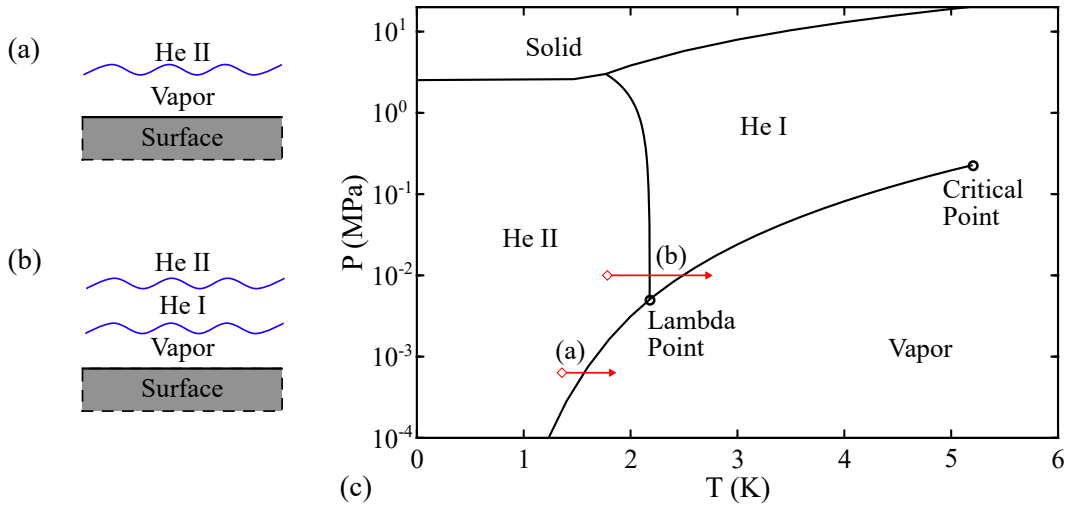


Figure 4.3: Simple illustration showing film boiling types (a) at lower pressures and (b) at higher pressures. Also representative positions on a phase diagram plot (c) where they would occur.

In the steady film boiling regime, $q_{He}$ can be modeled through Newton's law of cooling:

$$q_{He} = h_{film}(T_w - T_b) \tag{4.5}$$

where $h_{film}$ is the film boiling coefficient. $h_{film}$ has been shown to vary significantly both on bath temperature, tube wall temperature, tube radius, and hydrostatic pressure head [18, 80–82].

Relevant data matching the experimental conditions is sparse. Regardless, $h_{film} = 200 \text{ W/m}^2\text{K}$ was chosen based on published data of cylinders diameters greater than 10 mm, wall temperatures of 75 K, and an average depth of 10 cm, which is similar to our average experimental depth [18, 80, 82]

**Transient Heat Transfer.** It is again important to note that the discussion above is for steady state conditions. Vacuum break is a transient process. Experimental studies on transient helium transfer in a channel indicate that time to onset of steady film boiling occurs on the order of tens of milliseconds to tens of seconds depending heat flux, head pressure, and bath temperature [18]. The time to onset of film boiling can be estimated by [18, 83]:

$$\Delta t^* = \kappa q_a^{-4} \tag{4.6}$$

where $\kappa$ is a temperature dependent proportionality function in the form of:

$$\kappa = \frac{\rho_{He} c (T_\lambda - T_b)^2}{f(T_b) j^4} \tag{4.7}$$

where $j$ is a proportionality constant on order of unity. Based on property data from HEPAK™ database and heat fluxes on the order of 30 kW/m$^2$, transition time would be few tens of milliseconds. Ideally, a different full transient He II heat transfer model which accounts for unique features in the formation of vorticies and emission of thermal waves (e.g., [84]), would be more appropriate to better describe the actual transient physics of He II heat transfer. However, to keep things simple, computational restraints, and fact that transition time ideally is fairly short, this model assumes quasi-steady state and uses the steady state film boiling model. While not a perfect assumption, the simulation still can provide useful information and guide the next modeling improvements.

**Applied Heat Transfer Model.** Collecting all the correlations together allows a range of conditions to be applied for modeling purposes. Figure 4.4 (a) shows a representative heat transfer plot for $q_{He}$ where $\psi = 0.59$ and He II depth of 15 cm. Figure 4.4 (b) shows a slice of heat transfer map showing representative $q_{He}$ curves at $\psi=0.59$, $T_b = 2$ K, and different depths. Figure 4.4 (b) labels the different regimes and illustrates the depth effects on heat transfer. From these figures one can see that the warming bath temperature, which was seen in the experiments, will significantly effect the peak heat flux (the plateau region of the plot). Additionally, these plots indicate that the 40-60 K temperatures seen in the experiments may not be enough for some parts of the pipe to

transition to steady film boiling. This means that tuning the peak heat flux will be very important for matching the model to experimental data.
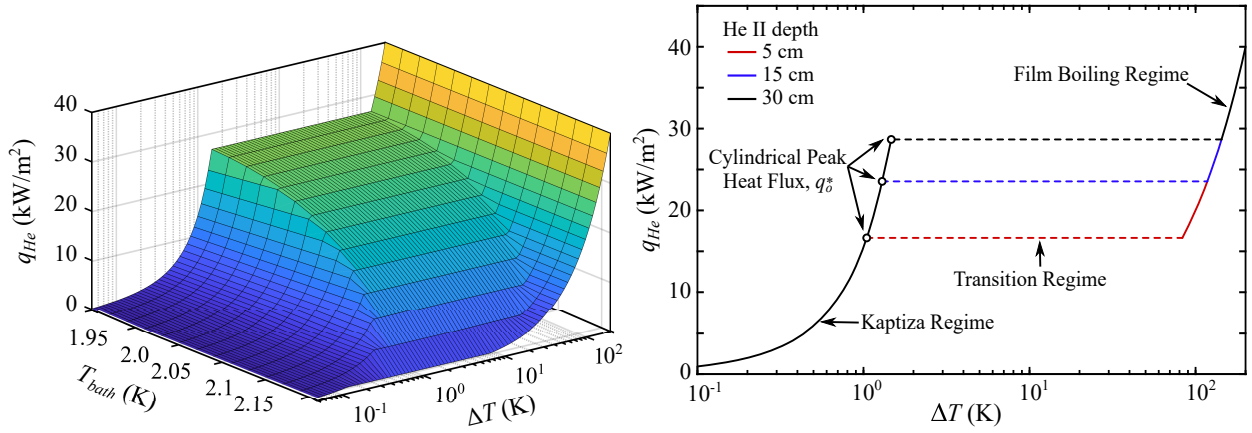


Figure 4.4: (a) A representative map of $q_{He}$ as a function of $\Delta T = T_w - T_b$ and $T_b$ with a LHe depth of 15 cm and a $\psi = 0.59$. (b) Slice of heat transfer map showing representative $q_{He}$ curves at $\psi=0.59$, $T_b = 2$ K, and different depths [46].

### 4.1.2 Mass Deposition

In the previous chapter, mass deposition, $\dot{m}_c$, was based on evaluating a sticking coefficient and an assumed ideal Maxwellian velocity distribution of the gas molecules. This model allowed the simulation results to be in reasonable agreement with experimental observations. However, sticking coefficient model was intended for use in the free molecular regime and not the continuum regime. As illustrated in the last chapter, most $GN_2$ deposits on the walls during in the steady state deposition regime; $GN_2$ density is high and it is not in the free molecular regime. Therefore, a new model was needed to correct for condensation effect, which can cause a mean flow towards the wall and thereby cause a deviation from the ideal Maxwellian distribution.

The Hertz-Knudsen relation with Schrage modification model was adopted for the modeling update [85]. This continuum regime model is based on kinetic theory and includes the equilibrium effect of condensation and evaporation on a cold surface. For this model, mass deposition is estimated by:

$$\dot{m}_c = \sqrt{\frac{M_g}{2\pi R}} \left( \Gamma(\beta)\sigma_c \frac{P}{\sqrt{T_g}} - \sigma_e \frac{P_s}{\sqrt{T_s}} \right) \qquad (4.8)$$

62

where $P_s$ is the gas saturated vapor pressure at $T_s$. $\sigma_c$ and $\sigma_e$ are empirical condensation and evaporation coefficients, which are typically about the same and close to unity for freezing interfaces [86]. For the simulations, both coefficients are taken to be 0.95. The function $\Gamma(\beta)$ describes the deviation from Maxwellian velocity distribution due to gas molecules flowing toward the cold surface. It is estimated by [85]:

$$\Gamma(\beta) = exp\left(-\beta^2\right) + \beta\sqrt{\pi}\left[1 + erf\left(\beta\right)\right] \tag{4.9}$$

where $\beta = v_r/v_{rT}$ with $v_r = \dot{m}_c/\rho_g$ being the mean radial flow velocity toward the condensing surface, and $v_{rT} = \sqrt{2RT_g/M_g}$ being the thermal velocity of the gas molecules. Note, $\Gamma$ depends on $\dot{m}_c$ from $v_r$. Therefore, in order to obtain $\dot{m}_c$, Eq. 4.8 needs to be solved self-consistently at every time step.

### 4.1.3 Boundary Conditions

Most boundary conditions remained the same for the He II simulation as they were for He I. Tube dimensions remained constant with a diameter of 25.4 mm, total length of 6.45 m with a 0.57 m warm stainless steel inlet with temperature profiles matching experimental observations. Tube was evacuated to $10^{-6}$ Pa. For systematic comparison and model validation, four different nitrogen buffer tank pressures (i.e., 50 kPa, 100 kPa, 150 kPa, and 200 kPa) were used with the associated mass flow rates. Again these mass flow rates were calculated based upon the recorded pressure drop within the tank over the experiment as detailed in Section 2.3.1. Due to limited volume of LHe, the bath temperature rose 100-150 mK over the course of all experiments (e.g., as shown in Figure 2.12 (b)). Additionally, there were slight differences in bath starting temperature ($\pm$ 25 mK) for the different starting tank pressures. It is important to point out that $q_0^*$ depends on the bath temperature, $T_b$. To ensure the simulation conditions matched experimental observations, the experimentally observed time varying bath temperature rise, $T_b(t)$, was incorporated into the model.

## 4.2 Model Validation

Gas dynamics and radial heat transfer equations remained unchanged from the He I simulations except for the above modeling updates. These equations at listed boundary conditions were solved

using the same two-step first-order Godunov-type finite difference method [31, 64]. Figure 4.5 shows a representative comparison between the simulated surface temperature profiles (a) and the experimentally observed wall temperatures (b). For the simulation, a $\psi = 1.97$ was used. Results from the simulation again reproduces key features of the experiment. Temperatures rapidly rise then start to plateau between 40 K and 60 K. Also for both experimental and simulated curves, the separation between adjacent curves gradually increases illustrating the slowing of the propagating gas wave. More importantly, one needs to look into the rise times because that marks where the
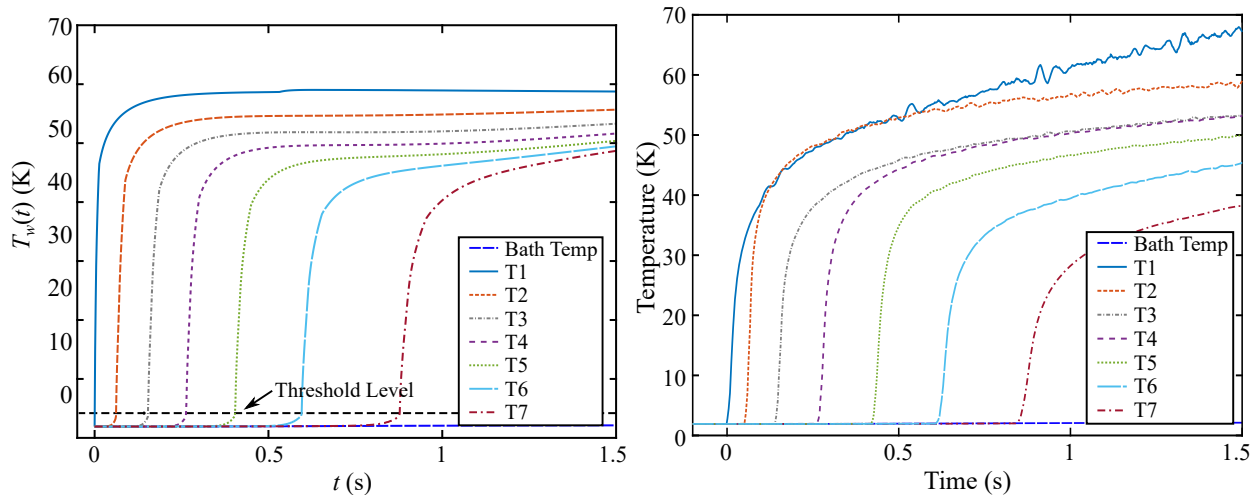


Figure 4.5: For backing tank pressures of 150 kPa, plots showing the comparison of simulated wall temperatures with an optimal $\psi = 1.97$ (a), and recorded experimental wall temperatures (b) [46].

propagating gas front is. Figure 4.6 overlays experimental and simulated data and zooms in such the rise times can be better seen. From this figure, it can be seen that the simulated rise times after tuning are very close to the experimental results.

There are some deviations from the experimental observations such as the experiments see a much sharper rise than the simulations. Also the curvature of the upper portions of the lines is similar, but do not match exactly. Experimentally, the first sensor T1 rose a little higher because of a slightly low bath level due to evaporation and boiling, which caused the sensor location to not be fully be immersed. Other deviations in the temperature profiles could be attributed to the simplifications made within the model, e.g., heat transfer model into the bulk fluid is for steady state not transient conditions or constant film boiling coefficient. In general, there is agreement
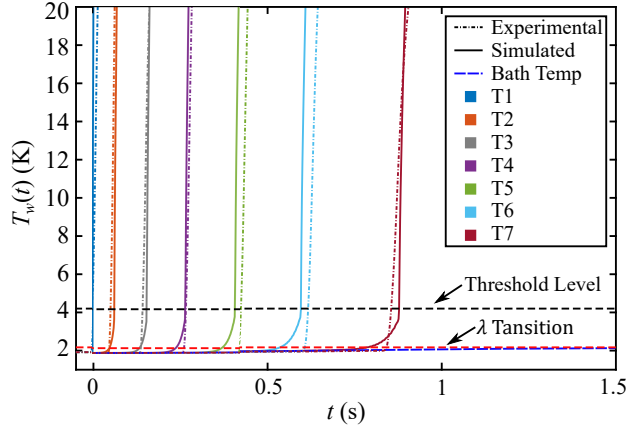
Figure 4.6: Both simulated and measured wall temperatures at different sensor locations [46].

between experimental and simulated results, which validates the model. However, this illustrates in future, development a more complex and refined model might better capture the shape of these observed temperature profiles.

Regardless of its limitations, a comparison across all data sets can still be made and other useful information can be extracted. As before, a threshold temperature (4.2 K) can be set in the vertical regions of the graph, as illustrated in Figure 4.6. This marks the position of the transient mass deposition region. The experimental and simulated rise times at the set threshold for the various tank pressures are presented in Figure 4.7. This figure shows that there is reasonable agreement between the experimentally measured rise times and the simulated rise time curves. There is slight disagreement in the 50 kPa experimental versus simulated rise time profile. Namely there is a slight bump around 3.6 m resulting from some the modeling simplifications related to film boiling. However, even with this bump slight in one curve, other curves show better agreement. It is important to remember, all calculated curves property are dependent on the choice of $\psi$ value. The optimal $\psi$ value was chosen to minimize the variance between the simulated rise times and the experimental rise times at the sensor locations for the chosen threshold temperature. Table 4.1 lists the optimized $\psi$ values for the different nitrogen backing tank pressures. All figures and discussion presented are based on these tuned $\psi$ values.
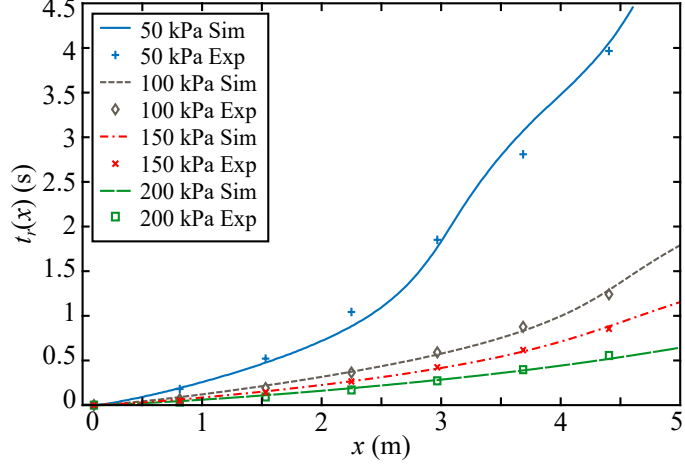
Figure 4.7: Systematic results showing comparison of simulated risetimes versus experimental rise times [46].

Table 4.1: Optimized $\psi$ values in the peak heat flux model for He II runs at different tank pressures [46].

| Tank Pressure (kPa) | Optimal $\psi$ |
|:---:|:---:|
| 50 | 0.43 |
| 100 | 0.59 |
| 150 | 1.97 |
| 200 | 1.96 |

## 4.3   He I and He II

He II was observed to have a stronger slowing effect compared to He I in Dhuley's preliminary experiments [41], and again verified in the experiments in Chapter 2. It was hypothesized that this difference was due to the to the highly efficient heat transfer mechanism, thermal counterflow, within the He II bath. A comparison of the experimental rise times of He I and He II with their simulated curves for 100 kPa buffer tank pressure is made in Figure 4.8. Optimal simulated curves show agreement with the experimental data, and they show stronger slowing effect within He II compared to He I. Experimentally, everything was conducted under almost identically conditions except one was run with He I and the other He II. Simulation wise, only difference between the two is the LHe heat transfer model and bath temperature. These results support the hypothesis, and

66

one can more affirmatively conclude that the difference in deceleration is the result of the different heat transfer mechanics of the two LHe phases.
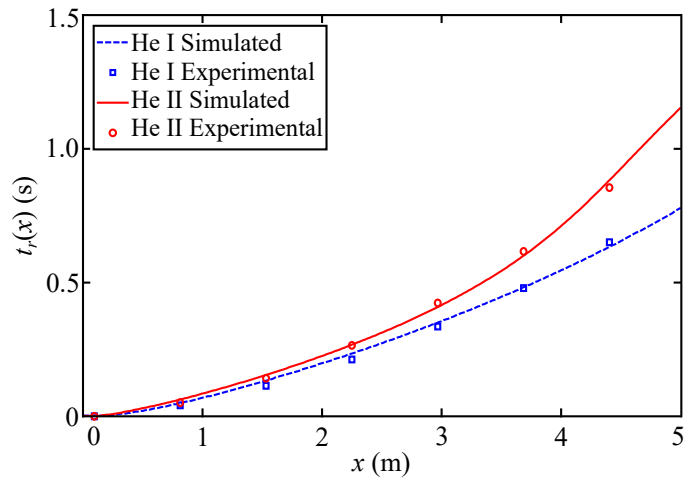


Figure 4.8: Comparison of He I and He II for 100 kPa buffer tank pressure [46].

## 4.4   Heat Deposition in He II

### 4.4.1   Deposition Heat Flux

Important aspect to particle accelerator safety is knowing the heat flux and total heat being deposited into the He II bath. For example, heat flux estimations allow operators to predict boil-off rates, which affect the sizing safety relief valves. To begin, this simulation can calculate the actual deposition heat flux into the inner tube surface from the gas, $q_{dep}(x)$, which includes the heat leaving the gas from convection and the heat being deposited due to condensation. Using 100 kPa backing tank pressure conditions as a representative example, Figure 4.9 shows estimated deposition heat flux over time at the sensor locations after being optimized.
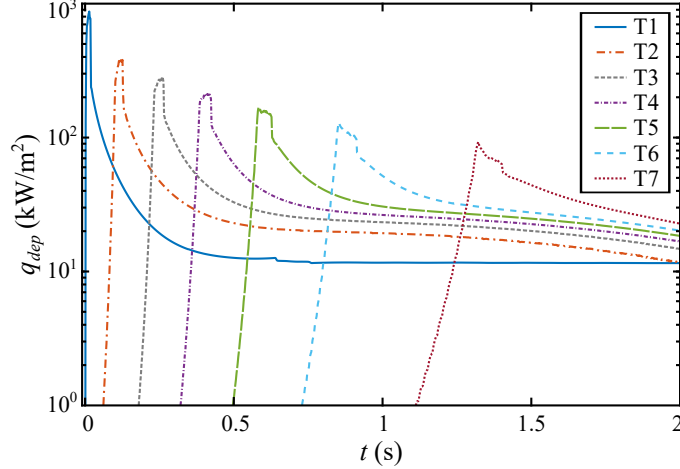
Figure 4.9: Representative graph showing simulated deposition heat flux, $q_{dep}$ passing into the tube wall at each respective sensor locations for 100 kPa tank pressure [46].

From this figure, it can be seen that the heat deposition spikes to over $10^2$ kW/m$^2$ as the main propagating wave front reaches the location. At the time of the spike, the wall location is still very cold because the leading expansion fan has not deposited much mass or transferred heat into the wall as discussed in the prior chapter. As nitrogen gas freezes to the walls, the wall temperature $T_w$ rises sharply to a local saturation point between 40 K and 60 K depending on local spacial properties. This warming results in the deposition rate rapidly dropping and then leveling off as the wall temperature approaches the local saturation conditions. The leveling of deposition heat indicates that gas convection and heat from condensation are roughly constant, and that the location has entered the previously discussed steady mass deposition region. There is a slight drop observed within the $q_{dep}(x)$, which is due to a change in the local liquid helium heat flux resulting from the bath temperature warming and tank pressure dropping.

### 4.4.2 Liquid Helium Heat Flux

As deposition heat passes through the copper tube it is deposited into the LHe bath. The heat flux into the bath, $q_{He}$, can also be extracted from these simulations. Figure 4.10 shows representative $q_{He}$ curves as a function of time at the sensor locations after optimization for 50 kPa (a) and 200 kPa (b) nitrogen buffer tank pressure.

68
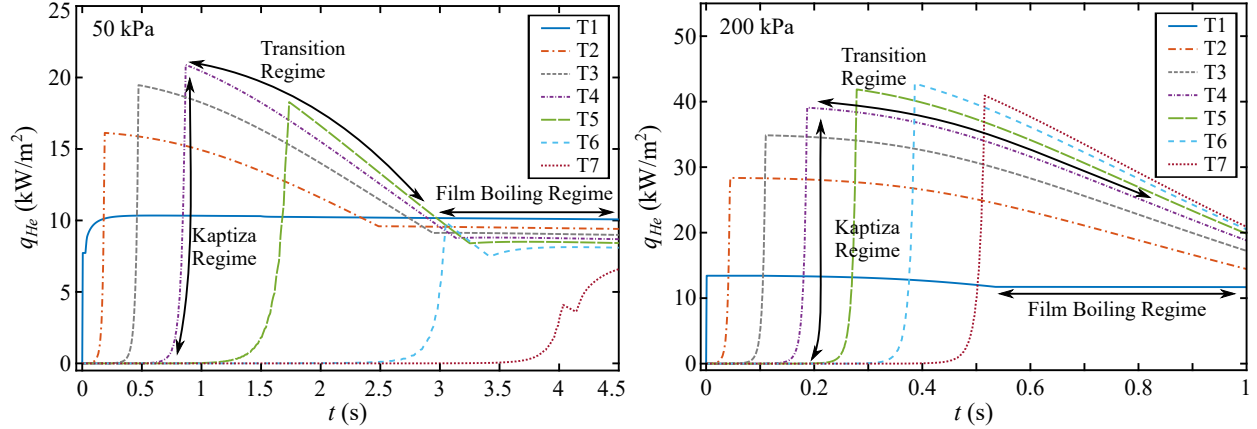
Figure 4.10: Simulated heat flux passing into the He II bath at sensor locations for representative runs with (a) 50 kPa and (b) 200 kPa tank pressures [46].

Similar to deposition heat on the inside, $q_{He}$ outside spikes up as $T_w$ rises due to the arrival of the propagating gas wave. Heat cannot be transferred away from the wall quick enough so a vapor film starts to form. In other words, heat transfer changes quickly from the Kaptiza regime to the transition to film boiling regime. The unstable vapor formation limits the heat transfer in this region at the local peak heat flux, $q_0(T_b, x)$. That limit is dependent on the bath temperature, $T_b$, and the depth, which is determined by position $x$. Wall temperature levels off as gas saturation conditions within the tube are reached. Since the temperature difference between the bath and the surface does not increase, heat transfer remains within the transition regime. However, the bath temperature is warming so the estimated peak heat flux will decrease. Figure 4.10 (a) and (b) mark the transition region as it slowly drops. As the bath temperature further warms, a gas film can more readily form and the tube can transition into steady film boiling. Due to slightly warmer experimental starting bath temperature, a larger bath temperature rise over the experiment, and a significantly longer run time, the 50 kPa run more easily readily transitions into steady film boiling. The strong depth effect also can be observed within these figures. At the beginning of the tube, the sensor position is very close to the surface so peak heat flux is lower and it transitions to steady film boiling easier. Locations further downstream are deeper in the LHe bath so the greater hydrostatic head suppresses stable film formation. Depth also effects the peak value transitioning from the Kaptiza regime to the transition regime. Deeper the sensors, the higher the peak heat flux. However, sensor locations in the middle of the tube see the greatest rise. This is due to bath

69

temperature warming over time, which limits the peak downstream when the gas front arrives at that location.

### 4.4.3   Total Heat Deposition

Total heat being deposited into the bath is also important result to consider. It determines how much a bath will warm in a given amount of time, and when a given bath volume would transition from He II to He I. Total heat deposited into the helium bath, $Q(t)$, can be estimated by:

$$Q(t) = \int_0^t dt' \int_0^L dx' \pi D_2 \cdot q_{\text{He}}(x', t') \tag{4.10}$$

$Q(t)$ for the four runs are presented in figure 4.11.
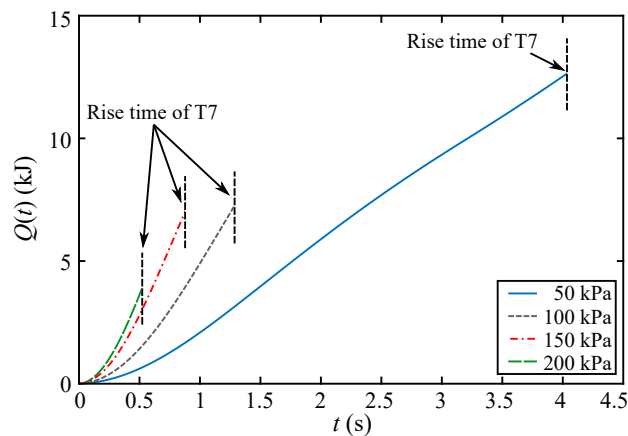


Figure 4.11: Estimated total heat, $Q(t)$, deposited into the He II bath under different pressures. Propagating GN$_2$ wave front reaches the last sensor approximately at the vertical dashed line [46].

Within this figure, the $Q(t)$ curves are cut off at the time when the rise time of the last sensor, and are marked by a dashed black vertical line. It can be seen that there is a short transient region in the beginning as the gas starts depositing on the tube walls. Curvature of the lines flattens and becomes almost linear. The slope of the lines is determined by the mass flow rate into the tube, which is a function of the nitrogen tank pressure. Linearity of the line could possibly be the result of two competing effects: The first possible factor is the drop in tank pressure which slows the mass flow rate into the tube, and thereby decreasing the total heat being depositing into the bath. The second possible factor is the increase in available condensation surface area due to propagation of the wave down the tube, which will increases the total liquid helium deposition rate. Figure also

70

shows the rate of total heat being deposited, $dQ/dt$, is higher for the 200 kPa runs compared to 50 kPa run, which is expected from the higher mass flow rate. However, due to shorter propagation time, the total heat being deposited into the bath when last sensor rose is higher at about 12 kJ for the 50 kPa run compared to 5 kJ for the 200 kPa run.

## 4.5   Summary

This chapter set out to bring the new 1D vacuum break in a tube model closer to the actual conditions of a particle accelerator beam tube cavity, which are immersed in He II. It discussed a mass deposition model update which can be used in the continuum regime unlike the first sticking coefficient model which is valid in the free molecular regime. It also discussed updates to the LHe heat transfer model to account for differences in He II. By adjusting the peak heat flux through the tuning parameter $\psi$, the simulated results and experiments were able to produce various features of the experimental wall temperature observations. One important safety factor in particle accelerator design is the heat and heat flows through the system. Using the tuned model, the results show the arrival of the gas front cause a spike in the heat being deposited into the tube walls as the gas condenses onto the surface. This spike drops off as the tube wall warms and approaches the local saturation temperature. As the wall temperature rises on the outside surface, the heat transfer into the liquid helium bath changes from Kapitza regime to the transition regime. Simulation revealed that the depth of the tube and bath temperature play a significant role in determining if and when a location transitions into the film boiling regime. Finally, as expected, it was observed the LHe heat deposition rate will be higher when the mass flow rate is higher. Although, due to shorter experimental time, the total heat deposited into the bath will be less than lower mass flow rate experiments.

# CHAPTER 5

# VACUUM BREAK IN HELIUM I WITH A CAVITY

Particle accelerator beam tubes are complex shapes such as a series of elliptical cavities [12]. This chapter discusses the addition of a bulky cavity onto a short section of tube in order to better simulate actual geometrical conditions. Results from the preliminary experiment are also presented.

## 5.1  Facility Changes

First experiments conducted in this dissertation used a long tube to develop an understanding of how gas propagation slows within a LHe cooled tube as it condenses on the wall. Actual SRF cavities have complex shapes and that shape will change based on the desired particle and its target velocity [87, 88]. The focus of the next set of experimental vacuum break studies is an elliptical style SRF cavities, which are used in particle accelerators such as those at the European X-ray Free Electron Laser (XFEL). An example of such an elliptical cavity chain with some dimensions is presented in Figure 5.1 from [12].
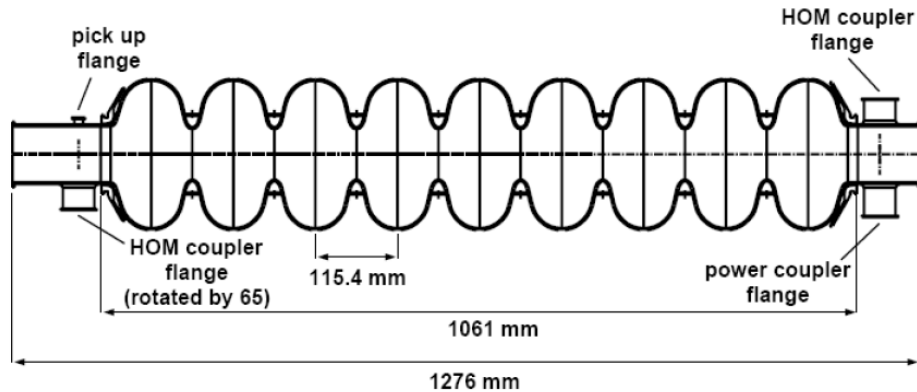


Figure 5.1: Schematic drawing of an actual SRF elliptical style cavity with dimensions [12].

It is desired to know how these chains of voluminous cavities will affect the gas propagation during sudden catastrophic loss of vacuum. To begin, only a single cavity will be considered for this

preliminary investigation. Additionally, to simplify the analysis and fabrication, a simple cylinder shape will be used. To make experimental dimensions comparable to actual system, an aspect ratio of inlet diameter : max diameter : cavity length can be approximated. An aspect ratio of 1:3:1.8 was chosen for a cavity size based on rough dimension values extracted from literature [12]. For fabrication, the helical tube coil was disconnected from the existing system and replaced with a short segment of tube with the cavity. Copper tube size is again 25.4 mm inner diameter with 1.25 mm thickness. Distance from the exit of the vacuum jacket to the beginning of the cavity is approximately 44 cm. Cylindrical cavity itself maintains the 1:3:1.8 aspect ratio with an inlet diameter of 25.4 mm (diameter of the incoming copper tube), outer diameter of 75.7 mm, and a length of 45.7 mm. Cavity walls on top, bottom, and the sides were machined such that they are 1.25 mm thick, which is the same thickness as the inlet copper tube. Basic schematic of the new experimental is presented in Figure 5.2.
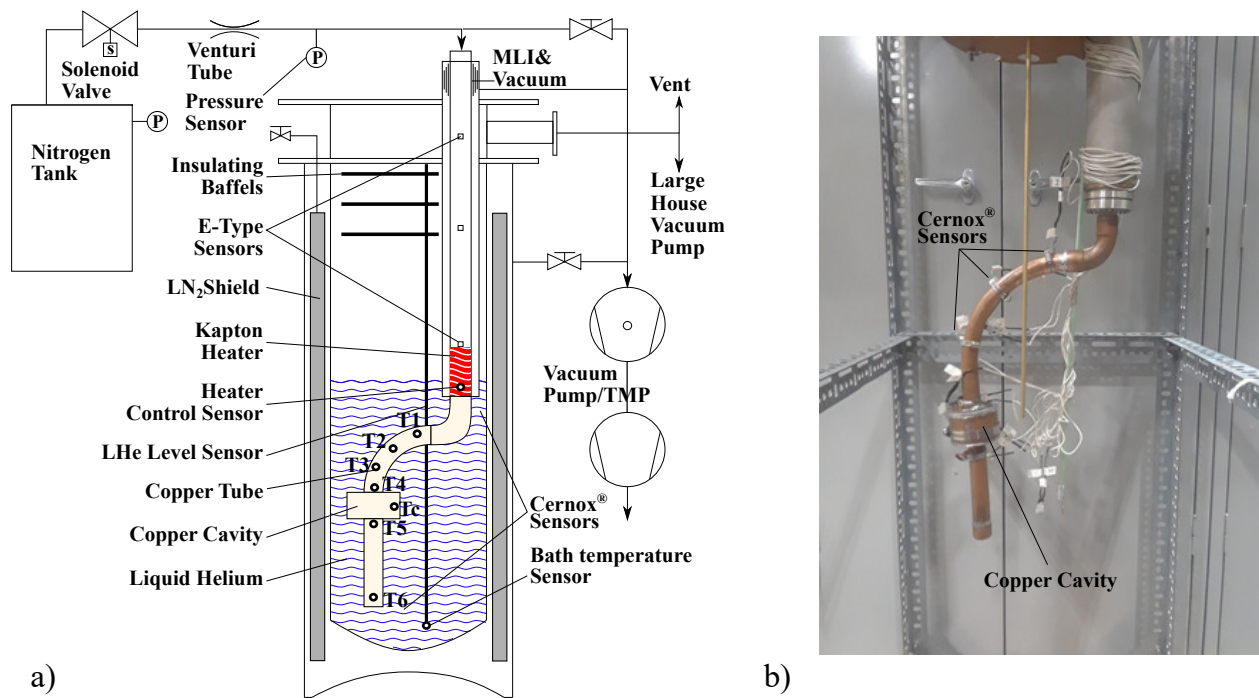


Figure 5.2: Schematic of system changes to include a bulky cavity (a). Picture of the cavity after fabrication (b).

To monitor gas propagation, like prior experiments, surface temperatures were measured with

seven Cernox™ temperature sensors. Six of temperature sensors are placed approximately 10 cm apart with the first sensor (T1) being placed 14 cm downstream of the exit of the vacuum jacket tube. Fourth sensor (T4) is just before the cavity and the fifth sensor (T5) is located just after the cavity. Last temperature sensor (Tc) was centered between T4 and T5 on the larger diameter cavity wall. Approximate sensor positioning is also illustrated in figure 5.2.

Other equipment such as the pressure sensors, power supplies, data acquisition, buffer tank, etc. were reused or unchanged from the prior helical tube experiments.

## 5.2   Preliminary Results

An experiment was run using He I and 100 kPa buffer tank pressure. Procedurally everything was conducted in the same manor as previous helical experiments. Vacuum was broken using a solenoid valve and data was recorded. Post experiment data processing remained the same as previously discussed in Chapter 2 (i.e. taking a 80 pt moving average to reduce harmonic and random noise).

Figure 5.3 (a) shows the temperature versus time plots at the different sensor locations. Figure 5.3 (b) shows a zoomed version of the helical pipe with the sensor locations. Within Figure 5.3 (a), an arbitrary threshold temperature of 0.05 K over the bath temperature is marked by horizontal dashed line. Actual arrival times of the propagating gas front are marked by vertical dashed horizontal lines. From this figure, it can be seen that the temperature sensors rise rapidly as the propagating wave reaches the sensor location. Although, there are unusual results seen just before the cavity. It is expected that the gas propagation will slow as the wave moves down the tube, which is seen by the increased time spacing from between sensors T1 and T2 compared to T2 and T3. However, the time gap between T3 and T4 temperature rise drops even though the spacial distance is the same, which indicates there may be an acceleration occurring just before the opening of the cavity. This acceleration can be more clearly observed looking at the discretized velocity, the distance between sensors over the difference in rise times, $v = \Delta x / \Delta t_r$. The velocities between the various sensor are presented in Figure 5.4. Position on this graph is taken to be the midpoint between sensors as pointed out in Figure 5.3 (b). Note, unlike previous 100 kPa helical tube measures, the time scale is around 25 ms versus 1400 ms, so the lines do not appear nearly vertical. Therefore, the chosen threshold value will affect the results. Regardless of this limitation,

velocity information can still be extracted and used qualitatively. These figures show that the velocity drops from T1 to T3. However, the velocity increases between T3 and T4 just before the cavity. After the cavity the speed drops again.
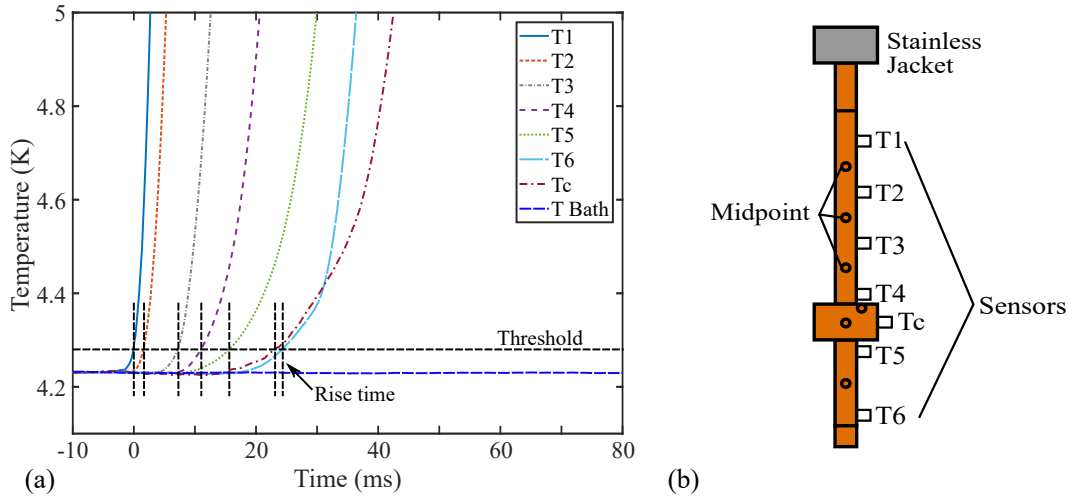


Figure 5.3: (a) Temperature versus time plot for the short segment of pipe with a cavity. (b) Illustration of sensor organization and positioning.
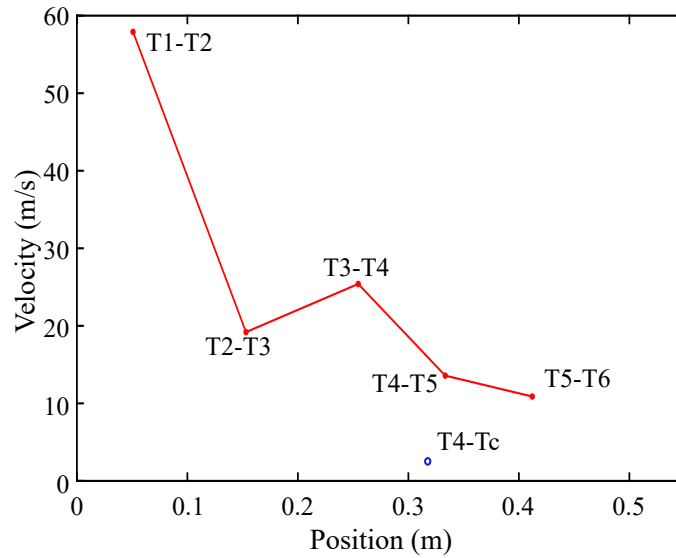


Figure 5.4: Midpoint position versus velocity graph for the short segment of pipe with a cavity.

75

Believing this could be an equipment error, a test was conducted on the data acquisition boxes using a voltage pulse generator, but results indicated that box timing was indeed correct. The experiment was redone and conducted under the same conditions, but again the same results were observed. As of this writing, it is not entirely clear why this phenomenon is being observed. However, some insight might be gained by looking at the shape of the simulated density wave front as it moves through the tube (see figure 3.11). Initially the vacuum break is characterized by an expansion fan into vacuum as previous research experiments and known gas dynamics has shown to be the case (i.e., [25, 26]). Once the gas hits the cold section, it starts condensing, which causes the propagation wave to form. However, it takes time for the mass flow rate at the start of the LHe chilled section to reach steady state, around 25 ms, due to the warm section prior. This time scale is on the same order of propagation within the short warm pipe segment. Therefore, as more mass flow enters the tube due to this building, the gas will propagate faster and possibly could cause the observed acceleration of the gas. More data in future will be needed to validate this supposition or provide an alternate explanation.

Second key observation, the position of sensor T5 is downstream of Tc, but Tc's temperature rise occurs after T5. This indicates that the gas is passing through the cavity before completely filling it. For future simulations, this indicates that a 1D simulation and modeling will not be adequate to capture the flow though the cavity.

## 5.3   Summary

This chapter covered the beginnings of the next phase of development to more closely model actual geometric and environmental conditions within an particle accelerator beam line tube. For these new experiments, the helical coil was replaced with a short segment of tube with a bulky cavity in the middle. Two key observations were made from this: First, there appears to be an acceleration of the propagating gas front just before the sudden expansion into the cavity. Second, the gas will pass through the cavity before completely filling it. Further research on this observed phenomenon is needed in future to clarify why these observations are being observed.

# CHAPTER 6

# CONCLUSION AND FUTURE REMARKS

## 6.1   Conclusion

Work in this dissertation described the development and fabrication of an experimental apparatus which one could effectively observe the deceleration of a propagating gas within a simplified beam tube cooled by either He I or He II. Dissertation also covers the development of a new model which describes the interlinked physics of gas propagation, mass deposition and heat transfer into the liquid helium bath. From these project developments, several conclusions could be reached:

1. Preliminary observations that gas propagation does slow when in a condensing environment such as a liquid helium cooled tube were again validated.

2. Through a new theoretical model describing all the interlinked physics, the surface temperature rise was shown to be tied to a propagating gas density wave within the tube, which develops as a result of condensation within the tube. If there is no condensation, the expansion into the tube is characterized by just an expansion fan.

3. Three regimes within the gas propagation are observed through the theoretical model and simulation: First is the warm entrance which quickly saturates to inlet property conditions within several tens of milliseconds. This section has little effect on the propagating gas. Second section is the mass deposition regime which can be broken up into a steady deposition region and a transient onset region. Most deposition occurs in the steady deposition region. Transient region forms the propagating wave which can span 0.5 meter section of tube. The start of this wave is marked by a temperature spike on the tube walls (i.e., the rise time). Third section is a leading expansion fan which travels at rapid speeds to the end of the tube, but does not contain much mass or energy so there little to negligible mass deposition and corresponding temperature increase. These observations are important because it indicates, there likely is not a true "shock" formation, which is classically characterized by extremely sharp change, almost a discontinuity, in properties before and after the wave front. The true observed front is a slightly more gradual density wave that reaches a local maximum, which is based on the mass deposition upstream.

4. From the systematic studies, lower mass flow rates correspond to a slower and shallower propagating wave. Propagation wave moves slower down the tube. Higher mass flow rates cause a faster propagating wave because it is not as affected by upstream mass deposition.

5. Heat transfer during a vacuum break is very complex. However, using steady state heat transfer models with a tuning parameter in both He I and He II, fair agreement of several key features within wall temperature profiles (i.e., rise times and max surface temperature) are seen between experimental and simulated results.

6. He II shows a stronger slowing effect compared to He I. This can be attributed to the higher heat transfer of He II due to thermal counterflow.

7. heat deposition into the inner wall is greatest when the wall is clean and cold. As the frost layer builds the deposition rate drops.

8. On the outside in the helium bath the heat deposition carried away from the tube is highly dependent on the bath temperature as well as bath depth, which previous modeling and research has also observed. In the case of these experiments it shows that high mass flow rate experiments and lower deeper sections of the helical tube may not observe steady film boiling.

## 6.2   Future development

This work lays the foundation for the next stage of development of vacuum break in a particle accelerator beam line tube. Using knowledge gained through this dissertation extended studied can be made. Following are suggested areas of research for future development:

This work models a straight tube cooled with LHe. SRF beam tube cavities are complex shapes such as a string of elliptical cavities. Eventually, an actual SRF cavity might be used and analyzed. However, first step is to look at a single cavity dynamics. Chapter 5 covered the beginnings of the next phase of experimentation using a voluminous cavity. However, more detailed study and analysis is needed to clarify presented observations.

As the gas propagates down the tube, it freezes to the walls. At a certain point there is no additional gas to freeze to the walls until frost layer builds significantly enough that more gas can propagate down the tube. Determining this freeze out length at any given time is the subject of an upcoming paper.

Comparing the simulation temperature profiles to the actual results, one can see the actual results show a sharper initial rise and a more gradual curvature to the upper limiting temperature than what was seen in the simulations. Expanding the LHe heat transfer model to a true transient heat diffusion into the bulk fluid may allow better agreement between the simulated and experimental time versus temperature curves.

Due to the void in relevant data, two different mass deposition models were adopted: an effective coefficient based model for the free molecular regime and a continuum based condensation model. Neither model was completely experimentally validated for a cryogenic cooled surface with nitrogen gas in the continuum regime under vacuum break conditions. Usage of an optical cryostat to observe the frost layer growth could provide insight into what is actually occurring and how well predicted frost layer growth matches with actual results during a vacuum break.

# APPENDIX A

# CALIBRATIONS

## A.1 Temperature calibrations

Lakeshore Cernox™ temperature sensors used in these experiments were calibrated using an in-house calibration rig. Calibration rig had a factory calibrated Cernox™ sensor temperature sensor which was referenced for all other sensors. Sensors were calibrated in the range of 1.4-290 K. From manufacturer recommended procedure, calculated resistance readings were centered and normalized by [89]:

$$Z = \frac{2log_{10}(R_r) - log_{10}(R_L) - log_{10}(R_U)}{log_{10}(R_U) - log(R_L)} \tag{A.1}$$

where $R_r$ is the actual resistance reading at temperature $T$, $R_U$ is the resistance at the upper bound temperature, and $R_L$ is the resistance at the lower bound temperature. Figure A.1 shows Temperatures as a function of normalization factor $Z$ for the experimentally relevant temperature range of 1.8 to 70 K.
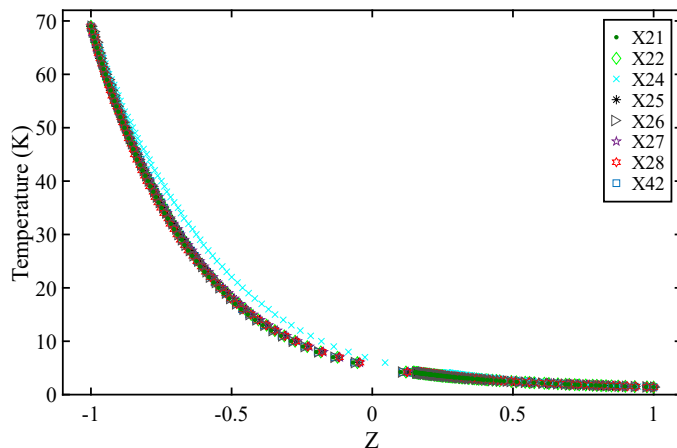


Figure A.1: Cernox™ temperature calibration as a function of normalization and centering factor Z.
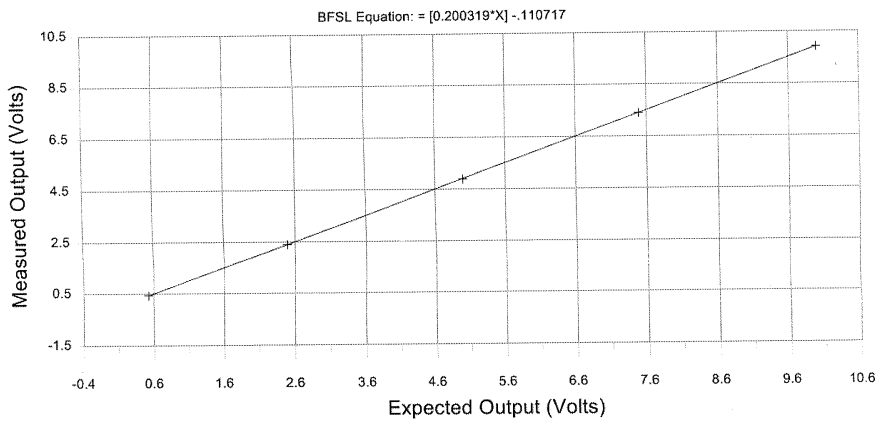
A reasonable continuous regression fit from 1.8 - 70 K for each sensor was calculated using exponential regression fit function in the form of:

$$T(Z) = Ae^{BZ} + Ee^{FZ} \tag{A.2}$$

where $A$, $B$, $E$, and $F$ are fit coefficient. Coefficients were calculated by non-linear regression using the trust-region algorithm within Matlab™.

## A.2 Pressure calibrations

Pressure transducer used in these experiment was factory calibrated. Calibration was verified upon receiving by a dial pressure gauge. Calibration certificate:

Date: 03/25/2019
Model Number: TD1000DDA005003D002X
Serial Number: 84513
Accuracy: +/-0.25% FS.BFSL

Output: 0-10V
Range: 50 psia
Excitation: 24 VDC
Temperature: 24 C

**TRANSDUCERS** *direct*

BFSL Equation: = [0.200319*X(psia)] -.110717



BFSL Equation: = [0.200319*X] -.110717



Test Equipment Used:
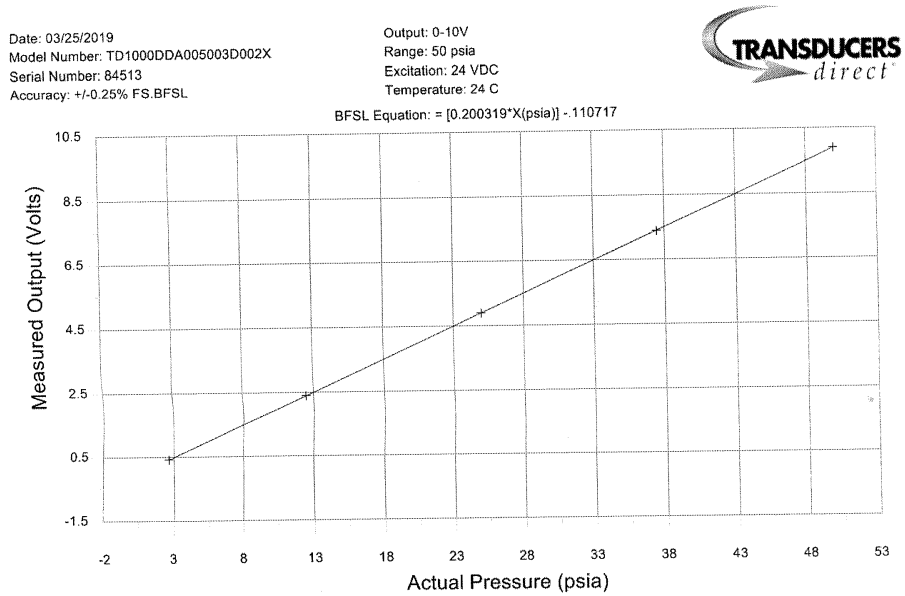
| Point # | Actual psia | Measured Value | Error[% FS] |
|---------|-------------|----------------|-------------|
| 1 | 2.700 | 0.429563 | -0.006 |
| 2 | 12.500 | 2.393587 | 0.003 |
| 3 | 25.000 | 4.898546 | 0.014 |
| 4 | 37.500 | 7.399889 | -0.014 |
| 5 | 50.000 | 9.905537 | 0.003 |

Configuration Station
Mensor CPC 4000 Ser# 810234
NIST Tracable Cal Cert ID # 84745
FLUKE 8845A Ser# F5193049
NIST Tracable Cal Cert ID # 9488005

Technician: _____

# APPENDIX B

# COPYRIGHT PERMISSIONS

Figures 1.3, 4.1, and 4.2 are reprinted from Helium cryogenics by Van Sciver [18]:

## SPRINGER NATURE LICENSE
## TERMS AND CONDITIONS

Mar 29, 2022

This Agreement between Nathaniel Garceau ("You") and Springer Nature ("Springer Nature") consists of your license details and the terms and conditions provided by Springer Nature and Copyright Clearance Center.

| | |
|---|---|
| License Number | 5253761451875 |
| License date | Feb 21, 2022 |
| Licensed Content Publisher | Springer Nature |
| Licensed Content Publication | Springer eBook |
| Licensed Content Title | Classical Helium Fluid Mechanics |
| Licensed Content Author | Steven W. Van Sciver |
| Licensed Content Date | Jan 1, 2012 |
| Type of Use | Thesis/Dissertation |
| Requestor type | academic/university or research institute |
| Format | print and electronic |
| Portion | figures/tables/illustrations |
| Number of figures/tables /illustrations | 3 |
| Will you be translating? | no |
| Circulation/distribution | 1 - 29 |
| Author of this Springer Nature content | no |
| Title | Vacuum break in a liquid helium cooled tube |
| Institution name | Florida State University |
| Expected presentation date | Apr 2022 |
| Portions | Figures 6.13, 7.1, 7.32 |
| Requestor Location | Nathaniel Garceau |

| | |
|---|---|
| Total | **0.00 USD** |

Terms and Conditions

**Springer Nature Customer Service Centre GmbH**
**Terms and Conditions**
This agreement sets out the terms and conditions of the licence (the **Licence**) between you and **Springer Nature Customer Service Centre GmbH** (the **Licensor**). By clicking 'accept' and completing the transaction for the material (**Licensed Material**), you also confirm your acceptance of these terms and conditions.

**1. Grant of License**

**1. 1.** The Licensor grants you a personal, non-exclusive, non-transferable, world-wide licence to reproduce the Licensed Material for the purpose specified in your order only. Licences are granted for the specific use requested in the order and

for no other use, subject to the conditions below.

**1. 2.** The Licensor warrants that it has, to the best of its knowledge, the rights to license reuse of the Licensed Material. However, you should ensure that the material you are requesting is original to the Licensor and does not carry the copyright of another entity (as credited in the published version).

**1. 3.** If the credit line on any part of the material you have requested indicates that it was reprinted or adapted with permission from another source, then you should also seek permission from that source to reuse the material.

## 2. Scope of Licence

**2. 1.** You may only use the Licensed Content in the manner and to the extent permitted by these Ts&Cs and any applicable laws.

**2. 2.** A separate licence may be required for any additional use of the Licensed Material, e.g. where a licence has been purchased for print only use, separate permission must be obtained for electronic re-use. Similarly, a licence is only valid in the language selected and does not apply for editions in other languages unless additional translation rights have been granted separately in the licence. Any content owned by third parties are expressly excluded from the licence.

**2. 3.** Similarly, rights for additional components such as custom editions and derivatives require additional permission and may be subject to an additional fee. Please apply to Journalpermissions@springernature.com/bookpermissions@springernature.com for these rights.

**2. 4.** Where permission has been granted **free of charge** for material in print, permission may also be granted for any electronic version of that work, provided that the material is incidental to your work as a whole and that the electronic version is essentially equivalent to, or substitutes for, the print version.

**2. 5.** An alternative scope of licence may apply to signatories of the STM Permissions Guidelines, as amended from time to time.

## 3. Duration of Licence

**3. 1.** A licence for is valid from the date of purchase ('Licence Date') at the end of the relevant period in the below table:

| Scope of Licence | Duration of Licence |
|---|---|
| Post on a website | 12 months |
| Presentations | 12 months |
| Books and journals | Lifetime of the edition in the language purchased |

## 4. Acknowledgement

**4. 1.** The Licensor's permission must be acknowledged next to the Licenced Material in print. In electronic form, this acknowledgement must be visible at the same time as the figures/tables/illustrations or abstract, and must be hyperlinked to the journal/book's homepage. Our required acknowledgement format is in the Appendix below.

## 5. Restrictions on use

**5. 1.** Use of the Licensed Material may be permitted for incidental promotional use and minor editing privileges e.g. minor adaptations of single figures, changes of format, colour and/or style where the adaptation is credited as set out in Appendix 1 below. Any other changes including but not limited to, cropping, adapting, omitting material that affect the meaning, intention or moral rights of the author are strictly prohibited.

**5. 2.** You must not use any Licensed Material as part of any design or trademark.

**5. 3.** Licensed Material may be used in Open Access Publications (OAP) before publication by Springer Nature, but any

Licensed Material must be removed from OAP sites prior to final publication.

## 6. Ownership of Rights

**6. 1.** Licensed Material remains the property of either Licensor or the relevant third party and any rights not explicitly granted herein are expressly reserved.

## 7. Warranty

IN NO EVENT SHALL LICENSOR BE LIABLE TO YOU OR ANY OTHER PARTY OR ANY OTHER PERSON OR FOR ANY SPECIAL, CONSEQUENTIAL, INCIDENTAL OR INDIRECT DAMAGES, HOWEVER CAUSED, ARISING OUT OF OR IN CONNECTION WITH THE DOWNLOADING, VIEWING OR USE OF THE MATERIALS REGARDLESS OF THE FORM OF ACTION, WHETHER FOR BREACH OF CONTRACT, BREACH OF WARRANTY, TORT, NEGLIGENCE, INFRINGEMENT OR OTHERWISE (INCLUDING, WITHOUT LIMITATION, DAMAGES BASED ON LOSS OF PROFITS, DATA, FILES, USE, BUSINESS OPPORTUNITY OR CLAIMS OF THIRD PARTIES), AND
WHETHER OR NOT THE PARTY HAS BEEN ADVISED OF THE POSSIBILITY OF SUCH DAMAGES. THIS LIMITATION SHALL APPLY NOTWITHSTANDING ANY FAILURE OF ESSENTIAL PURPOSE OF ANY LIMITED REMEDY PROVIDED HEREIN.

## 8. Limitations

**8. 1.** _**BOOKS ONLY:**_Where **'reuse in a dissertation/thesis'** has been selected the following terms apply: Print rights of the final author's accepted manuscript (for clarity, NOT the published version) for up to 100 copies, electronic rights for use only on a personal website or institutional repository as defined by the Sherpa guideline (www.sherpa.ac.uk/romeo/).

**8. 2.** For content reuse requests that qualify for permission under the STM Permissions Guidelines, which may be updated from time to time, the STM Permissions Guidelines supersede the terms and conditions contained in this licence.

## 9. Termination and Cancellation

**9. 1.** Licences will expire after the period shown in Clause 3 (above).

**9. 2.** Licensee reserves the right to terminate the Licence in the event that payment is not received in full or if there has been a breach of this agreement by you.

### Appendix 1 — Acknowledgements:

**For Journal Content:**
Reprinted by permission from [**the Licensor**]: [**Journal Publisher** (e.g. Nature/Springer/Palgrave)] [**JOURNAL NAME**] [**REFERENCE CITATION** (Article name, Author(s) Name), [**COPYRIGHT**] (year of publication)

For **Advance Online Publication papers:**
Reprinted by permission from [**the Licensor**]: [**Journal Publisher** (e.g. Nature/Springer/Palgrave)] [**JOURNAL NAME**] [**REFERENCE CITATION** (Article name, Author(s) Name), [**COPYRIGHT**] (year of publication), advance online publication, day month year (doi: 10.1038/sj.[JOURNAL ACRONYM].)

**For Adaptations/Translations:**
Adapted/Translated by permission from [**the Licensor**]: [**Journal Publisher** (e.g. Nature/Springer/Palgrave)] [**JOURNAL NAME**] [**REFERENCE CITATION** (Article name, Author(s) Name), [**COPYRIGHT**] (year of publication)

**Note: For any republication from the British Journal of Cancer, the following credit line style applies:**

Reprinted/adapted/translated by permission from [**the Licensor**]: on behalf of Cancer Research UK: : [**Journal Publisher**

(e.g. Nature/Springer/Palgrave)] [**JOURNAL NAME**] [**REFERENCE CITATION** (Article name, Author(s) Name), [**COPYRIGHT]** (year of publication)

For **Advance Online Publication** papers:
Reprinted by permission from The [**the Licensor**]: on behalf of Cancer Research UK: [**Journal Publisher** (e.g. Nature/Springer/Palgrave)] [**JOURNAL NAME**] [**REFERENCE CITATION** (Article name, Author(s) Name), [**COPYRIGHT**] (year of publication), advance online publication, day month year (doi: 10.1038/sj.[JOURNAL ACRONYM])

**For Book content:**
Reprinted/adapted by permission from [**the Licensor**]: [**Book Publisher** (e.g. Palgrave Macmillan, Springer etc) [**Book Title**] by [**Book author**(s)] [**COPYRIGHT**] (year of publication)

**Other Conditions**:

Version  1.3

**Questions?** <u>customercare@copyright.com</u> **or +1-855-239-3415 (toll free in the US) or +1-978-646-2777.**

<hr />

For Figure 1.1 from ESS eleptical cavity cryomodules by C. Darve et.al [13]:

## AIP PUBLISHING LICENSE
## TERMS AND CONDITIONS

Dec 13, 2021

This Agreement between Nathaniel Garceau ("You") and AIP Publishing ("AIP Publishing") consists of your license details and the terms and conditions provided by AIP Publishing and Copyright Clearance Center.

| | |
|---|---|
| License Number | 5207290987459 |
| License date | Dec 13, 2021 |
| Licensed Content Publisher | AIP Publishing |
| Licensed Content Publication | AIP Conference Proceedings |
| Licensed Content Title | The ESS elliptical cavity cryomodules |
| Licensed Content Author | Christine Darve, Pierre Bosland, Guillaume Devanz, et al |
| Licensed Content Date | Jan 29, 2014 |
| Licensed Content Volume | 1573 |
| Licensed Content Issue | 1 |
| Type of Use | Thesis/Dissertation |
| Requestor type | Student |
| Format | Print and electronic |
| Portion | Figure/Table |
| Number of figures/tables | 1 |
| Will you be translating? | No |
| Title | Vacuum break in a liquid helium cooled tube |
| Institution name | Florida State University |
| Expected presentation date | Apr 2022 |
| Portions | Figure 3 |
| Requestor Location | Nathaniel Garceau |

| | |
|---|---|
| Total | **0.00 USD** |

Terms and Conditions

AIP Publishing -- Terms and Conditions: Permissions Uses

AIP Publishing hereby grants to you the non-exclusive right and license to use and/or distribute the Material according to the use specified in your order, on a one-time basis, for the specified term, with a maximum distribution equal to the number that you have ordered. Any links or other content accompanying the Material are not the subject of this license.

1. You agree to include the following copyright and permission notice with the reproduction of the Material:"Reprinted from [FULL CITATION], with the permission of AIP Publishing." For an article, the credit line and permission notice must be printed on the first page of the article or book chapter. For photographs, covers, or tables, the notice may appear with the Material, in a footnote, or in the reference list.

2. If you have licensed reuse of a figure, photograph, cover, or table, it is your responsibility to ensure that the material is original to AIP Publishing and does not contain the copyright of another entity, and that the copyright notice of the figure,

For Figure 1.1 from https://lcls.slac.stanford.edu/overview is reused under Fair Use guidelines:

# Fair Use Evaluation Documentation

| | |
|---|---|
| **Name:** | Nathaniel Garceau |
| **Job Title:** | Student |
| **Institution:** | Florida State University |
| **Title of Work Used:** | Website picture |
| **Copyright Holder:** | SLAC National Accclerator Laboratory |
| **Publication Status:** | Published |
| **Publisher:** | SLAC National Accclerator Laboratory |
| **Place of Publication:** | https://lcls.slac.stanford.edu/overview |
| **Publication Year:** | unknown |
| **Description of Work:** | One of images on the page showing the linear accelerator in a long hallway. |
| **Date of Evaluation:** | March 29, 2022 |
| **Date of Intended Use:** | April 30, 2022 |

Describe the **Purpose** and Character of Your Intended Use:

Image is going to be used in a dissertation to visualize the long length of a particle accelerator. Additionally it will be used to point out the interlinking between the modular components.
[+] Use is not-for-profit
[+] Use is one-time, or is only occasional or spontaneous
[+] Use is for "criticism, comment, news reporting, teaching, (including multiple print copies for classroom use), scholarship or research"

Fair           Unfair
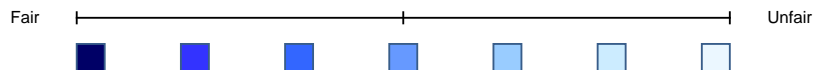
Describe the **Nature** of Your Intended Use of the Copyrighted Work:

Work is a public image on a website to a national lab (https://lcls.slac.stanford.edu/overview).
[+] Work to be used is primarily of a factual nature (non-fiction, collection of facts, etc.)
[+] Work to be used has been previously PUBLISHED

Fair ├─────────────────────┼─────────────────────┤ Unfair
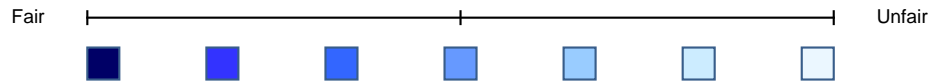
Describe the **Amount** of Your Intended Use in Relation to the Copyrighted Work as a Whole:

[+] Only limited and reasonable portions will be used.
Single image on the website will be used for illustration purposes. Image will be modified slightly to include arrows to point out features.

Fair ├─────────────────────┼─────────────────────┤ Unfair
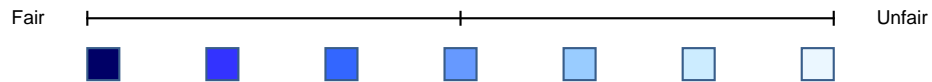
Describe the **Effect** of Your Intended Use on the Potential Market or Value of the Copyrighted Work:

[+] The work is NOT currently under commercial exploitation (out of print, no licensing available, etc.)
[+] A market for the work as it will be used is absent or is negligible & use of the work will have little or no negative impact on its value or potential value
[+] Proper attribution will be given with the intended use

Fair ├─────────────────────┼─────────────────────┤ Unfair
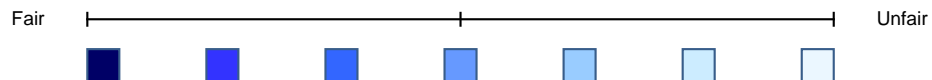
**The Average** <u>**"Fairness Level,"**</u> **Based on Your Rating of Each of the 4**

**Factors, Is:**

[see tool disclaimer for important clarifying information]:

Fair |———————————————————|———————————————————| Unfair

■ ■ ■ ■ ■ ■ ■
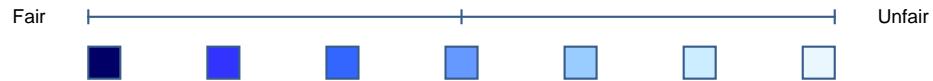
Based on the information and justification I have provided above, I, Nathaniel Garceau, am asserting this use is **FAIR** under Section 107 of the U.S. Copyright Code.

Signature: _____

Date of Signature: _____

*\*Disclaimer: This document is intended to help you* collect, organize & archive the information you might need to support your fair use evaluation. *It is not a source of legal advice or assistance. The results are only as good as the input you have provided by are intended to suggest next steps, and not to provide a final judgment. It is recommended that* you share this evaluation with a copyright specialist before proceeding with your intended use.

Figure 5.1 is reprinted under the creative commons license CC-BY-4.0. Details can be found at https://creativecommons.org/licenses/by/4.0/ and https://creativecommons.org/licenses/by/4.0/legalcode.

# BIBLIOGRAPHY

[1] B. Dotson. How particle acclerators work, 2014. U.S. Dept. of Energy, https://www.energy.gov/articles/how-particle-accelerators-work, Accessed:2021-06.

[2] D. Ungaro, A. Degiovanni, and P. Stabile. LIGHT: A Linear Accelerator for Proton Therapy. In *Proc. of N. American Particle Accelerator Conf. (NAPAC'16), Chicago, IL, USA, Oct. 9-14, 2016*, number 3 in N. American Particle Accelerator Conf., pages 1282–1286, Geneva, Switzerland, 2017. JACoW. doi: 10.18429/JACoW-NAPAC2016-FRB1IO02.

[3] A.J. Antolak. Overview of accelerator applications for security and defense. *Reviews of Accelerator Science and Technology*, 8, 2015. doi: 10.1142/s1793626815300029.

[4] CERN Press. New results indicate that particle discovered at CERN is a Higgs boson, 2013. https://home.cern/news/press-release/cern/new-results-indicate-particle-discovered-cern-higgs-boson, Accessed:2021-06.

[5] K. Dickerson. Here's what scientists really wanted to call the world's most famous particle., 2015. https://www.businessinsider.com/why-the-higgs-is-called-the-god-particle-2015-5, Accessed: 2021-06.

[6] CERN. Acclerators. https://home.cern/science/accelerators, Accessed 2021-06.

[7] SLAC National Acclerator Laboratory. SLAC by the numbers. https://www6.slac.stanford.edu/by-the-numbers, Accessed 2021-06.

[8] European Spallation Source. Acclerator. https://europeanspallationsource.se/accelerator, Accessed 2021-06.

[9] Fermilab. Science: Particle acclerators, 2019. https://www.fnal.gov/pub/science/particle-accelerators/index.html, Accessed 2021-06.

[10] C. Pagani and P. Pierini. Cryomodule design, assembly and alignment., 2005. Proc. of 12th Int. Work. on RF Supercond., Ithaca NY, https://www.classe.cornell.edu/public/SRF2005/pdfs/SuP04.pdf, Accessed: 2021-04-27.

[11] H.F. Dylla. Chapter 6.2 - the development of ultra-high-vacuum technology for particle accelerators and magnetic fusion devices. In Dorothy M. Hoffman, Bawa Singh, John H. Thomas, and John H. Thomas, editors, *Handbook of Vac. Sci. and Tech.*, pages 789–814. Academic Press, San Diego, 1998. doi: 10.1016/B978-012352065-4/50078-X.

[12] H. Padamsee. Design topics for superconducting RF cavities and ancillaries. *CERN Yellow Report CERN-2014-005*, pages 141–169, 2015. doi: 10.5170/CERN-2014-005.141.

[13] C. Darve, P. Bosland, G. Devanz, G. Olivier, B. Renard, and J.P. Thermeau. The ESS elliptical cavity cryomodules. *AIP Conference Proceedings*, 1573(1):639–646, 2014. doi: 10.1063/1.4860762.

[14] G. Ciovati. AC/RF superconductivity. *CERN Yellow Report CERN-2014-005*, pages 57–75, 2015. doi: 10.5170/CERN-2014-005.57.

[15] W. Singer. SRF cavity fabrication and materials. *CERN Yellow Report CERN-2014-005*, pages 171–207, 2015. doi: 10.5170/CERN-2014-005.171.

[16] R. Flukiger. Superconductivity for magnets. *CERN Yellow Report CERN-2014-005*, pages 247–267, 2015. doi: 10.5170/CERN-2014-005.247.

[17] S. Angus, K.M. de Reuck, and R.D. McCarty. Int. thermo. tables of the fluid state helium–4. volume 4 of *Int. Thermo. Tables of the Fluid State*. Pergamon Press, New York, NY, 1977. ISBN 9781483280684.

[18] Steven W. Van Sciver. *Helium Cryogenics*. International cryogenics monograph series. Springer, New York, 2nd edition, 2012. ISBN 978-1-4419-9978-8 978-1-4419-9979-5.

[19] Thomas Flynn. *Cryogenic Engineering*. Marcel Dekker, New York, 2 edition, November 2004. doi: 10.1201/9780203026991.

[20] G. Petitpas and S.M. Aceves. Modeling of sudden hydrogen expansion from cryogenic pressure vessel failure. *Int. J. of Hydrogen Energy*, 38(19):8190–8198, 2013. ISSN 0360-3199. doi: 10.1016/j.ijhydene.2012.03.166. URL https://www.sciencedirect.com/science/article/pii/S0360319912008646.

[21] G.F. Xie, X.D. Li, and R.S. Wang. Study on the heat transfer of high-vacuum-multilayer-insulation tank after sudden, catastrophic loss of insulating vacuum. *Cryogenics*, 50(10): 682–687, 2010. ISSN 0011-2275. doi: 10.1016/j.cryogenics.2010.06.020.

[22] S.M. Harrison. Loss of vacuum experiments on a superfluid helium vessel. *IEEE Trans. on Appl. Supercond.*, 12-1:1343–1346, March 2002. doi: 10.1109/TASC.2002.1018651.

[23] P. Lebrun and E. Delucinge. Interim summary report on the analysis of the 19 september 2008 incident at the lhc. Technical Report EDMS 973073, CERN, 2008. https://edms.cern.ch/document/973073/1.

[24] A.H. Shapiro. *The dynamics and thermodynamics of compressible fluid flow*, volume 2. The Ronald Press, New York, 1 edition, 1954.

[25] T. Takiya, F. Higashino, Y. Terada, and A. Koumura. Pressure wave propagation by gas expansion in a high vacuum tube. *Vacuum Sci. and Technol. A*, 17:2059–2063, 1999. doi: 10.1116/1.581726.

[26] J. John and T. Keith. *Gas Dynamics*. Pearson Education Inc., Upper Saddle River, NJ, USA, 3 edition, 2006. ISBN 9780132023313.

[27] Shock Wave Laboratory. Current research projects., 2021. Shock Wave Laboratory RWTH, Aachen University, www.swl.rwth-aachen.de/en/research/current-projects/, Accessed: 2021-06.

[28] Petersen Research Group. Shock-tube physics., 2021. https://petersengroup.tamu.edu/research-2/gas-dynamics-chemical-kinetics/shock-tube-physics/, Accessed 2021-06.

[29] M. Ady, G. Vandoni, M. Guinchard, P. Grosclaude, R. Kersevan, R. Levallois, and M. Faye. Measurement campaign of 21-25 july 2014 for evaluation of hie-isolde inrush protection system. Technical Report EDMS No. 1414574, CERN, 2014.

[30] M. Ady, M. Hermann, R. Kersevan, G. Vandoni, and D. Ziemianski. Leak propagation dynamics for the hie-isolde super conducting linac. *5th Int. Particle Accelerator Conf. Proc.*, pages 2351–2353, 2014. doi: 10.18429/JACoW-IPAC2014-WEPME039.

[31] I. Danaila, P. Joly, S.M. Kaber, and M. Postel. *An Introduction to Scientific Computing: Twelve Computational Projects Solved with MATLAB*. Springer-Verlag, New York, 2007. doi:10.1007/978-0-387-49159-2.

[32] J. P. Dawson and J. D. Haygood. Cryopumping. *Cryogenics*, 5(2):57–67, 1965. doi: 10.1016/S0011-2275(65)80002-9.

[33] Kimo M. Welch. *Capture pumping technology*. Elsevier, Amsterdam, 2nd fully rev. edition, 2001. ISBN 978-0-444-50882-9 978-0-444-50941-3.

[34] K.W. Rogers. Experimental investigations of solid nitrogen formed by cryopumping. Technical Report Report No. NASA-CR-553, NASA, 1966. Retrieved from NASA, Tech. Rep. Server.

[35] E. Bosque. *Transient heat transfer to helium II due to a sudden loss of insulating vacuum*. Dissertation, Florida State University, Tallahassee, 2014. Retrieved from FSU, Proquest Diss. Publishing database (UMI No. 3625730).

[36] M. Wiseman, K. Crawford, M. Drury, K. Jordan, J. Preble, Q. Saulter, and W. Schneider. Loss of cavity vacuum experiment at CEBAF. In Peter Kittel, editor, *Adv. in Cryog. Eng.*, volume 39 of *Adv. in Cryog. Eng.*, pages 997–1003. Springer US, Boston, MA, 1994. doi: 10.1007/978-1-4615-2522-_121.

[37] T. Boeckmann, D. Hoppe, K. Jensch, R. Lange, W. Maschmann, B. Petersen, and T. Schnautz. Experimental tests of fault conditions during the cryogenic operation of a XFEL prototype cryomodule. *Proc. of the Int. Cryog. Eng. Conf. 22 -- Int. Cryog. Mater. Conf.-2008*, page 723–728, 2009.

[38] Andrew A. Dalesandro, Jay Theilacker, and Steven Van Sciver. Experiment for transient effects of sudden catastrophic loss of vacuum on a scaled superconducting radio frequency cryomodule. In *AIP Conf. Proc.*, volume 1434, pages 1567–1574, Spokane, Washington, USA, 2012. doi: 10.1063/1.4707087.

[39] R.C. Dhuley and S.W. Van Sciver. Propagation of nitrogen gas in a liquid helium cooled vacuum tube following sudden vacuum loss – Part I: Experimental investigations and analytical modeling. *Int. Heat Mass Tran.*, 96:573–581, 2016. doi: 10.1016/j.ijheatmasstransfer.2016.01.077.

[40] R. C. Dhuley and S. W. Van Sciver. Propagation of nitrogen gas in a liquid helium cooled vacuum tube following sudden vacuum loss – Part II: Analysis of the propagation speed. *Int. Heat Mass Tran.*, 98:728–737, 2016. doi: 10.1016/j.ijheatmasstransfer.2016.03.077.

[41] Ram C Dhuley. *Gas Propagation in a Liquid Helium Cooled Vacuum Tube Following a Sudden Vacuum Loss*. Dissertation, Florida State University, Tallahassee, 2016. Retrieved from FSU, Proquest Diss. Publishing database (UMI No. 10120583).

[42] N. Garceau, W. Guo, and T. Dodamead. Gas propatation following a sudden loss of vacuum in a pipe cooled by He I and He II. In *Adv. in Cryo. Eng.: Proc. of the Cryo. Eng. Conf. (CEC) July 2017, Madison, WI, USA*, volume 278 of *IOP Conf. Ser.: Mater. Sci. and Eng.*, page 012068. IOP Publishing, Philadephia, Pa, 2017. doi:10.1088/1757-899X/278/1/012068.

[43] N.M. Garceau, S. Bao, W. Guo, and S.W. Van Sciver. The design and testing of a liquid helium cooled tube system for simulating sudden vacuum loss in particle acclerators. *Cryogenics*, 100: 92–96, 2019. doi: 10.1016/j.cryogenics.2019.04.012.

[44] N. Garceau, S.R. Bao, and W. Guo. Heat and mass transfer during a sudden loss of vacuum in a liquid helium cooled tube – Part I: Interpretation of experimental observations. *Int. Heat Mass Tran.*, 129:1144–1150, 2019. doi: 10.1016/j.ijheatmasstransfer.2018.10.053.

[45] N. Garceau, S.R. Bao, and W. Guo. Heat and mass transfer during a sudden loss of vacuum in liquid helium cooled tube - Part II: Theoretical modeling. *Int. J. Heat Mass Tran.*, 146, 2020. doi: 10.1016/j.ijheatmasstransfer.2019.118883.

[46] N. Garceau, S.R. Bao, and W. Guo. Heat and mass transfer during a sudden loss of vacuum in a liquid helium cooled tube – Part III: Heat deposition in He II. *Int. Heat Mass Tran.*, 181: 121885, 2021. doi: 10.1016/j.ijheatmasstransfer.2021.121885.

[47] R.C. Dhuley and S.W. Van Sciver. Epoxy encapsulation of Cernox$^{TM}$ SD thermometer for measuring the temperature of surfaces in liquid helium. *Cryogenics*, 77:49–52, 2016. doi: 10.1016/j.cryogenics.2016.05.001.

[48] J.H. Leinhard and C.L. Tein. *Statistical Thermodynamics*. Hemisphere Pub. Corp., 1979. ISBN 0891160485. URL https://uh.edu/engines/StatisticalThermodynamics.pdf.

[49] G. Van Wylen and R. Sonntag. *Fundamentals of classical thermodynamics.* John Wiley and Sons, Inc., Hoboken, NJ, USA, 1965.

[50] R.A. Haefer. Cryogenic vacuum techniques. *J. of Phy. E: Sci. Inst.*, 14(3):273–288, March 1981. ISSN 0022-3735. doi: 10.1088/0022-3735/14/3/002.

[51] N. Fray and B. Schmitt. Sublimation of ices of astrophysical interest: A bibliographic review. *Planetary and Space Science*, 57(14-15):2053–2080, December 2009. ISSN 00320633. doi: 10.1016/j.pss.2009.09.011.

[52] M. Maerefat, S. Fujikawa, T. Akamatsu, T. Goto, and T. Mizutani. An experimental study of non-equilibrium vapor condensation in a shock-tube. *Exp. in Fluids*, 7:513–520, 1989. doi: 10.1007/BF00187402.

[53] M.E. Bland. The cryopumping of water vapour in the continuum pressure region. *Cryogenics*, 15(11):639–643, November 1975. ISSN 00112275. doi: 10.1016/0011-2275(75)90094-6.

[54] G Davey. Cryopumping in the transition and continuum pressure regions. *Vacuum*, 26(1): 17–22, January 1976. ISSN 0042-207X. doi: 10.1016/S0042-207X(76)80414-9.

[55] Frank P. Incropera, David P. Dewitt, Theodore L. Bergman, and Adrienne S. Lavine. *Fundamentals of Heat and Mass Transfer.* John Wiley and Sons, Hoboken, NJ, 6th edition, 2007. ISBN 978-0-471-45728-2.

[56] National Institute of Standards and Technology. Nist chemistry webbook, srd69, 2021. U.S. Dept. of Commerce, https://webbook.nist.gov/chemistry/fluid/, Accessed:2021-12.

[57] Jonas Lantz. *Heat Transfer Correlations Between a Heated Surface and Liquid Superfluid Helium.* Thesis, Linköpings universitet, Linköping, Sweden, 2007. https://www.diva-portal.org/smash/get/diva2:16858/FULLTEXT01.pdf.

[58] D.N. Lyon. Boiling heat transfer and peak nucleate boiling fluxes in saturated liquid helium between the lambda and critical temperatures. *Intern. Advan. Cryog. Eng.*, 10:371, 01 1965.

[59] B. P. Breen and J. W. Westwater. Effect of diameter of horizontal tubes on film boiling heat transfer. *Chemical Engineering Progress*, 58:67–72, 1962.

[60] C. Schmidt. Transient heat transfer and recovery behavior of superconductors. *IEEE Transactions on Magnetics*, 17(1):738–741, 1981. doi: 10.1109/TMAG.1981.1060947.

[61] National Institute of Standards and Technology. Nist: properties of solid materials from cryogenic- to room-temperatures, 2022. U.S. Dept. of Commerce, https://trc.nist.gov/cryogenics/materials/materialproperties.htm, Accessed:2022-01.

[62] T. Cook and G. Davey. The density and thermal conductivity of solid nitrogen and carbon dioxide. *Cryogenics*, 16(6):363–369, June 1976. ISSN 00112275. doi: 10.1016/0011-2275(76)90217-4.

[63] T.A. Scott. Solid and liquid nitrogen. *Physics Reports*, 27(3):89–157, September 1976. ISSN 03701573. doi: 10.1016/0370-1573(76)90032-6.

[64] G.A. Sod. A survey of several finite difference methods for systems of nonlinear hyperbolic conservation laws. *J. Comput. Phy.*, 27(1):1–31, 1978. doi: 10.1016/0021-9991(78)90023-2.

[65] R.V. Smith. Review of heat transfer to helium I. *Cryogenics*, 9(1):11–19, February 1969. ISSN 00112275. doi: 10.1016/0011-2275(69)90251-3.

[66] A. Sato, M. Maeda, T. Danstuka, M. Yuyama, and Y. Kamioka. Temperature dependence of the Gorter-Mellink exponent $m$ measured in a channel. In *Adv. in Cryog. Eng.*, volume 51A of *Adv. in Cryog. Eng.*, page 387. Springer US, Boston, MA., 2006. doi:10.1063/1.2202439.

[67] William Frank Vinen. Mutual friction in a heat current in liquid helium II III. Theory of the mutual friction. *Proc. R. Soc. Lond. A*, 242(1231):493–515, November 1957. doi: 10.1098/rspa.1957.0191.

[68] D. R. Tilley and J. Tilley. *Superfluidity and Superconductivity*. Graduate Student Series in Physics. Adam Hilger Ltd, Bristol, 2 edition, 1986. ISBN 9780852748077.

[69] K. W. Schwarz. Turbulence in superfluid helium: Steady homogeneous counterflow. *Phys. Rev. B*, 18:245–262, 1978. doi: 10.1103/PhysRevB.18.245.

[70] J. Gao, E. Varga, W. Guo, and W. F. Vinen. Statistical measurement of counterflow turbulence in superfluid helium-4 using $He_2^*$ tracer-line tracking technique. *J. Low Temp. Phys.*, 187:490, 2017. doi: 10.1007/s10909-016-1681-y.

[71] Brian Mastracci and Wei Guo. Exploration of thermal counterflow in He II using particle tracking velocimetry. *Phys. Rev. Fluids*, 3(6):063304, 2018. doi: 10.1103/PhysRevFluids.3.063304.

[72] N.S. Snyder. Heat transport through helium II: Kapitza conductance. *Cryogenics*, 10:89–95, 1970. doi: 10.1016/0011-2275(70)90077-9.

[73] L.J. Challis. Experimental evidence for a dependence of the Kapitza conductance on the Debye temmperature of a solid. *Phys. Lett. A*, 26:105–106, 1968. doi: 10.1016/0375-9601(68)90499-4.

[74] R.E. Peterson and A.C Anderson. The Kapitza thermal boundry resistance. *J. Low Temp. Phys.*, 11:639–665, 1973. doi: 10.1007/BF00654451.

[75] G. Claudet and P. Seyfert. Bath cooling with subcooled superfluid helium. *Adv. Cryog. Eng.*, 27:441, 1981.

[76] A. Iwamoto, R. Maekawa, and T. Mito. Kapitza conductance of an oxidized copper surface in saturated He II. *Cryogenics*, 41(5):367–371, 2001. ISSN 0011-2275. doi: https://doi.org/10.1016/S0011-2275(01)00082-0.

[77] A. Kashani and S.W. Van Sciver. High heat flux kapitza conductance of technical copper with several different surface preparations. *Cryogenics*, 25(5):238–242, 1985. doi: 10.1016/0011-2275(85)90202-4.

[78] S.W. Van Sciver and R.L. Lee. Heat transfer to helium-II in cylindrical geometries. In *Adv. Cryog. Eng.*, volume 25 of *Adv. Cryog. Eng.*, pages 363–371. Springer US, Boston, MA., 1980. doi: 10.1007/978-1-4613-9856-1_43.

[79] S.W. Van Sciver and R.L. Lee. Heat transfer from circular cylinders in He II. In *Cryogenic Process and Equipment in Energy Systems*, volume H00164, page 147. ASME Publication, Boston, MA., 1981.

[80] K.R. Bretts and A.C. Leonard. Free convection film boiling from a flat, horizontal surface in saturated He II. In *Adv. in Cryog. Eng.*, volume 21 of *Adv. in Cryog. Eng.*, pages 282–292. Springer US, Boston, MA., 1975. doi: 10.1007/978-1-4757-0208-8_37.

[81] R.C. Steed and R.K Irey. Corelation of the depth effect on film boiling heat transfer in liquid helium II. In *Adv. in Cryog. Eng.*, volume 15 of *Adv. in Cryog. Eng.*, pages 299–307. Springer US, Boston, MA., 1995. doi: 10.1007/978-1-4757-0513-3_36.

[82] J. S. Goodling and R. K. Irey. Non-boiling and film boiling heat transfer to a saturated bath of liquid helium. In K. D. Timmerhaus, editor, *Adv. Cryog. Eng.*, volume 14 of *Adv. Cryog. Eng.*, pages 159–169, Boston, MA, 1969. Springer US.

[83] S.W. Van Sciver. Transient heat transport in he II. *Cryogenics*, 19(7):385–392, 1979. doi: 10.1016/0011-2275(79)90120-6.

[84] Shiran Bao and Wei Guo. Transient heat transfer of superfluid $^4$He in nonhomogeneous geometries: Second sound, rarefaction, and thermal layer. *Phys. Rev. B*, 103:134510, Apr 2021. doi: 10.1103/PhysRevB.103.134510.

[85] J.G. Collier and J.R. Thome. *Convective Boiling and Condensation*. Oxford University Press, New York, 3rd edition, 1994. ISBN 0-19-85628-9.

[86] Aaron H. Persad and Charles A. Ward. Expressions for the evaporation and condensation coefficients in the Hertz-Knudsen relation. *Chem. Rev.*, 116(14):7727–7767, July 2016. doi: 10.1021/acs.chemrev.5b00511.

[87] H. Padamsee, J. Knobloch, and T. Hays. *RF Super conductors for Acclerators*. John Wiley & Sons, New York, 2nd edition, 2008. ISBN 978-3-527-40842-9.

[88] H. Padamsee. *RF Superconductivity: Science, Technology and Applications.* Wiley-VCH, Weinheim, 2nd edition, 2009. ISBN 978-3-527-40842-9.

[89] Lakeshore Cryotronics Inc. Appendix d: Sensor calibration accuracies, 2022. https://www.lakeshore.com/products/categories/downloads/temperature-products/cryogenic-temperature-sensors/cernox, Accessed:2022-03.

# BIOGRAPHICAL SKETCH

Nathaniel M. Garceau was born and raised in Florida. He graduated from high school in 2004. He attended University of Florida from 2004 - 2007, and transferred to Florida Institute of Technology where he graduated with a Bachelors in Chemical Engineering in 2009. From 2007 - 2011, he worked as a student summer intern and then later full time as a research engineer at the Florida Solar Energy Center (FSEC), which is a branch of University of Central Florida in Cocoa Florida. At FSEC, he worked on biomass gassification, catalysis and liquid hydrogen research projects. In 2011, he traveled to Tokyo, Japan for nine months as a study abroad learning Japanese language and culture at KCP International Language Institute. From 2012 - 2015, he lived in South Korea where he obtained a Masters in Engineering from Korea Institute of Science and Technology's (KIST) R&D Academy and a Masters of Science in Energy and Environment Engineering from University of Science and Technology (UST). His Masters' work was dealing with liquid hydrogen liquefaction and storage. While in Korea, he also helped found Hylium Industries Inc., which as of this writing is still in business and selling liquid hydrogen drones, mobile hydrogen vehicle refilling stations, and other cryogenic technologies. In spring 2017, he moved to Tallahassee and began work on this dissertation. Nathaniel has multiple peer reviewed papers and has presented at engineering conferences. His first conference was the 2013 Cryogenic Engineering Conference in Anchorage, Alaska. As of this publication, his full resume and publication list can be found on his Linkedin profile: https://www.linkedin.com/in/nathaniel-garceau-02632289 .